

6-28-2016

# Vortex Rossby Wave Propagation in Three Dimensional Tropical-Cyclone-Like Baroclinic Vortices

Cen Gao  
cgao003@fiu.edu

**DOI:** 10.25148/etd.FIDC000788

Follow this and additional works at: <https://digitalcommons.fiu.edu/etd>

 Part of the [Atmospheric Sciences Commons](#), and the [Meteorology Commons](#)

---

## Recommended Citation

Gao, Cen, "Vortex Rossby Wave Propagation in Three Dimensional Tropical-Cyclone-Like Baroclinic Vortices" (2016). *FIU Electronic Theses and Dissertations*. 2533.

<https://digitalcommons.fiu.edu/etd/2533>

This work is brought to you for free and open access by the University Graduate School at FIU Digital Commons. It has been accepted for inclusion in FIU Electronic Theses and Dissertations by an authorized administrator of FIU Digital Commons. For more information, please contact [dcc@fiu.edu](mailto:dcc@fiu.edu).

FLORIDA INTERNATIONAL UNIVERSITY

Miami, Florida

VORTEX ROSSBY WAVE PROPAGATION IN THREE DIMENSIONAL  
TROPICAL-CYCLONE-LIKE BAROCLINIC VORTICES

A dissertation submitted in partial fulfillment of the

requirements for the degree of

DOCTOR OF SCIENCE

in

GEOSCIENCES

by

Cen Gao

2016

To: Dean Michael R. Heithaus  
College of Arts, Sciences and Education

This dissertation, written by Cen Gao, and entitled Vortex Rossby Wave Propagation in Three Dimensional Tropical-Cyclone-Like Baroclinic Vortices, having been approved in respect to style and intellectual content, is referred to you for judgment

We have read this dissertation and recommend that it be approved.

---

Hugh Willoughby

---

Haiyan Jiang

---

Robert Burgman

---

Tao Li

---

Ping Zhu, Major Professor

Date of Defense: June 28, 2016

The dissertation of Cen Gao is approved.

---

Dean Michael R. Heithaus  
College of Arts, Sciences and Education

---

Andrés G. Gil  
Vice President for Research and Economic Development  
and Dean of the University Graduate School

Florida International University, 2016

ABSTRACT OF THE DISSERTATION  
VORTEX ROSSBY WAVE PROPAGATION IN THREE DIMENSIONAL  
TROPICAL-CYCLONE-LIKE BAROCLINIC VORTICES

by

Cen Gao

Florida International University, 2016

Miami, Florida

Professor Ping Zhu, Major Professor

This study aims to advance our understanding of the inner-core dynamics of tropical cyclones (TCs) from the perspective of vortex Rossby waves (VRWs) through investigating wave kinematics, propagation feature, and wave-mean-flow interaction in three dimensional TC-like baroclinic vortices. Using the Wenzel-Kramers-Brillouin analysis in the asymmetric balanced model framework, the generalized wave dispersion relation, group velocities, and stagnation radius/height of VRW wave-packets in both pseudo-height and isentropic coordinates are derived. It is found that the VRW dispersion relation associated with baroclinic vortices in an isentropic coordinate has the same format as that of barotropic vortices in a pseudo-height coordinate. However, baroclinicity causes the vertical wavenumber to increase, resulting in wave propagation features different from those in barotropic vortices. The stagnation radius and height are strictly constrained by the geometry of the 'critical' surface determined by the initial properties of wave-packets and basic-state vortices. Baroclinicity substantially promotes the vertical propagation of VRWs but suppresses the corresponding wave radial propagation under the constraint of the 'critical' surface. Asymmetries excited at the surface are trapped in the low layer with

substantial radial propagation, whereas the waves excited in the low to mid-troposphere in the vortex inner-core region can effectively propagate upward but their radial propagation is suppressed. Only low azimuthal wavenumber asymmetries can have meaningful radial and vertical propagation.

The theoretical prediction of wave kinematics is confirmed by the non-hydrostatic simulations performed by the Weather Research and Forecasting (WRF) model. The WRF simulations show that the VRWs in baroclinic vortices can be classified into a surface quasi-barotropic regime and an upper baroclinic regime. The distinct wave kinematics in these two regimes results in different wave-mean-flow interaction. The former causes a strong vortex spin-up just outside the center of the initial asymmetry similar to those in barotropic vortices, whereas the latter confines the mean angular momentum inside the center of initial asymmetry but substantially supports the upward transport of angular momentum. The vortex intensification in baroclinic vortices is shown to be governed by the tilting of wave phase, the radial and vertical eddy momentum fluxes, and the vortex symmetric response to asymmetric momentum forcing.

## TABLE OF CONTENTS

CHAPTER	PAGE
1 INTRODUCTION .....	1
1.1 Basic TC Dynamics and Axisymmetric Intensification Theory .....	2
1.2 Asymmetric Features and Dynamics of TCs .....	6
1.3 Wave-Mean-Flow Interaction and TC Intensification .....	9
1.4 Objectives and Organization of Dissertation .....	12
2 VRW Theory In Pseudo-Height Coordinates .....	17
2.1 Asymmetric Balance Model .....	17
2.2 Governing Equations .....	19
2.3 WKB Analysis .....	22
2.4 Summary .....	28
3 VRW Theory in Isentropic Coordinates .....	30
3.1 Introduction .....	30
3.2 Transformation between Pseudo-Height and Isentropic Coordinates .....	30
3.3 Geopotential Perturbation Tendency Equation in Isentropic Coordinates .....	32
3.4 WKB Analyses .....	33
3.5 ‘Critical’ Surface of Radial and Vertical Propagation of VRWs .....	37
3.6 Summary .....	41
4 Impact of Baroclinicity on VRW Propagation .....	42
4.1 Introduction .....	42
4.2 Initial Condition of TC-Like Vortices .....	42
4.3 Simplest Baroclinicity: Constant Vertical Shear of Tangential Velocity .....	44
4.4 Extension to More Realistic Baroclinic TC Vortex .....	51
4.5 Summary and Conclusions .....	53
5 WRF Simulation of VRW Propagation in Baroclinic TC-like Vortices.	
Part I: Asymmetric Structure and Evolution .....	71
5.1 Introduction .....	71
5.2 Overview of WRF Model Setup .....	74
5.3 Basic State Vortices and Asymmetry Initialization .....	75
5.3.1 Methodology of Balanced Vortices Construction .....	75

5.3.2 Baroclinic Flow and Quasi-Barotropic Flow in 3D Baroclinic Vortices .....	77
5.3.3 Experiment Design and Asymmetry Initialization .....	79
5.4 Verification of VRW Propagation .....	80
5.5 VRW Propagation Features in Baroclinic Vortices .....	83
5.5.1 Propagation of $W_{n-2}$ Asymmetry in the Quasi-barotropic Regime of a Baroclinic Vortex .....	83
5.5.2 Propagation of $W_{n-2}$ Asymmetry in the Baroclinic Regime of a Baroclinic Vortex .....	85
5.5.3 Propagation of $W_{n-1}$ Asymmetries .....	88
5.6 Summary .....	90
6 WRF Simulation of VRW Propagation in Baroclinic TC-like Vortices.	
Part II: Wave-Mean-Flow Interaction .....	110
6.1 Introduction .....	110
6.2 Budget Equation of Mean Tangential Velocity .....	110
6.3 A Review of Wave-Mean-Flow Interaction in Barotropic Vortices .....	113
6.4 Wave-Mean-Flow Interaction in 3D Baroclinic Vortex .....	117
6.4.1 Wave Phase Tilting .....	117
6.4.2 Tangential Wind Budget Analyses .....	119
6.4.3 Vortex Mean Flow Change Induced by Asymmetry .....	121
6.5 Summary .....	125
7 Summary and Conclusions .....	138
LIST OF THE REFERENCE .....	144
VITA .....	152

## LIST OF FIGURES

FIGURE	PAGE
Fig. 1.1: GOES-12 visible image of Hurricane Isabel (2005). .....	14
Fig. 1.2: Schematic sketch of vortex Rossby waves associated with a potential vorticity (PV) annulus. Red circle indicates the ring of peak PV .....	15
Fig. 1.3: Change in tangential velocity due to the wave activities as function of non-dimensional radius where $r_m$ is the radius of maximum wind. ....	16
Fig. 4.1: Basic-state swirl profiles for hurricane-strength and tropical-storm-strength vortices used in this study. (a): Tangential velocity (m/s); (b): relative vorticity (1/s).....	56
Fig. 4.2: Radius-height plots of tangential velocity (m/s, color shades) and vertical gradient of tangential velocity ( $\times 10^{-3}$ 1/s, contours). (a): Hurricane-strength vortex with strong baroclinicity; (b): Hurricane-strength vortex with weak baroclinicity; (c): Tropical-storm-strength vortex with strong baroclinicity; (d): Tropical-storm-strength vortex with weak baroclinicity.....	57
Fig. 4.3: Time variation of radial wavenumber $k$ and vertical wavenumber $m$ for azimuthal wavenumber 2 and 3 for the hurricane-strength vortex constructed in this study. ....	58
Fig. 4.4: Radial (a) and vertical (b) group velocities of wavenumber-1, wavenumber-2, and wavenumber-3 in hurricane-strength 2D non-divergent, 3D barotropic, and 3D baroclinic vortex. ....	59
Fig. 4.5: Wave radial trajectories (upper row) and vertical trajectories (bottom row) of wavenumber-1, wavenumber-2, and wavenumber-3 in 2D nondivergent (green), 3D barotropic (red), and 3D baroclinic (blue) vortices. The dashed vertical lines indicate the stagnation radii and heights computed by Eqs. 2.32-2.33. ....	60
Fig. 4.6: Structure of planetary Rossby wave propagation in a barotropically stratified fluid (after Cushman-Roisin and Beckers 2006). ....	61
Fig. 4.7: Sensitivity of stagnation radii (a) and stagnation heights (b) to initial radial wavenumber, $k_0$ . ....	62
Fig. 4.8: Sensitivity of stagnation radii (a) and stagnation heights (b) to initial vertical wavenumber, $m_0$ . ....	63

Fig. 4.9: Sensitivity of stagnation radii (a) and stagnation heights (b) to the radius where the asymmetry is initially placed. ....	64
Fig. 4.10: Sensitivity of stagnation radii (a) and stagnation heights (b) to RMW. ....	65
Fig. 4.11: Sensitivity of stagnation radii (a) and stagnation heights (b) to maximum tangential velocity. ....	66
Fig. 4.12: Stagnation radii (km, color shades) for azimuthal wavenumber-1 asymmetries excited at different radii (x-axis) and heights (y-axis) for (a): a hurricane-strength vortex with strong baroclinicity (L=5000); (b): a hurricane-strength vortex with weak baroclinicity (L=7500); (c): a tropical-storm-strength vortex with strong baroclinicity (L=5000); and (d): a tropical-storm-strength vortex with weak baroclinicity (L=7500). ....	67
Fig. 4.13: The same as Fig. 4.12 but for azimuthal wavenumber-2 asymmetries. ....	68
Fig. 4.14: Stagnation height (km, color shades) for azimuthal wavenumber-1 asymmetries excited at different radii (x-axis) and heights (y-axis) for (a): a hurricane-strength vortex with strong baroclinicity (L=5000); (b): a hurricane-strength vortex with weak baroclinicity (L=7500); (c): a tropical-storm-strength vortex with strong baroclinicity (L=5000); and (d): a tropical-storm-strength vortex with weak baroclinicity (L=7500). ....	69
Fig. 4.15: The same as Fig. 4.14 but for azimuthal wavenumber-2 asymmetries. ....	70
Fig. 5.1: Radius-height distribution of initial azimuthal velocity for the hurricane-strength vortex with weak baroclinicity. ....	92
Fig. 5.2: Radius-height distribution of initial azimuthal velocity for the hurricane-strength vortex with strong baroclinicity. ....	93
Fig. 5.3: Radius-height distribution of initial mean pressure (mb), which is the same for both weak and strong baroclinic vortices. ....	94
Fig. 5.4: Radius-height distribution of initial mean potential temperature (K) for both weak and strong baroclinic vortices. ....	95
Fig. 5.5: a) Initial radius-height distribution of the vortex $\beta$ effect parameter $q_f$ (color shades; scaled by $10^{-8}m^{-1}s^{-1}$ ) and vortex radial shear $r\bar{\Omega}_r$ (dashed lines; scaled by $10^{-3}m^{-1}s^{-1}$ ) of the weak baroclinic vortex; b) is the same as a) except that the dashed lines indicates the vortex vertical shear $\bar{v}_z$ . ....	96
Fig. 5.6: The same as Fig 5.5 but for the strong baroclinic vortex. ....	97

Fig. 5.7: Horizontal structure of initial asymmetric vorticity for a) azimuthal wavenumber one (wn-1) and b) azimuthal wavenumber two (wn-2) at the height where the asymmetry amplitude is the maximum (i.e., $z=0\text{km}$ for LB01 and HB01; $z=5\text{km}$ for LB02 and HB02).	98
Fig. 5.8: Radius-height distribution of initial basic-state symmetric vorticity (solid lines) and asymmetric perturbation vorticity (color shades) for (a) HB01, (b) HB02, (c) LB01, and (d) LB02. Vorticity has been multiplied by a factor of $10^5$ .	99
Fig. 5.9: Time–radius Hovmoller plots of the real part of the Fourier coefficients of (a) relative vorticity and (b) vertical velocity at 1 km altitude for wn-2 asymmetry in experiment LB01. Since the negative components of Fourier coefficients are merely the mirror of the positive components, for a clear illustration only positive components of Fourier coefficients are plotted. Triangle marks the center of the initial asymmetry, $r_c = r_m$ . Dashed lines indicate the outward propagation of VRW packets.	100
Fig. 5.10: The same as Fig 5.9 but for the wn-2 asymmetry at $z=2.5\text{km}$ in experiment LB02. The thin arrow in (a) indicates the upward propagation of wave packets.	101
Fig. 5.11: Height-time plots of wn-2 vorticity at the radius of 30 km in experiment LB02. Triangle marks the height where the center of initial asymmetry is placed (i.e., $z_c = 5\text{km}$ ).	102
Fig. 5.12: Radial-height distribution of wn-2 vorticity (color shades) and vertical gradient of azimuthal-mean tangential wind (dashed contours) after (a) 2 h, (b) 4 h, (c) 6 h and (d) 12 h from experiment LB01. Vorticity ( $s^{-1}$ ) has been multiplied by a factor of $10^5$ . Solid horizontal arrows in (d) indicate the radial propagation of wave packets in quasi-barotropic condition. Triangle marks the radius where the center of initial asymmetry is placed.	103
Fig. 5.13: The same as Fig 5.12 but for wn-2 asymmetry in experiment LB02 in which the center of initial asymmetry is placed at $z=5.0\text{ km}$ .	104
Fig. 5.14: (a) Horizontal plane view of positive Fourier coefficients of wn-2 vorticity at $z=0.5\text{ km}$ at 20 h in experiment LB01. (b): The same as (a) but for wn-2 asymmetry at $z=5\text{ km}$ at 20 h in experiment LB02. Vorticity ( $s^{-1}$ ) has been multiplied by a factor of $10^5$ . Note that the negative Fourier coefficients show the same structure but are $90^\circ$ off phase.	105
Fig. 5.15: Radial-height distribution of basic-state vorticity (black contours) and wn-2 asymmetric vorticity (color shades) at 6h for experiments (a): LB01, (b): LB02, (c): HB01, and (d): HB02. Vorticity ( $s^{-1}$ ) has been multiplied by a factor of $10^5$ . Solid arrows in each panel indicate the propagation of wave packets.	106

Fig. 5.16: Radial-height distribution of wn-1 vorticity (color shades) and vertical gradient of azimuthal-mean tangential wind (dashed contours) after (a): 4 h, (b): 6 h, (c): 12 h, and (d): 20 h from experiment LB01. Vorticity ( $s^{-1}$ ) has been multiplied by a factor of $10^5$ . Solid horizontal arrows in (d) indicate the radial propagation of wave packets in quasi-barotropic condition. Triangle marks the radius where the center of initial asymmetry is placed. ....	107
Fig. 5.17: The same as Fig 5.16 but for wn-1 asymmetry in experiment LB02 in which the center of initial asymmetry is placed at $z=5.0\text{km}$ . ....	108
Fig. 5.18: (a) Horizontal plane view of positive Fourier coefficients of wn-1 vorticity at $z=0.5\text{ km}$ at 20 h in experiment LB01. (b): The same as (a) but for wn-1 asymmetry at $z=5\text{ km}$ at 20 h in experiment LB02. Vorticity ( $s^{-1}$ ) has been multiplied by a factor of $10^5$ . Note that the negative Fourier coefficients are the axisymmetric mirror of positive Fourier coefficients. ....	109
Fig. 6.1: Change in azimuthal-mean tangential wind induced by a wn-2 asymmetry in the simulation of a 2D non-divergent barotropic model. (After Montgomery and Kallenbach 1997). ....	127
Fig. 6.2: Examples of the horizontal tilting of perturbations of (a) growing and (b) decaying cases in an idealized vortex in which the radial gradient of the mean angular velocity is set to a negative value such that the tangential wind speed is the same at all three radii indicated by the thin solid curves. Thick solid lines indicate a perturbation flow. Thin dashed lines separate regions of the perturbation that have opposite signs of tangential and radial wind direction. Thick dashed arrows represent the positive radial direction. (After Young and Williams 2005). ....	128
Fig. 6.3: (a), (c) and (e): Positive Fourier coefficients of wn-2 asymmetric vorticity at $z=0.5\text{km}$ as function of azimuthal angle at 30 min, 4 h, and 8 h respectively in experiment LB01. (b), (d) and (f): The same as (a), (c), and (e) but for LB02 at $z=5.0\text{km}$ . Vorticity ( $s^{-1}$ ) has been multiplied by a factor of $10^5$ . The increase (decrease) of a phase line with azimuthal angle indicates an upshear (downshear) tilting. ....	129
Fig. 6.4: The same as Fig 6.3 but for the wave phase tilting in the vertical at the radius of $r=60\text{km}$ . ....	130
Fig. 6.5: (a) and (b): Radius-height plot of the simulated azimuthal-mean tangential wind tendency ( $ms^{-1}h^{-1}$ ) directly from the model output at 2 h and 4 h respectively in experiment LB01. (c) and (d): the diagnosed tendency ( $ms^{-1}h^{-1}$ ) associated with the eddy momentum divergence in the budget equation. (e) and (f): the diagnosed tendency	

$(m s^{-1} h^{-1})$ associated with the mean advection in the budget equation. Solid contours in figures indicate the radial momentum flux ( $m^2 s^{-2}$ ). .....	131
Fig. 6.6: The same as Fig. 6.5 but for LB02 at 2 h and 6 h. ....	132
Fig. 6.7: The same as Fig. 6.6 but for HB02. ....	133
Fig. 6.8: (a), (c), and (e): Change in basic-state tangential wind $\Delta \bar{v}$ (solid/dashed contours) and vorticity $\Delta \bar{\zeta}$ (color shades) at 1 h for LB01, LB02, and HB01, respectively. (b), (d), and (f): The same as (a), (c), and (e) but for the fields at 6 h. The maximum acceleration (positive $\delta \bar{v}$ ) and the position where it occurs are indicated by the legend in each figures. ....	134
Fig. 6.9: (a) and (b): Evolution of the change in azimuthal-mean tangential wind at $z=0.5$ km and $z=5.0$ km in LB01, respectively. Thin dashed line indicates the zero line. Thick dashed line and triangle indicate the radius where the center of initial asymmetry is placed. ....	135
Fig. 6.10: The same as Fig 6.9 but for the change in azimuthal-mean tangential wind at $z=2.5$ km and $z=7.5$ km in LB02. ....	136
Fig. 6.11: The same as Fig 6.10 but for HB02 with strong vortex baroclinicity. ....	137

## CHAPTER 1: INTRODUCTION

Tropical cyclones (TCs), with their triple threats of violent winds, heavy rainfall, and storm surge, are one of the most destructive forces of nature that can bring devastation to coastal areas. The strong and deadly landfalling TCs, such as Hurricane Katrina and Super Typhoon Haiyan, can kill thousands of people, cause billions of dollars in property damage, and result in immense human suffering. Timely and accurate TC forecasts allow for advanced warning that can save lives and property. The National Hurricane Center (NHC) has increasingly relied upon guidance from the forecasts made by operational numerical weather prediction (NWP) models to issue TC track (position) and intensity (strength) advisory. Tropical cyclone track forecasting has been improving substantially over the past couple of decades, whereas no such improvement is seen in TC intensity forecasts (Rappaport et al. 2009). The disparity in forecasting skills lies in the fact that TC tracks and intensity are governed by different processes. The track of a TC is determined primarily by the large-scale steering flow. The steady improvement in predicting large-scale atmospheric fields by operational NWP models owing to the ever increasing model resolution and advances in observational network and modeling technology is the main reason for the substantial reduction in track forecasting error. In contrast, TC intensification is not only modulated by the external forcing, such as the large-scale atmospheric fields and underlying sea surface temperature (SST), but also depends largely on the TC internal processes. An accurate prediction of TC intensity is difficult mainly because that TC internal processes are highly convective in nature and involve in a complicated interaction spanning a spectrum of scales from the TC vortex-scale flow down to turbulence (Marks

and Shay 1998). To date, details of how the interactions of internal processes governing the rate of the TC intensification remains poorly understood. Breaking the deadlock of the TC intensity forecasts has been a principal goal of both weather forecasters and researchers.

## **1.1 Basic TC Dynamics and Axisymmetric Intensification Theory**

To the first-order approximation, a TC may be regarded as an axisymmetric vortex that satisfies the hydrostatic balance in the vertical and gradient wind balance in a horizontal plane. The basic-state dynamic and thermodynamic fields that hold such an axisymmetric vortex follow the so-called thermal wind relation, which imposes a strong constraint on the evolution of a TC vortex driven by the diabatic heating and friction. Acting alone, the diabatic heating and friction would drive the TC flow away from the thermal wind equilibrium. Thus, in order for the vortex to maintain the equilibrium, a transverse (or secondary) circulation is required to oppose the effects of the forcing. The stream-function of tangential velocity and vertical velocity of this overturning circulation associated with such a simplified axisymmetric TC vortex in an azimuthally-averaged radial-height plane can be obtained by solving a diagnostic equation, known as the Sawyer-Eliassen (SE) balance equation first derived by Eliassen (1951). The SE balance equation provides a fundamental physical basis for describing the evolution of a rapidly-rotating vortex. Shapiro and Willoughby (1982) first solved the SE equation for a point source of diabatic heating placed in a TC-like vortex. They showed that a heating source located in the middle troposphere can induce inflow in the lower troposphere and outflow in the upper troposphere beyond the radius of the source. For a similar reason, in order to maintain a

state of balanced flow, a momentum sink associated with the surface friction will induce inflow in the boundary layer and outflow above the layer.

The spin-up of an axisymmetric balanced vortex can be understood in terms of absolute angular momentum,

$$M = rv + \frac{1}{2} fr^2 \quad (1.1)$$

where  $r$  is the radius from the vortex center,  $v$  is the azimuthal-mean tangential velocity,  $f$  is the Coriolis parameter. The governing equation of  $M$  may be written as,

$$\frac{DM}{Dt} = rF_\lambda \quad (1.2)$$

where  $F_\lambda$  is the net force in the azimuthal direction, and  $rF_\lambda$ , thus, represents a torque acting

on a fluid parcel.  $\frac{D}{Dt} = \frac{\partial}{\partial t} + u \frac{\partial}{\partial r} + w \frac{\partial}{\partial z}$  is the material derivative following fluid

particles in the axisymmetric flow. In the absence of external forcing,  $M$  is materially conserved. Thus, Eq. (1.1) indicates that as air parcels move radially inward (i.e., the decrease in  $r$ ), it will lead to the spin-up of the vortex (i.e., the increase in  $v$ ).

Over the years, several theories from the axisymmetric perspective have been proposed to explain the spin-up of a vortex, or intensification of TCs. These include (a) the linear conditional instability of the second kind (CISK) mechanism (Charney and Eliassen 1964; Ooyama 1964; Carrier 1971), (b) the Ooyama's cooperative intensification mechanism (Ooyama 1969, 1982; Willoughby 1990, 1995), and (c) the Emanuel's thermodynamic air-sea interaction mechanism (Rotunno and Emanuel 1987; Emanuel 1989; Emanuel et al. 1994; Emanuel 1997, 2003; Holton 2004).

The CISK mechanism recognizes that the surface air spirals into the center of a low pressure and forces air to rise. The adiabatic cooling causes moisture to condense and release latent heat, which warms the surrounding atmosphere and causes the surface pressure to drop. As the surface radial pressure gradient increases, more moist air converges towards the center of the vortex and results in more latent heating release. The positive feedback intensifies the storm. Later, it was realized that the statistical equilibrium of water substance assumed by the CISK implies that the cumulus convection consumes water (not directly the convective available potential energy, CAPE) at the rate the same as that supplied by the large-scale system. Raymond and Emanuel (1993) argued that such a closure used by the CISK fundamentally violates the causality since convection is not caused by the large-scale water supply. Emanuel et al. (1994) further pointed out if it were the large-scale circulation to replenish the moisture needed for convection as assumed by the CISK, then, vortex intensification would be just as likely to occur over land as over the ocean. A key problem is that the CISK completely overlooks the central role of surface moisture fluxes in accomplishing the remoistening.

Ooyama recognized the limitation of the linear CISK mechanism and developed what was later termed as the cooperative intensification theory for TCs (Ooyama 1969; 1982; 1997). Although the dynamic picture and the role of cumulus convection depicted by the cooperative intensification theory to a certain extent is similar to that described by the linear CISK, Ooyama's model did contain a simple bulk aerodynamic representation of the surface moisture flux, which increases with the surface wind speed and the degree of the air-sea moisture dis-equilibrium. But Ooyama did not discuss the consequences of the wind speed dependence.

Although the evaporation of water from the underlying ocean has long been recognized as the ultimate energy source for tropical cyclones (Kleinschmidt 1951; Riehl 1954; Malkus and Riehl 1960; Ooyama 1969), Emanuel and colleagues (Emanuel 1986; Rotunno and Emanuel 1987; Emanuel 1989; Emanuel et al. 1994; Emanuel 1997, 2003; Holton 2004) first emphasized the importance of air-sea interactions in the TC intensification processes. The central part of the wind-induced surface heat exchange (WISHE) mechanism was the positive feedback between the wind-speed dependent moisture fluxes and the tangential velocity of the broad-scale vortex. The convective available potential energy was shown to be non-necessary in the storm environment for intensification. Emanuel (2003) specifically describes the intensification process as follows: ‘Intensification proceeds through a feedback mechanism wherein increasing surface wind speeds produce increasing surface enthalpy flux..., while the increased heat transfer leads to increasing storm winds.’

All three intensification mechanisms are established on the basis of the axisymmetric considerations. Neither buoyant updrafts and cold downdrafts nor any other asymmetries are considered in theories. However, observations show that rapidly-rotating storms are frequently accompanied by ‘bursts’ of intense convection (e.g. Gentry et al. 1970; Black et al. 1986; Marks et al. 1992; Molinari et al. 1999). The observed TC asymmetries raise questions on the applicability of purely axisymmetric theories to the intensification processes of TCs with marked flow asymmetries: How does vortex intensification proceed in three-dimensional models and in reality? Are there fundamental differences between the intensification process in a three-dimensional model and that in an axisymmetric model?

## 1.2 Asymmetric Features and Dynamics of TCs

Both observations and numerical simulations show that asymmetric features, which are intimately linked to the deep convection growing in a rotation-rich environment and evolve at a much shorter time scale than that of axisymmetric evolution, can play an important role in TC intensification. The TC inner-core asymmetries can be readily inferred from the polygonal eyewall frequently shown in satellite and radar observations. For example, Lewis and Hawkins (1982) showed clear images of polygonal eyewall from hexagons to triangles from land-based radar observations of Hurricanes David (1979); Anita (1977); Caroline (1975); and Betsy (1965) and airborne radar observations of Debbie (1969) and Anita (1977). The convoluted swirling mesovortices associated with the polygonal eyewall were also reported in many other observational studies (e.g., Muramatsu 1986; Black and Marks 1991; Willoughby and Black 1996; Kossin et al. 2002; and Knaff et al. 2003). Figure 1.1 shows an example of convoluted swirling mesovortices embedded in the eyewall of Hurricane Isabel (2005) in the GOES satellite visible image.

Polygonal eyewalls were first viewed as a superposition of internal-gravity waves with differing wavenumbers and periods by Willoughby (1978) and Kurihara (1976). Later, it was found that many characteristics of polygonal eyewall can be well explained by the vortex Rossby waves (VRWs), a concept first introduced by MacDonald (1968). The basic wave mechanism of VRWs may be schematically illustrated by Fig. 1.2. The eyewall deep convection results in an annular ring of high potential vorticity (PV) with large PV gradient pointing radially inward and outward on the inner and outer edges of PV annulus respectively. Similar to the planetary vorticity gradient, which supports planetary Rossby waves, the basic-state PV gradients of a TC serves as a “waveguide” to allow for cyclonic

propagation of VRWs on the inner edge and anti-cyclonic propagation of VRWs on the outer edge of the PV annulus superimposed on the TC mean tangential flow. If the counter propagating VRWs have the same value of angular velocity relative to the Earth, that is, to be phase locked, each wave will make the other grow exponentially leading to the barotropic instability.

By analyzing the linearized 2D non-divergent vorticity equation in a cylindrical coordinate, Schubert et al. (1999, hereafter S99) was able to derive the very first analytical solution of barotropic instability of VRWs associated with an annular vorticity ring and showed that the instability depends strongly on the initial structure of the vortex. Their theoretical analyses were confirmed by a numerical simulation using an unforced 2D barotropic nondivergent model, which shows that exponential growth of wavenumber-4 disturbances can occur on both sides of the eyewall ring and result in the generation of mesovortices and polygonal eyewall structure. The S99's barotropic instability theory of VRWs ultimately provides a physically sound explanation of the formation and development of eyewall mesovortices. The basic findings of S99 obtained in the highly idealized 2D framework were confirmed by 3D simulations. Using a linearized non-hydrostatic anelastic model, Nolan and Montgomery (2002) and Nolan and Lewis (2003) showed that axisymmetric 3D TC-like vortices with CAT-1 and CAT-3 strength are barotropically unstable to low wavenumber perturbations and demonstrated that the heat and momentum fluxes induced by asymmetric eddies can have a substantial impact on TC vortex structure and intensity.

In addition to the azimuthally propagating VRWs illustrated in Fig. 1.2, using the same 2D non-divergent barotropic model as that used by S99, Montgomery and Kallenbach

(1997, hereafter MK97) demonstrated that VRWs can also propagate radially supported by the radial gradient of the basic-state PV in a sheared vortex monopole. Their Wenzel-Kramers-Brillouin (WKB) analyses showed that as VRWs propagate radially outward the radial shearing effect can cause their radial wavenumbers to continuously increase, which reduces the group velocities to slow down the wave packets. The outward propagating VRW-packets eventually ceased at the stagnation radii where the group velocity goes to zero for sufficiently large radial wavenumbers.

The mechanism of VRW propagation depicted by MK97 was verified by Moller and Montgomery (2000, hereafter MM00) who studied the VRW propagation in three dimensional (3D) vortices constructed using the same radial swirl profiles of MK97 in the asymmetric balance (AB) model framework. The theoretical analyses of VRWs shown in MM00 confirmed the basic findings of MK97 but revealed several interesting features of VRW propagation in 3D barotropic vortices. First, VRWs excited in the inner-core region not only propagate radially outward but also can propagate upward. Second, the radial shear of the vortex symmetric flow, which causes the radially propagating VRWs to cease at the stagnation radii, is also responsible for slowing down VRWs in the vertical propagation. As a result, vertically propagating VRWs also have stagnation heights where vertical group velocity goes to zero when the radial wavenumber becomes sufficiently high. However, unlike the radial wavenumber, which increases as wave-packets propagate radially outward, MM's derivation ends up with a vertical wavenumber that does not change with time as wave packets propagate upward in barotropic vortices. Lastly, only wavenumber-1 asymmetry shows significant upward propagation in MM's simulations,

whereas higher wavenumber asymmetries have much lower stagnation heights than that of the wavenumber-1 asymmetry, and thus, they are basically trapped in the low layer.

McWilliams et al. [2003, hereafter MW03] generalized the VWR theory of MK97 and MM00 in a conservative, rotating, and  $f$ -plane shallow-water equation framework. The slowly varying formalism (or ‘ray’ theory) derived by MW03 is more complete and accurate than the local Taylor expansion used by MK97 and MM00. Moreover, MW03 study revealed interesting features of the interaction between the radial propagation of VRW-packets and the vortex mean flow. The pioneering work of MK97, MM00 and MW03 greatly advanced our understanding of propagation and evolution of TC asymmetries in the context of VRW framework.

### **1.3 Wave-mean-flow Interaction and TC Intensification**

One of the important finding of MK97 is that the eddy energy associated with asymmetries can be axisymmetrized in the mean flow of a vortex. Using the numerical simulations of perturbed monopole vortices by a 2D nondivergent barotropic model, MK97 studied the change in mean tangential velocity induced by wave activities. They showed that the inward eddy momentum fluxes lead to the redistribution of vortex mean flow and the resultant change in mean tangential velocity as the function of radius exhibits a reversed “S” shape illustrated in Fig. 1.3. The zero tangential velocity change corresponds well with the stagnation radius of radially propagating VRWs derived from the WKB analyses. For vertical disturbances excited near the radius of maximum wind (RMW), the maximum acceleration of the mean tangential velocity due to the inward momentum fluxes occurs outside the radius where the initial asymmetries are placed and the flow acceleration is

larger than the deceleration, which is notably different from the case without the vortex " $\beta$ " effect. On the basis of this result, MK97 argued that if the asymmetric disturbances, excited in the TC inner-core region, can continue for several eddy-turnovers without disrupting the outward propagation of the disturbances, a net inward horizontal vorticity flux across a closed circuit will accelerate the circulation of the circuit, and hence, result in a stronger monopolar vortex. The pioneering work on radial propagation of VRWs shown in MK97 established a foundation for understanding the internal mechanisms of TC intensification via wave-mean-flow interaction.

Moller and Montgomery (1999) and MM00 extended MK97's derivations and simulations in the 2D non-divergent model to the 2D and 3D AB model framework and confirmed the basic finding of MK97's wave-mean-flow interaction mechanism that the wave energy can be axisymmetrized into the vortex mean flow. These results from VRW perspective are consistent with other studies that vortex axisymmetrization is found to be a universal dynamic process for monopole vortices (Melander et al. 1987; McCalpin 1987; Carr and Williams 1989; Sutyrin 1989; Guinn and Schubert 1993; Holland and Dietachmayer 1993; Ritchie and Holland 1993; Smith and Montgomery 1995).

However, during the life cycle of TCs, the monopole shaped basic state vorticity may only occur in the tropical storms or the developing stages of weak hurricanes. The radial profiles of PV of intensifying or mature TCs should exhibit annulus-like shape. Although no theoretical study is available, the wave-mean-flow interaction associated with PV annuluses has been studied using numerical simulations. Wang (2001 and 2002) showed the asymmetric structure in the inner-core region of a vortex annulus was dominated by wavenumber-1 and-2 VRWs in a simulation using a hydrostatic primitive

equation model. Chen and Yau (2000) validated the VRW propagation in a simulation of a perturbed annulus vortex. Both the outward propagating and inward propagating VRWs were found owing to the opposite PV radial gradient inside and outside the PV ring. The characteristic of those waves are similar to those depicted by the MK97's and MM00's VRW theory. And in a further investigation using the empirical normal mode analysis, Chen et al. (2003) confirmed that the leading modes in the vortex core region are indeed VRWs. The waves coupled well with convection lead to the appearance of inner spiral bands. These studies suggested that VRWs do exist in more realistic annulus vortices.

The TC asymmetric features and wave-mean-flow interaction have been shown to have important implications on vortex intensification. However, while some studies (e.g. Heymsfield et al. 2001; Montgomery and Enagonio 1998; Nguyen et al. 2008) found that the progressive segregation, merger, and axisymmetrization of TC inner-core asymmetries and the induced low-level convergence by these features are fundamental to the intensification process, other studies, however, suggested that asymmetric features can also have a negative effect on TC intensification. For example, Nolan and Montgomery (2002) argued that the direct spindown of eyewall by eddies resulting from barotropic vortex breakdown could weaken the TC intensity at the mature stage. Wu and Braun (2004) showed that the eddy momentum flux associated with the TC inner-core asymmetries could weaken a TC directly by producing a deceleration of the azimuthal mean tangential velocity in the vicinity of radius of maximum wind (RMW) and indirectly by inducing an anomalous secondary circulation opposite of the primary secondary circulation. To date, many aspects of asymmetric dynamics and their role in storm intensification remain poorly understood.

## 1.4 Objectives and Organization of Dissertation

Although MM00's work greatly advanced our understanding of VRW propagation and wave-mean-flow interaction in a 3D framework, their theoretical analysis does not include the effect of vortex basic-state baroclinicity. Thus, it remains unclear whether the results of MK97, MM00, and MW03's theoretical analyses can be extended to baroclinic vortices. How baroclinicity of the symmetric vortices affects VRW propagation and wave-mean-flow interaction is an important question that needs to be addressed. In a recent study, using a two-layer model Peng et al. (2014a and 2014b) investigated the effect of baroclinicity on vortex axisymmetrization. They showed that the same initial asymmetric perturbation can have important effects on symmetric vortices depending on the baroclinicity of basic-state vortices. However, since a layered model does not support the vertical propagation of VRWs, it is unknown if the main conclusions of Peng et al. [2014a and 2014b] will be substantially affected by the vertical propagation of VRWs. Therefore, there is a need to further investigate the impact of baroclinicity on VWR propagation and wave-mean-flow interaction in 3D vortices under continuous stratifications that support both vertical and radial propagation of VRWs.

In this study, a local WKB analysis similar to that used in MK97 and MM00 is used to analyze the VRW propagation in baroclinic vortices in the 3D AB model framework. On the basis of the derived dispersion relation, group velocities, and stagnation radii and heights of VRWs, we aim to identify the important difference of VRW propagation in barotropic and baroclinic vortices and investigate how the key parameters that determine the basic-state vortices and asymmetric disturbances affect VRW propagation in barotropic and baroclinic vortices. This dissertation is organized as follows. Chapter 2 presents the

VRW theory including the derivation of dispersion relation, radial/vertical group velocities, stagnation radii and heights of VRWs in baroclinic conditions in the pseudo-height coordinate. The corresponding VRW theory in the isentropic coordinate is presented in Chapter 3. The VRW radial and vertical propagation in baroclinic monopole swirl vortices and the impact of baroclinicity on VRW propagation are discussed in Chapter 4. Chapter 5 presents the validation of theoretically derived VRWs using the numerical simulations by the non-hydrostatic Weather Research & Forecasting (WRF) model. Investigation of wave-mean-flow interaction and its implication on TC intensification are presented in Chapter 6 followed by a summary and discussion of this dissertation research in Chapter 7.

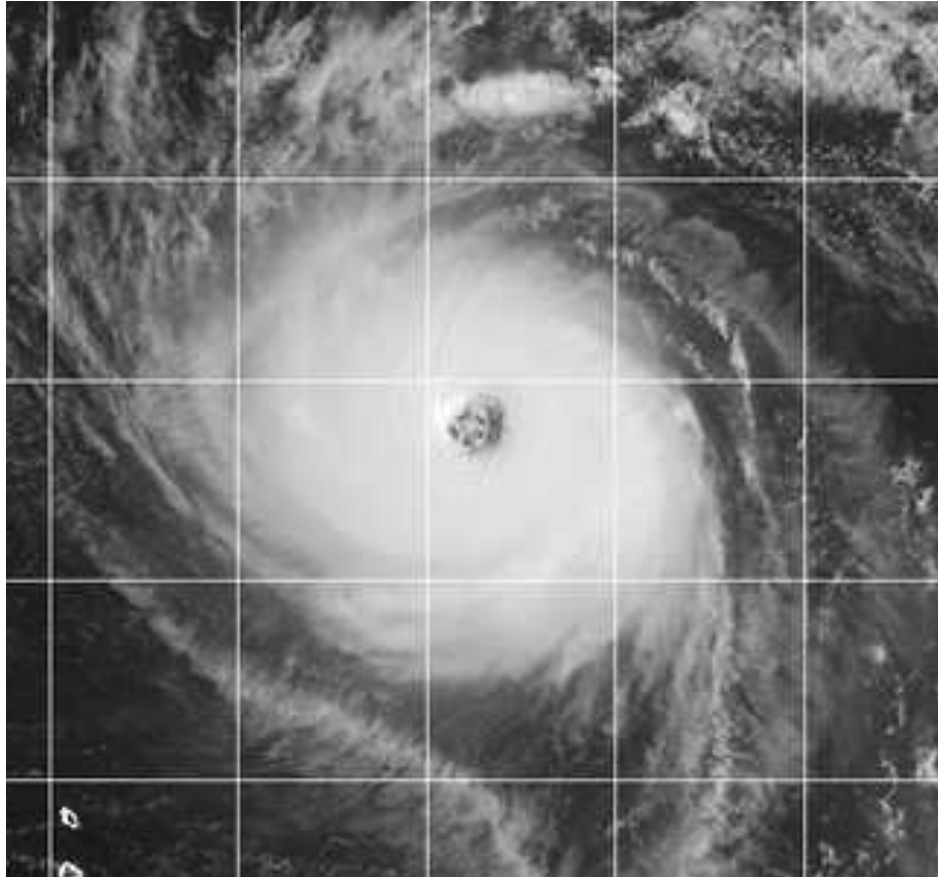


Fig. 1.1: GOES-12 visible image of Hurricane Isabel (2005).

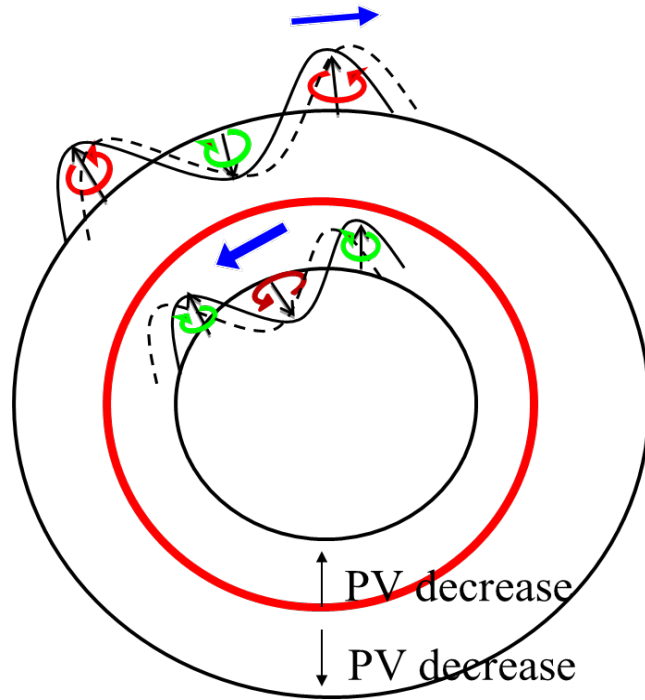


Fig. 1.2: Schematic sketch of vortex Rossby waves associated with a potential vorticity (PV) annulus. Red circle indicates the ring of peak PV.

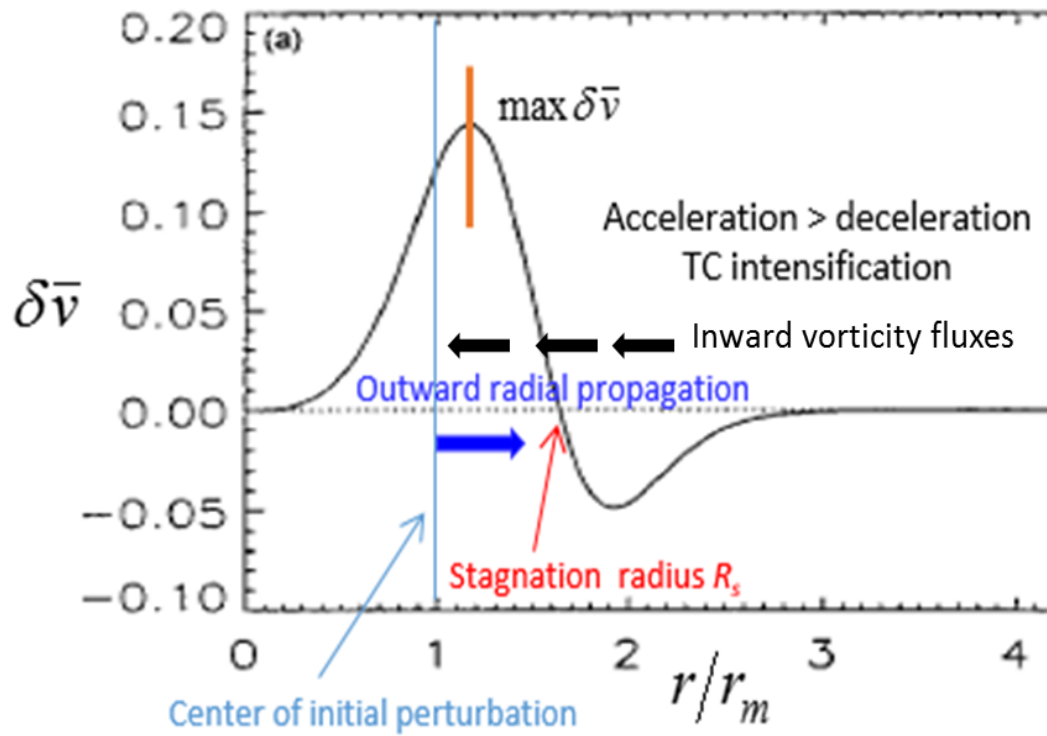


Fig. 1.3: Change in tangential velocity due to the wave activities as function of non-dimensional radius where  $r_m$  is the radius of maximum wind.

## CHAPTER 2: VRW Theory in Pseudo-Height Coordinates

### 2.1 Asymmetric Balance Model

The quasi-geostrophic (QG) theory is arguably the most influential theory in meteorology. The basic-state of the QG flow is in geostrophic and hydrostatic balance. The meteorologically insignificant motions associated with high-frequency gravity and inertial waves are filtered out. In the absence of external heating and friction, the QG flow conserves its potential vorticity (PV) on fluid particles following the geostrophic wind. In other words, the horizontal advection by the geostrophic wind and the vertical advection are neglected in the horizontal momentum equation. The physical simplicity of the QG theory has led to the fundamental understanding of the dynamics of large-scale atmospheric flow. Meteorologists were bent on obtaining a deeper understanding of three-dimensional (3D) asymmetric dynamics of tropical cyclones (TCs), but for a long time had to cope with the complexity of the primitive equations till late 80s and early 90s. Observations indicated that the symmetric TCs evolve near equilibrium states of hydrostatic and gradient wind balance (Willoughby 1990), suggesting that the evolution of a rapidly rotating TC vortex could be described and understood in a much simpler dynamic framework.

In light of the QG theory, Shapiro and Montgomery (1993, SM93) developed a so-called asymmetric balance (AB) model, which describes the TC-like vortices in a way that may be analogous to the description of the large-scale atmospheric flow by the QG theory. The AB theory views a 3D asymmetric TC as a rapidly rotating vortex but with a slow macroscopic evolution. The basic-state of such a vortex satisfies the gradient-wind and hydrostatic balance and holds thermal-wind relation. It allows for order one divergence as

well as rapid rotation, but filters out high-frequency gravity and inertial waves (“fast motions”) from the system. The horizontal advection of a scalar quantity follows a fluid particle in a symmetric vortex in which only the azimuthal-mean tangential velocity is considered and the azimuthal-mean radial flow is neglected.

However, the assumptions that lead to the AB approximation are different from those of QG approximation. The AB theory was developed following the so-called geostrophic momentum (GM) approximation of the large-scale atmospheric flow (Eliassen 1949; Fjortoft 1962; Hoskins 1975) in which the expansion of a term in the momentum equation is truncated after the first-order time derivative under the assumption of  $D^2(\cdot)/Dt^2 \ll f^2(\cdot)$ , where  $D/Dt$  is the material derivative and  $f$  is the Coriolis parameter. The GM approximation is similar to the QG approximation when it is transformed to the geostrophic coordinate. The AB theory extends the GM approximation of the large-scale atmospheric flow to the rapidly rotating vortices by replacing  $f^2$  (the square inertial frequency in a resting atmosphere) with the inertial stability of a symmetric vortex,  $S^2 = \bar{\eta} \bar{\xi}$  (the analog of  $f^2$  in a rapidly rotating environment) where  $\bar{\eta} = f + \frac{1}{r} \frac{\partial(r\bar{v})}{\partial r}$  is the absolute vorticity,  $\bar{\xi} = f + 2\bar{v}/r$  is the inertia parameter,  $r$  is the radius in a cylindrical coordinate with its origin located at the center of a vortex, and  $\bar{v}$  is the azimuthal-mean tangential velocity. Thus, the basic assumption of AB theory becomes,

$$D_v^2(\cdot)/Dt^2 \ll S^2(\cdot), \quad (2.1)$$

where  $\frac{D_v}{Dt} = \frac{\partial}{\partial t} + \frac{\bar{v}}{r} \frac{\partial}{\partial \lambda} = \frac{\partial}{\partial t} + \bar{\Omega} \frac{\partial}{\partial \lambda}$ ,  $\lambda$  is the azimuthal angle of a cylindrical coordinate, and  $\bar{\Omega}$  is the angular velocity.

## 2.2 Governing Equations

The hydrostatic balance, gradient wind balance, and thermal wind relation in a pseudo-height cylindrical coordinate (Hoskins and Bertherton 1972) can be expressed as,

$$\frac{\partial \bar{\phi}}{\partial z} = (g / \theta_0) \bar{\theta}, \quad (2.2)$$

$$\frac{\partial \bar{\phi}}{\partial r} = \bar{v}^2 / r + f \bar{v}, \quad (2.3)$$

$$\frac{\partial^2 \bar{\phi}}{\partial r \partial z} = (g / \theta_0) \frac{\partial \bar{\theta}}{\partial r} = \bar{\xi} \bar{v}_z, \quad (2.4)$$

where  $r$  and  $z$  are the radius and pseudo-height of a cylindrical coordinate following a translating symmetric vortex with the coordinate origin located at the vortex center,  $\phi$  is the geopotential,  $g$  is the gravitational acceleration,  $\theta$  is the potential temperature, and  $\theta_0$  is a reference potential temperature,  $\bar{v}_z = \frac{\partial \bar{v}}{\partial z}$  is the vertical shear of azimuthal-mean tangential velocity. Overbar represents the azimuthal-mean. For weak disturbances, the radial and tangential momentum, thermodynamic, and continuity equations without external heating and friction on an  $f$  plane may be written as (SM93),

$$\frac{D_v u'}{Dt} - \bar{\xi} v' = -\frac{\partial \phi'}{\partial r}, \quad (2.5)$$

$$\frac{D_v v'}{Dt} + \eta u' + \frac{\partial \bar{v}}{\partial z} w' = -\frac{1}{r} \frac{\partial \phi'}{\partial \lambda}, \quad (2.6)$$

$$\frac{D_v}{Dt} \left( \frac{\partial \phi'}{\partial z} \right) + \bar{\xi} \frac{\partial \bar{v}}{\partial z} u' + N^2 w' = 0, \quad (2.7)$$

$$\frac{1}{r} \frac{\partial (r u')}{\partial r} + \frac{1}{r} \frac{\partial v'}{\partial \lambda} + \frac{\partial w'}{\partial z} = 0, \quad (2.8)$$

where  $u$  is the radial wind,  $w$  is the vertical velocity,  $N^2 = \frac{\partial^2 \bar{\phi}}{\partial z^2} = (g/\theta_0) \frac{\partial \bar{\theta}}{\partial z}$  is the azimuthal-mean buoyancy frequency, and prime indicates the deviation from the azimuthal-mean. Taking the linear material derivative ( $D_v / Dt$ ) of momentum equations and cross-substituting  $u'$  and  $v'$  yields,

$$\frac{D_v^2 u'}{Dt} + \bar{\eta} \bar{\xi} u' + \bar{\xi} \frac{\partial \bar{v}}{\partial z} w' + \frac{D_v}{Dt} \left( \frac{\partial \phi'}{\partial r} \right) = -\bar{\xi} \frac{1}{r} \frac{\partial \phi'}{\partial \lambda}. \quad (2.9)$$

$$\frac{D_v^2 v'}{Dt} + \bar{\eta} \bar{\xi} v' + \frac{\partial \bar{v}}{\partial z} \frac{D_v w'}{Dt} + \frac{1}{r} \frac{D_v}{Dt} \left( \frac{\partial \phi'}{\partial \lambda} \right) = \bar{\eta} \frac{\partial \phi'}{\partial r}. \quad (2.10)$$

Under the fundamental assumption of AB model,  $D_v^2(\cdot) / Dt^2 \ll S^2(\cdot)$ , the secondary material derivatives in Eqs. 2.9-2.10 can be neglected. Then, it is easy to show from Eqs. 2.6-2.8 that the geopotential perturbation tendency equation can be written as (cf. SM93's Eq.3.10),

$$\begin{aligned} & \frac{D}{Dt} \left[ \frac{1}{r^2} \frac{\partial^2 \phi'}{\partial \lambda^2} + \frac{\bar{\xi} \bar{q}}{N^2} \frac{1}{r} \frac{\partial}{\partial r} \left( \frac{r N^2}{\bar{\xi} \bar{q}} \frac{\partial \phi'}{\partial r} \right) + \frac{\bar{\xi} \bar{q}}{N^2} \frac{\partial}{\partial z} \left( \frac{\bar{\eta}}{\bar{q}} \frac{\partial \phi'}{\partial z} \right) - \frac{\bar{\xi} \bar{q}}{N^2} \frac{1}{r} \frac{\partial}{\partial r} \left( \frac{r}{\bar{q}} \bar{v}_z \frac{\partial \phi'}{\partial z} \right) - \frac{\bar{\xi} \bar{q}}{N^2} \frac{1}{r} \frac{\partial}{\partial z} \left( \frac{r}{\bar{q}} \bar{v}_z \frac{\partial \phi'}{\partial r} \right) \right], \\ & = -\frac{\bar{\xi} \bar{q}}{N^2} \left[ \frac{\partial}{\partial r} \left( \frac{N^2}{\bar{q}} \right) - \frac{\partial}{\partial z} \left( \frac{\bar{\xi} \bar{v}_z}{\bar{q}} \right) \right] \frac{1}{r} \frac{\partial \phi'}{\partial \lambda}, \end{aligned} \quad (2.11)$$

where  $\bar{q} = \bar{\eta} N^2 - \bar{\xi} \bar{v}_z^2$  is the azimuthal-mean PV. The terms on the right-hand side (RHS) of Eq.2.11 may be simplified as

$$\begin{aligned}
& -\frac{\bar{\xi}\bar{q}}{N^2} \left[ \frac{\partial}{\partial r} \left( \frac{N^2}{\bar{q}} \right) - \frac{\partial}{\partial z} \left( \frac{\bar{\xi}\bar{v}_z}{\bar{q}} \right) \right] \frac{1}{r} \frac{\partial \phi'}{\partial \lambda} \\
& = -\frac{\bar{\xi}\bar{q}}{N^2} \left[ -\frac{N^2}{\bar{q}^2} \frac{\partial \bar{q}}{\partial r} + \frac{\bar{\xi}\bar{v}_z}{\bar{q}^2} \frac{\partial \bar{q}}{\partial z} + \frac{1}{\bar{q}} \frac{\partial N^2}{\partial r} - \frac{1}{\bar{q}} \frac{\partial}{\partial z} (\bar{\xi}\bar{v}_z) \right] \frac{1}{r} \frac{\partial \phi'}{\partial \lambda}, \\
& = -\frac{\bar{\xi}\bar{q}}{N^2} \left( -\frac{N^2}{\bar{q}^2} \frac{\partial \bar{q}}{\partial r} + \frac{\bar{\xi}\bar{v}_z}{\bar{q}^2} \frac{\partial \bar{q}}{\partial z} + \frac{1}{\bar{q}} \frac{\partial^3 \bar{\phi}}{\partial z \partial z \partial r} - \frac{1}{\bar{q}} \frac{\partial^3 \bar{\phi}}{\partial z \partial z \partial r} \right) \frac{1}{r} \frac{\partial \phi'}{\partial \lambda} \\
& = \frac{\bar{\xi}}{\bar{q}r} \left( \frac{\partial \bar{q}}{\partial r} - \frac{\bar{\xi}\bar{v}_z}{N^2} \frac{\partial \bar{q}}{\partial z} \right) \frac{\partial \phi'}{\partial \lambda}
\end{aligned} \tag{2.12}$$

where to obtain Eq.2.12, derivatives of Eqs.2.2 & 2.4 and definition of  $N^2$  have been used.

The terms in the square bracket on the left-hand side (LHS) of Eq.2.11 may be rewritten

as,

$$\begin{aligned}
& \frac{1}{r^2} \frac{\partial^2 \phi'}{\partial \lambda^2} + \frac{\bar{\xi}\bar{q}}{N^2} \frac{1}{r} \frac{\partial}{\partial r} \left( \frac{rN^2}{\bar{\xi}\bar{q}} \frac{\partial \phi'}{\partial r} \right) + \frac{\bar{\xi}\bar{q}}{N^2} \frac{\partial}{\partial z} \left( \frac{\bar{\eta}}{\bar{q}} \frac{\partial \phi'}{\partial z} \right) - \frac{\bar{\xi}\bar{q}}{N^2} \frac{1}{r} \frac{\partial}{\partial r} \left( \frac{r}{\bar{q}} \bar{v}_z \frac{\partial \phi'}{\partial z} \right) - \frac{\bar{\xi}\bar{q}}{N^2} \frac{1}{r} \frac{\partial}{\partial z} \left( \frac{r}{\bar{q}} \bar{v}_z \frac{\partial \phi'}{\partial r} \right) \\
& = \frac{1}{r^2} \frac{\partial^2 \phi'}{\partial \lambda^2} + \frac{\partial^2 \phi'}{\partial r^2} + \frac{\bar{\xi}\bar{\eta}}{N^2} \frac{\partial^2 \phi'}{\partial z^2} - \frac{2\bar{\xi}\bar{v}_z}{N^2} \frac{\partial^2 \phi'}{\partial r \partial z} + \left( \frac{1}{r} + \frac{1}{N^2} \frac{\partial N^2}{\partial r} - \frac{1}{\bar{\xi}} \frac{\partial \bar{\xi}}{\partial r} - \frac{1}{\bar{q}} \frac{\partial \bar{q}}{\partial r} \right) \frac{\partial \phi'}{\partial r} \\
& \quad + \frac{\bar{\xi}\bar{\eta}}{N^2} \left( \frac{1}{\bar{\eta}} \frac{\partial \bar{\eta}}{\partial z} - \frac{1}{\bar{q}} \frac{\partial \bar{q}}{\partial z} \right) \frac{\partial \phi'}{\partial z} - \frac{\bar{\xi}\bar{v}_z}{N^2} \left( \frac{1}{r} + \frac{1}{\bar{v}_z} \frac{\partial \bar{v}_z}{\partial r} - \frac{1}{\bar{q}} \frac{\partial \bar{q}}{\partial r} \right) \frac{\partial \phi'}{\partial z}, \\
& \quad - \frac{\bar{\xi}\bar{v}_z}{N^2} \left( \frac{1}{r} + \frac{1}{\bar{v}_z} \frac{\partial \bar{v}_z}{\partial z} - \frac{1}{\bar{q}} \frac{\partial \bar{q}}{\partial r} \right) \frac{\partial \phi'}{\partial r} \\
& \approx \frac{1}{r^2} \frac{\partial^2 \phi'}{\partial \lambda^2} + \frac{\partial^2 \phi'}{\partial r^2} + \frac{\bar{\xi}\bar{\eta}}{N^2} \frac{\partial^2 \phi'}{\partial z^2} - \frac{2\bar{\xi}\bar{v}_z}{N^2} \frac{\partial^2 \phi'}{\partial r \partial z}
\end{aligned} \tag{2.13}$$

where the first derivative terms of  $\frac{\partial \phi'}{\partial r}$  and  $\frac{\partial \phi'}{\partial z}$  that contain  $\frac{1}{r}$ ,  $\frac{1}{\bar{q}} \frac{\partial \bar{q}}{\partial r}$ ,  $\frac{1}{\bar{q}} \frac{\partial \bar{q}}{\partial z}$ ,  $\frac{1}{\bar{\xi}} \frac{\partial \bar{\xi}}{\partial r}$ ,

$\frac{1}{N^2} \frac{\partial N^2}{\partial z}$ ,  $\frac{1}{\bar{\eta}} \frac{\partial \bar{\eta}}{\partial z}$ ,  $\frac{1}{\bar{v}_z} \frac{\partial \bar{v}_z}{\partial r}$ , and  $\frac{1}{\bar{v}_z} \frac{\partial \bar{v}_z}{\partial z}$  have been neglected since they have much

smaller magnitudes than the remaining second derivative terms of Eq.,  $\frac{\partial^2 \phi'}{\partial \lambda^2}$ ,  $\frac{\partial^2 \phi'}{\partial r \partial z}$ , and

$\frac{\partial^2 \phi'}{\partial z^2}$  under the assumption of slow radial variation of the mean flow. Thus, the simplified geopotential tendency equation without diabatic heating in pseudo-height coordinates can be written as,

$$\left(\frac{\partial}{\partial t} + \bar{\Omega} \frac{\partial}{\partial \lambda}\right) \left[ \frac{1}{r^2} \frac{\partial^2 \phi'}{\partial \lambda^2} + \frac{\partial^2 \phi'}{\partial r^2} + \frac{\bar{\xi} \bar{\eta}}{N^2} \frac{\partial^2 \phi'}{\partial z^2} - \frac{2 \bar{\xi} \bar{v}_z}{N^2} \frac{\partial^2 \phi'}{\partial r \partial z} \right] = \frac{\bar{\xi}}{\bar{q} r} \left[ \frac{\partial \bar{q}}{\partial r} - \frac{\bar{\xi} \bar{v}_z}{N^2} \frac{\partial \bar{q}}{\partial z} \right] \frac{\partial \phi'}{\partial \lambda}. \quad (2.14)$$

### 2.3 WKB Analysis

The geopotential tendency equation Eq. (2.14) may be linearized in the vicinity of  $r=R_0$  and  $z=Z_0$  as,

$$\begin{aligned} & \left( \frac{\partial}{\partial t} + \left[ \bar{\Omega}_0 + \left( \frac{\partial \bar{\Omega}}{\partial r} \right)_0 \delta r + \left( \frac{\partial \bar{\Omega}}{\partial z} \right)_0 \delta z \right] \frac{\partial}{\partial \lambda} \right) \left[ \frac{1}{R_0^2} \frac{\partial^2 \phi'}{\partial \lambda^2} + \frac{\partial^2 \phi'}{\partial r^2} + \frac{\bar{\xi}_0 \bar{\eta}_0}{N_0^2} \frac{\partial^2 \phi'}{\partial z^2} - \frac{2 \bar{\xi}_0 \bar{v}_{z0}}{N_0^2} \frac{\partial^2 \phi'}{\partial r \partial z} \right], \\ & = \frac{\bar{\xi}_0}{R_0 \bar{q}_0} \left[ \left( \frac{\partial \bar{q}}{\partial r} \right)_0 - \frac{\bar{\xi}_0 \bar{v}_{z0}}{N_0^2} \left( \frac{\partial \bar{q}}{\partial z} \right)_0 \right] \frac{\partial \phi'}{\partial \lambda}, \end{aligned} \quad (2.15)$$

where  $\delta r = r - R_0$  and  $\delta z = z - Z_0$ . Subscript 0 denotes the value at the initial position of an asymmetry, i.e.,  $r = R_0$  and  $z = Z_0$ .

Following MK97's Wenzel-Kramers-Brillouin (WKB) analyses, we seek solutions of Eq.2.15 in the form of,

$$\phi'(r, \lambda, z, t) = A(t) e^{i\{n\lambda + k(t)(r-R_0) + m(t)(z-Z_0) - \Lambda(t)\}} \quad (2.16)$$

where  $A(t)$  is a time-dependent amplitude,  $n$ ,  $k(t)$  and  $m(t)$  are the azimuthal, radial, and vertical wavenumbers, and  $\Lambda(t)$  a time-dependent phase. Substituting Eq.2.16 into Eq.15 and grouping real and imaginary terms together yields an equation in the form of

$\{R_e\} + i\{I_m\} = 0$ . MK97 showed that equating the imaginary part and real part to zero (i.e.,  $I_m = 0, R_e = 0$ ) gives the information of wave dispersion relation and wave amplitude, respectively. Since this dissertation focuses on vortex Rossby wave (VRW propagation), issues on wave amplitude (i.e., results obtained from  $R_e = 0$ ) will not be discussed. The balance that  $I_m = 0$  yields,

$$B(n\bar{\Omega}_0 - \frac{\partial\Lambda}{\partial t}) + \frac{n\bar{\xi}_0}{R_0\bar{q}_0} \left[ (\frac{\partial\bar{q}}{\partial r})_0 - \frac{\bar{\xi}_0\bar{v}_{z0}}{N_0^2} (\frac{\partial\bar{q}}{\partial z})_0 \right] + B \left[ \left( \frac{\partial k}{\partial t} + n(\frac{\partial\bar{\Omega}}{\partial r})_0 \right) \delta r + \frac{\partial m}{\partial t} + n(\frac{\partial\bar{\Omega}}{\partial z})_0 \delta z \right] = 0, \quad (2.17)$$

where

$$B = \frac{n^2}{R_0^2} + k^2 + \frac{\bar{\xi}_0\bar{\eta}_0}{N_0^2} m^2 - \frac{2\bar{\xi}_0\bar{v}_{z0}}{N_0^2} km = \frac{n^2}{R_0^2} + (k - \frac{\bar{\xi}_0\bar{v}_{z0}}{N_0^2} m)^2 + \frac{\bar{\xi}_0\bar{q}_0}{N_0^4} m^2. \quad (2.18)$$

It is clear that  $B$  is always positive for any radial and vertical wavenumbers,  $k$  and  $m$ . Since Eq.2.17 is valid for small but otherwise arbitrary  $\delta r$  and  $\delta z$ , one may first set  $\delta r = 0$  and  $\delta z = 0$ . Eq. 2.17, then, gives the dispersion relation of a spectrally localized wave-packet,

$$\omega = \frac{\partial\Lambda}{\partial t} = n\bar{\Omega}_0 + \frac{n}{R_0} \frac{\bar{q}_f}{B}. \quad (2.19)$$

E.2.19 is similar to that of Rossby waves in a sheared flow (Tung 1983; Vallis 2006), where

$$\bar{q}_f = \frac{\bar{\xi}_0}{\bar{q}_0} \left( (\frac{\partial\bar{q}}{\partial r})_0 - \frac{\bar{\xi}_0\bar{v}_{z0}}{N_0^2} (\frac{\partial\bar{q}}{\partial z})_0 \right). \quad (2.20)$$

For nonzero  $\delta r$  and  $\delta z$ , Eq.2.17 then requires,

$$\frac{\partial k}{\partial t} = -n(\frac{\partial\bar{\Omega}}{\partial r})_0; \quad k(t) = k_0 - n(\frac{\partial\bar{\Omega}}{\partial r})_0 t, \quad (2.21)$$

$$\frac{\partial m}{\partial t} = -n\left(\frac{\partial \bar{\Omega}}{\partial z}\right)_0; \quad m(t) = m_0 - n\left(\frac{\partial \bar{\Omega}}{\partial z}\right)_0 t, \quad (2.22)$$

where  $k_0$  and  $m_0$  are the initial radial and vertical wavenumber. Since both  $\left(\frac{\partial \bar{\Omega}}{\partial r}\right)_0$  and  $\left(\frac{\partial \bar{\Omega}}{\partial z}\right)_0$  are negative provided that  $\bar{v}$  decreases with the increase of radius and height, Equations 2.21-2.22 indicate that radial wavenumber and vertical wavenumber,  $k$  and  $m$ , continue increasing as the wave-packet propagates upward and radially outward.

For barotropic conditions ( $\bar{v}_z = 0$ ), it is easy to show that Eq.2.19 and Eq. 2.22 reduce to,

$$\omega = n\bar{\Omega}_0 + \frac{n}{R_0} \frac{\bar{\xi}_0}{\bar{q}_0} \frac{\left(\frac{\partial \bar{q}}{\partial r}\right)_0}{\frac{n^2}{R_0^2} + k^2 + \frac{\bar{\eta}_0 \bar{\xi}_0}{N^2} m^2}. \quad (2.23)$$

$$\frac{\partial m}{\partial t} = 0. \quad (2.24)$$

Equation 2.23 is the same as that derived by MM00 [cf. Eq.3.3 in MM00]. For 2D non-divergent barotropic model ( $\bar{v}_z = 0$  and  $\bar{\eta}_0 \approx \bar{\xi}_0$ ), Eq.2.19 reduces to,

$$\omega = n\bar{\Omega}_0 + \frac{n}{R_0} \frac{\left(\frac{\partial \bar{\eta}}{\partial r}\right)_0}{\frac{n^2}{R_0^2} + k^2}. \quad (2.25)$$

Equation 2.25 is the same as that derived by MK97.

Comparing Eq. 2.22 with Eq. 2.24, an immediate conclusion is that VRWs keep their vertical wavenumbers constant during propagating in barotropic vortices whereas the vertical wavenumbers continue increasing as wave-packets propagate upward in baroclinic

vortices, a feature similar to the radially propagating VRW that increases its radial wavenumber as wave-packets propagate radially outward. This is a key difference of VRW propagation in barotropic and baroclinic conditions. From the perspective of shearing effect, such a difference is easy to understand. Similar to the radial gradient of mean angular velocity, which causes the increase of radial wavenumber, the vertical shearing effect because of the vertical gradient of mean angular velocity leads to the increase of vertical wavenumber as wave-packets propagate upward. Another important difference of VRW propagation in barotropic and baroclinic vortices results from their vortex " $\beta$ " effect. In baroclinic conditions, the vortex " $\beta$ " effect,  $\bar{q}_f$ , includes an extra term associated with the vertical gradient of basic-state PV. We will show in Chapter 4 that this extra vortex " $\beta$ " effect has a profound impact on VWR vertical and radial propagation.

From Eq.2.19, the radial group velocity  $C_{gr} = \partial\omega/\partial k$  and vertical group velocity  $C_{gz} = \partial\omega/\partial m$  in baroclinic conditions can be readily derived,

$$C_{gr} = -\frac{2n}{R_0} \left( k - \frac{\bar{\xi}_0 \bar{v}_{z0}}{N_0^2} m \right) \frac{\bar{q}_f}{B^2}, \quad (2.26)$$

$$C_{gz} = -\frac{2n}{R_0} \left( \frac{\bar{\xi}_0 \bar{\eta}_0}{N_0^2} m - \frac{\bar{\xi}_0 \bar{v}_{z0}}{N_0^2} k \right) \frac{\bar{q}_f}{B^2}. \quad (2.27)$$

For barotropic conditions (constant  $m$  and  $\bar{v}_z = 0$ ), Eqs.2.26-2.27 reduce to,

$$C_{gr} = -\frac{2nk \bar{\xi}_0}{R_0 \bar{q}_0} \frac{\left( \frac{\partial \bar{q}}{\partial r} \right)_0}{\left( \frac{n^2}{R_0^2} + k^2 + \frac{\bar{\eta}_0 \bar{\xi}_0}{N^2} m^2 \right)^2} \quad (2.28)$$

$$C_{gz} = -\frac{2nm}{R_0} \frac{\bar{\eta}_0 \bar{\xi}_0^2}{N^2 \bar{q}_0} \frac{(\frac{\partial \bar{q}}{\partial r})_0}{(\frac{n^2}{R_0^2} + k^2 + \frac{\bar{\eta}_0 \bar{\xi}_0}{N^2} m^2)^2} \quad (2.29)$$

Equations 2.28-2.29 are the same as those obtained by MM00, showing that the increase of radial wavenumber  $k$  as a result of the radial shearing effect not only causes the radially propagating VRWs to slow down and stop at the stagnation radius but also reduces the vertical group velocity so that vertically propagating VRW eventually stops at a stagnation height for a sufficiently large radial wavenumber  $k$ . For baroclinic basic-state vortices (Eqs. 2.26-2.27), in addition to the radial shearing effect, both the increase of vertical wavenumber  $m$  and the vortex " $\beta$ " associated with the vertical gradient of basic-state vorticity and tangential velocity can complicate the radial and vertical propagation of wave-packets.

Integrating group velocities (Eqs. 2.26-2.27) with time, one obtains the radial and vertical trajectories of an isolated wave-packet,

$$r(t) = R_0 + \int_0^t C_{gr} dt = R_0 + \int_0^t \left[ -\frac{2n}{R_0} \left( k - \frac{\bar{\xi}_0 \bar{v}_{z0}}{N_0^2} m \right) \frac{\bar{q}_f}{B^2} \right] dt \quad (2.30)$$

$$z(t) = Z_0 + \int_0^t C_{gz} dt = R_0 + \int_0^t \left[ -\frac{2n}{R_0} \left( \frac{\bar{\xi}_0 \bar{\eta}_0}{N_0^2} m - \frac{\bar{\xi}_0 \bar{v}_{z0}}{N_0^2} k \right) \frac{\bar{q}_f}{B^2} \right] dt. \quad (2.31)$$

The stagnation radius ( $R_{stg}$ ) and stagnation height ( $Z_{stg}$ ) for monopole vortices, then, can be determined by calculating the limit of trajectories as time  $t \rightarrow \infty$ ,

$$R_{stg} = R_0 + \frac{\delta_2 \bar{q}_f \bar{\Omega}_{z0} m_0}{R_0 \bar{\Omega}_{r0}^2 A^3} \left( 1 - \frac{\bar{\Omega}_{z0} k_0}{\bar{\Omega}_{r0} m_0} \right) \left( \tan^{-1} \gamma - \frac{\pi}{2} \right) + \left( \frac{\bar{q}_f}{R_0 \bar{\Omega}_{r0}^2 A^2} \right) \frac{\delta_2 m_0 (\bar{\Omega}_{r0} m_0 - \bar{\Omega}_{z0} k_0) + (\bar{\Omega}_{r0} + \delta_1 \bar{\Omega}_{z0}) n^2 / R_0^2}{n^2 / R_0^2 + (k_0 + \delta_1 m_0)^2 + \delta_2 m_0^2} \quad (2.32)$$

$$\begin{aligned}
Z_{stg} = & Z_0 + \frac{\delta_2 \bar{q}_f m_0}{R_0 \bar{\Omega}_{r0} A^3} \left(1 - \frac{\bar{\Omega}_{z0} k_0}{\bar{\Omega}_{r0} m_0}\right) \left(\frac{\pi}{2} - \tan^{-1} \gamma\right) \\
& - \left(\frac{\bar{q}_f}{R_0 \bar{\Omega}_{r0}^2 A^2}\right) \frac{\delta_2 k_0 (\bar{\Omega}_{r0} m_0 - \bar{\Omega}_{z0} k_0) - [\delta_1 (\bar{\Omega}_{r0} + \delta_1 \bar{\Omega}_{z0}) + \delta_2 \bar{\Omega}_{z0}] n^2 / R_0^2}{n^2 / R_0^2 + (k_0 + \delta_1 m_0)^2 + \delta_2 m_0^2},
\end{aligned} \tag{2.33}$$

where,

$$\bar{\Omega}_{r0} = \left(\frac{\partial \bar{\Omega}}{\partial r}\right)_0,$$

$$\bar{\Omega}_{z0} = \left(\frac{\partial \bar{\Omega}}{\partial z}\right)_0,$$

$$\delta_1 = -\frac{\bar{\xi}_0 \bar{v}_{z0}}{N_0^2},$$

$$\delta_2 = \frac{\bar{\xi}_0 \bar{q}_0}{N_0^4},$$

$$A^2 = \left[ \left(1 + \frac{\delta_1 \bar{\Omega}_{z0}}{\bar{\Omega}_{r0}}\right)^2 + \frac{\delta_2 (\bar{\Omega}_{z0})^2}{(\bar{\Omega}_{r0})^2} \right] \frac{n^2}{R_0^2} + \delta_2 \left(m_0 - \frac{\bar{\Omega}_{z0}}{\bar{\Omega}_{r0}} k_0\right)^2, \text{ and}$$

$$\gamma = \frac{(k_0 + \delta_1 m_0) \left(1 + \frac{\delta_1 \bar{\Omega}_{z0}}{\bar{\Omega}_{r0}}\right) + \delta_2 m_0 \frac{\bar{\Omega}_{z0}}{\bar{\Omega}_{r0}}}{A}.$$

For barotropic conditions ( $\bar{\Omega}_{z0} = 0$  and  $\delta_1 = 0$ ), Eqs. 2.31-2.33 reduce to,

$$R_{stg} = R_0 + \frac{\bar{\xi}_0}{R_0 \bar{q}_0 \bar{\Omega}_{r0}} \frac{\left(\frac{\partial \bar{q}}{\partial r}\right)_0}{\frac{n^2}{R_0^2} + k_0^2 + \delta_2 m_0^2}, \tag{2.34}$$

$$Z_{stg} = Z_0 + \frac{m_0 \bar{\eta}_0 \bar{\xi}_0^2 \left(\frac{\partial \bar{q}}{\partial r}\right)_0}{R_0 N^2 \bar{q}_0 \bar{\Omega}_{r0} A^3} \left[ \frac{\pi}{2} - \tan^{-1} \left(\frac{k_0}{A}\right) - \frac{k_0 A}{k_0^2 + A^2} \right], \tag{2.35}$$

where

$$A^2 = \frac{n^2}{R_0^2} + \frac{\bar{\eta}_0 \bar{\xi}_0}{N^2} m_0^2.$$

Equations 2.34-2.35 are the same as those obtained by MM00 [c.f. Eq. 3.5 in MM00]. Comparing the wave formulae obtained in the barotropic and baroclinic conditions, it is clear that the baroclinicity substantially complicates the radial and vertical propagation of VRWs. The detailed impact of baroclinicity on VRW propagation will be discussed in Chapter 4.

## 2.4 Summary

Although the VRW concept was formed nearly 50 years ago by MacDonald (1968), all theoretical studies on VRW to date have been limited to 2D non-divergent barotropic and 3D barotropic vortices lack of vertical structure (e.g. MK97, Moller and Montgomery 1999; S99; MM00, MW03, Cotto et al. 2015; Gonzalez et al. 2015). Real TC vortices, however, are in fact baroclinic. As more and more evidences of VRW are shown in observations and 3D full physics numerical simulations (e.g., Kossin and Eastin 2001; Mallen et al. 2005; Wang 2001, 2002a,b; Chen and Yau 2001; Chen and Yau 2003; Kossin et al. 2002, 2004; Kossin and Schubert 2004; Chavanne et al. 2010), the VRW theory obtained in barotropic vortices may not provide appropriate guidance for observational and numerical studies of VRW since barotropic assumption may oversimplify the wave features. To my knowledge, this is the first theoretical study to examine the effects of baroclinicity on VRW kinematics in TC-like vortices. Using AB model and WKB analysis, I successfully derived the generalized wave formulae that can describe VRW propagation in both barotropic and baroclinic conditions. The results show that baroclinicity substantially

complicates the VRW propagation due to both the vertical shearing effect that results in the increase of vertical wavenumber with time and the additional " $\beta$ " restoring mechanism that supports wave propagation.

## CHAPTER 3: VRW Theory in Isentropic Coordinates

### 3.1 Introduction

Using the WKB analysis, the generalized wave dispersion relation, group velocities, and stagnation radius and height of VRWs are successfully derived in the pseudo-height coordinate. However, the derived wave formulae are much more complicated than those obtained in barotropic conditions. The complication results from the 3D structure of a baroclinic vortex in the pseudo-height coordinate in contrast to the virtually 2D structure of a barotropic vortex. If the basic state of a baroclinic vortex is stably stratified so that the potential temperature,  $\theta$ , is a monotonically increasing function of height, then,  $\theta$  may be used as an independent vertical coordinate. The advantage is that the vertical “velocity” in this coordinate is just  $\dot{\theta} = \frac{D\theta}{Dt}$ . Adiabatic motions ( $\dot{\theta} = 0$ ) are virtually 2D when viewed in an isentropic coordinate framework. Thus, the atmospheric flow the baroclinic (Ertel) PV equation is often derived in isentropic coordinates. Since the wave restoring mechanism of VRW is the radial and vertical gradient of PV, it is interesting to see if the wave formulae can be simplified in isentropic coordinates. Such a derivation may shed new light on and help gain a deeper understanding of VRW propagation in barotropic and baroclinic conditions.

### 3.2 Transformation between Pseudo-Height and Isentropic Coordinates

Let  $\psi$  be A generic scalar, which can be expressed as  $\psi = \psi(r, z)$  and  $\psi = \psi(r, \theta)$  in pseudo-height coordinates and isentropic coordinates, respectively. It is also true  $z = z(r, \theta)$ , then, the linear material derivatives may be written as,

$$\begin{aligned}
d\psi &= \frac{\partial\psi}{\partial r} dr + \frac{\partial\psi}{\partial z} dz \\
d\psi &= \frac{\partial^*\psi}{\partial r} dr + \frac{\partial^*\psi}{\partial\theta} d\theta, \\
dz &= \frac{\partial^*z}{\partial r} dr + \frac{\partial^*z}{\partial\theta} d\theta
\end{aligned} \tag{3.1}$$

where  $\frac{\partial}{\partial}$  and  $\frac{\partial^*}{\partial}$  indicate the partial derivative in pseudo-height coordinates and

isentropic coordinates, respectively. From Eq.3.1, it is easy to show,

$$\begin{aligned}
\frac{\partial\psi}{\partial r} + \frac{\partial^*z}{\partial r} \frac{\partial\psi}{\partial z} &= \frac{\partial^*\psi}{\partial r} \\
\frac{\partial^*z}{\partial\theta} \frac{\partial\psi}{\partial z} &= \frac{\partial^*\psi}{\partial\theta}
\end{aligned} \tag{3.2}$$

When  $\psi=\theta$  is satisfied, Eqs. 2.2-2.4 lead to,

$$\begin{aligned}
\frac{\partial^*z}{\partial r} &= -\frac{\partial\theta}{\partial r} \left( \frac{\partial\theta}{\partial z} \right)^{-1} = -\frac{\bar{\xi}\bar{v}_z}{N^2} \\
\frac{\partial^*z}{\partial\theta} &= \left( \frac{\partial\theta}{\partial z} \right)^{-1},
\end{aligned} \tag{3.3}$$

where to obtain Eq.3.3, relations  $\frac{\partial\theta}{\partial z} = \frac{N^2}{(g/\theta_0)}$  (from Eq.2.2) and  $\frac{\partial\theta}{\partial r} = \frac{\bar{\xi}\bar{v}_z}{(g/\theta_0)}$  (from

Eqs.2.3 & 2.4) have been used. Thus, the transformation of first derivatives between pseudo-height coordinates and isentropic coordinates (Montgomery and Shapiro 1995) can be obtained as follows,

$$\begin{aligned}
\frac{\partial^*}{\partial r} &= \frac{\partial}{\partial r} - \frac{\bar{\xi}\bar{v}_z}{N^2} \frac{\partial}{\partial z} \\
\frac{\partial^*}{\partial\theta} &= \frac{g/\theta_0}{N^2} \frac{\partial}{\partial z}
\end{aligned} \tag{3.4}$$

and

$$\begin{aligned}\frac{\partial}{\partial r} &= \frac{\partial^*}{\partial r} + \frac{\bar{\xi}\bar{v}_z}{g/\theta_0} \frac{\partial^*}{\partial \theta} \\ \frac{\partial}{\partial z} &= \frac{N^2}{g/\theta_0} \frac{\partial^*}{\partial \theta}\end{aligned}\quad (3.5)$$

With Eqs.3.4-3.5, it is known that the transformation of second derivatives between the coordinates can be written as,

$$\begin{aligned}\frac{\partial^2}{\partial r^2} &= \left(\frac{\partial^*}{\partial r} + \frac{\bar{\xi}\bar{v}_z}{g/\theta_0} \frac{\partial^*}{\partial \theta}\right)\left(\frac{\partial^*}{\partial r} + \frac{\bar{\xi}\bar{v}_z}{g/\theta_0} \frac{\partial^*}{\partial \theta}\right) \\ &= \frac{\partial^{*2}}{\partial r^2} + 2\frac{\bar{\xi}\bar{v}_z}{g/\theta_0} \frac{\partial^{*2}}{\partial r\partial\theta} + \left(\frac{\bar{\xi}\bar{v}_z}{g/\theta_0}\right)^2 \frac{\partial^{*2}}{\partial \theta^2} + \frac{\partial}{\partial r}\left(\frac{\bar{\xi}\bar{v}_z}{g/\theta_0}\right) \frac{\partial^*}{\partial \theta}\end{aligned}\quad (3.6)$$

$$\begin{aligned}\frac{\partial^2}{\partial r\partial z} &= \left(\frac{\partial^*}{\partial r} + \frac{\bar{\xi}\bar{v}_z}{g/\theta_0} \frac{\partial^*}{\partial \theta}\right)\left(\frac{N^2}{g/\theta_0} \frac{\partial^* f}{\partial \theta}\right) \\ &= \frac{N^2}{g/\theta_0} \frac{\partial^{*2}}{\partial r\partial\theta} + \frac{\bar{\xi}\bar{v}_z N^2}{(g/\theta_0)^2} \frac{\partial^{*2}}{\partial \theta^2} + \frac{\partial}{\partial r}\left(\frac{N^2}{g/\theta_0}\right) \frac{\partial^*}{\partial \theta}\end{aligned}\quad (3.7)$$

$$\begin{aligned}\frac{\partial^2}{\partial z^2} &= \frac{N^2}{g/\theta_0} \frac{\partial^*}{\partial \theta} \left(\frac{N^2}{g/\theta_0} \frac{\partial^*}{\partial \theta}\right) \\ &= \left(\frac{N^2}{g/\theta_0}\right)^2 \frac{\partial^{*2}}{\partial \theta^2} + \frac{\partial}{\partial z}\left(\frac{N^2}{g/\theta_0}\right) \frac{\partial^*}{\partial \theta}\end{aligned}\quad (3.8)$$

### 3.3 Geopotential Perturbation Tendency Equation in Isentropic Coordinates

Applying the transformation of first derivatives (Eqs. 3.4-3.5) and second derivatives (Eqs.3.6-3.8) to the terms on the RHS and LHS of Eq.2.14, respectively, it can be shown that the geopotential tendency equation can be written as,

$$\begin{aligned}\frac{D}{Dt} \left[ \frac{1}{r^2} \frac{\partial^{*2}\phi'}{\partial \lambda^2} + \frac{\partial^{*2}\phi'}{\partial r^2} + \frac{\bar{\xi}\bar{q}}{(g/\theta_0)^2} \frac{\partial^{*2}\phi'}{\partial \theta^2} + \frac{\bar{\xi}\bar{v}_z}{g/\theta_0} \left( \frac{1}{\bar{v}_z} \frac{\partial \bar{v}_z}{\partial r} + \frac{1}{\bar{\xi}} \frac{\partial \bar{\xi}}{\partial r} + \frac{\bar{\eta}}{\bar{v}_z} \frac{1}{N^2} \frac{\partial N^2}{\partial z} - \frac{2}{N^2} \frac{\partial N^2}{\partial r} \right) \frac{\partial^{*2}\phi'}{\partial \theta} \right] \\ = \frac{\bar{\xi}}{\bar{q}r} \frac{\partial^{*2}\bar{q}}{\partial \theta} \frac{\partial^{*2}\phi'}{\partial \lambda}\end{aligned}$$

(3.9)

The last term on the LHS of Eq.3.9,

$$\frac{\bar{\xi} \bar{v}_z}{g / \theta_0} \left( \frac{1}{\bar{v}_z} \frac{\partial \bar{v}_z}{\partial r} + \frac{1}{\bar{\xi}} \frac{\partial \bar{\xi}}{\partial r} + \frac{\bar{\eta}}{\bar{v}_z} \frac{1}{N^2} \frac{\partial N^2}{\partial z} - \frac{2}{N^2} \frac{\partial N^2}{\partial r} \right) \frac{\partial^* \phi'}{\partial \theta},$$

can be neglected

for two reasons. First, the terms  $\frac{1}{\bar{v}_z} \frac{\partial \bar{v}_z}{\partial r}$ ,  $\frac{1}{\bar{\xi}} \frac{\partial \bar{\xi}}{\partial r}$ ,  $\frac{1}{N^2} \frac{\partial N^2}{\partial z}$ , and  $\frac{1}{N^2} \frac{\partial N^2}{\partial r}$  are small under

the assumption of slow radial variation of the mean flow. Second,  $\frac{\partial^* \phi'}{\partial \theta}$  measures the

vertical gradient associated with eddy disturbances, whereas the second-order derivatives,

$$\frac{\partial^{*2} \phi'}{\partial \lambda^2}, \frac{\partial^{*2} \phi'}{\partial r^2}, \text{ and } \frac{\partial^{*2} \phi'}{\partial \theta^2},$$

measure the curvature of eddy disturbances. The former has a

much smaller magnitude than the latter. Thus, for the purpose of applying the local WKB approximation, the geopotential perturbation tendency equation in isentropic coordinates can be simplified to,

$$\frac{D}{Dt} \left[ \frac{1}{r^2} \frac{\partial^{*2} \phi'}{\partial \lambda^2} + \frac{\partial^{*2} \phi'}{\partial r^2} + \frac{\bar{\xi} \bar{q}}{(g / \theta_0)^2} \frac{\partial^{*2} \phi'}{\partial \theta^2} \right] = \frac{\bar{\xi}}{\bar{q} r} \frac{\partial^* \bar{q}}{\partial \theta} \frac{\partial^* \phi'}{\partial \lambda}. \quad (3.10)$$

### 3.4 WKB Analyses

Eq.3.10 can be linearized in the vicinity of  $r = R_0^*$  and  $\theta = \theta_0$  as

$$\left( \frac{\partial^*}{\partial t} + \left[ \bar{\Omega}_0 + \left( \frac{\partial^* \bar{\Omega}}{\partial r} \right)_0 \delta r + \left( \frac{\partial^* \bar{\Omega}}{\partial \theta} \right)_0 \delta \theta \right] \frac{\partial^*}{\partial \lambda} \right) \left[ \frac{1}{R_0^2} \frac{\partial^2 \phi'}{\partial \lambda^2} + \frac{\partial^2 \phi'}{\partial r^2} + \frac{\bar{\xi}_0 \bar{q}_0}{(g/\theta_0)^2} \frac{\partial^2 \phi'}{\partial \theta^2} \right] \quad (3.11)$$

$$= \frac{\bar{\xi}_0}{\bar{q}_0 R_0} \left( \frac{\partial^* \bar{q}}{\partial \theta} \right)_0 \frac{\partial^* \phi'}{\partial \lambda}$$

In the local WKB approximation, one seeks solutions to Eq.3.11 in the form of,

$$\phi'(r, \lambda, \theta, t) = A_\theta(t) e^{i\{n\lambda + k^*(t)(r-R_0^*) + m^*(t)(\theta-\Theta_0) - \Lambda(t)\}}, \quad (3.12)$$

where  $n$ ,  $k^*$ , and  $m^*$  denote the azimuthal, radial, and vertical wavenumber in isentropic coordinates, respectively. The variable  $A(t)$  is a time-dependent amplitude and  $\Lambda(t)$  is a time-dependent phase. Inserting Eq. 3.12 into Eq. 3.11, equating the imaginary part to zero, and using the same method as that used in pseudo-height coordinates, one can obtain the dispersion relation and group velocities of VRW packets in isentropic coordinates,

$$\omega = n\bar{\Omega}_0 + \frac{n}{R_0^*} \frac{\bar{\xi}_0}{\bar{q}_0} \frac{\left( \frac{\partial^* \bar{q}}{\partial \theta} \right)_0}{\frac{n^2}{R_0^2} + k^{*2} + \frac{\bar{\xi}_0 \bar{q}_0}{(g/\theta_0)^2} m^{*2}}. \quad (3.13)$$

$$\frac{\partial k^*}{\partial t} = -n \left( \frac{\partial^* \bar{\Omega}}{\partial r} \right)_0; \quad k^*(t) = k_0^* - n \left( \frac{\partial^* \bar{\Omega}}{\partial r} \right)_0 t. \quad (3.14)$$

$$\frac{\partial m^*}{\partial t} = -n \left( \frac{\partial^* \bar{\Omega}}{\partial \theta} \right)_0; \quad m^*(t) = m_0^* - n \left( \frac{\partial^* \bar{\Omega}}{\partial \theta} \right)_0 t. \quad (3.15)$$

$$C_{gr} = - \frac{2nk^*}{R_0^*} \frac{\bar{\xi}_0}{\bar{q}_0} \frac{\left( \frac{\partial^* \bar{q}}{\partial \theta} \right)_0}{\left( \frac{n^2}{R_0^{*2}} + k^{*2} + \frac{\bar{\xi}_0 \bar{q}_0}{(g/\theta_0)^2} m^{*2} \right)^2}. \quad (3.16)$$

$$C_{g\theta} = -\frac{2nm^*}{R_0^*} \frac{\bar{\xi}_0^2}{(g/\theta_0)^2} \frac{(\frac{\partial^* \bar{q}}{\partial \theta})_0}{\left( \frac{n^2}{R_0^{*2}} + k^{*2} + \frac{\bar{\xi}_0 \bar{q}_0}{(g/\theta_0)^2} m^{*2} \right)^2}. \quad (3.17)$$

For a better comparison with the results in pseudo-height coordinates, we define,

$$B^* = \frac{n^2}{R_0^2} + k^{*2} + \frac{\bar{\xi}_0 \bar{q}_0}{(g/\theta_0)^2} m^{*2}, \quad (3.18)$$

$$\bar{q}_f^* = \frac{\bar{\xi}_0}{\bar{q}_0} \left( \frac{\partial^* \bar{q}}{\partial \theta} \right)_0. \quad (3.19)$$

Comparing Eqs.3.13, 3.16, and 3.17 with Eqs. 2.23, 2.28, and 2.29, it is clear that the VRW dispersion relation and group velocities in baroclinic vortices in isentropic coordinates have the same formalism as those of barotropic vortices in pseudo-height coordinates except that the Rossby deformation radius in barotropic conditions  $\frac{\bar{\xi}_0 \bar{\eta}_0}{N^2}$  is replaced by  $\frac{\bar{\xi}_0 \bar{q}_0}{(g/\theta_0)^2}$  in baroclinic conditions. A key difference is in the vertical wavenumber, which is constant in barotropic conditions but increases with time in baroclinic condition regardless of coordinates. Despite the same format of group velocities, the increase of vertical wavenumber with time in baroclinic vortices results in a more complex expression for the stagnation radius and stagnation level. Integrating group velocities (Eqs. 3.16-3.17) with time, the radial and vertical trajectories of an isolated wave-packet can be obtained. Similar to what was done in pseudo-height coordinates, the stagnation radius and stagnation level for monopole vortices in the isentropic coordinates can be derived by calculating the limit of trajectories as time  $t \rightarrow \infty$ ,

$$R_{stg}^* = R_0^* + \frac{\bar{\xi}_0 \delta_2^* \bar{q}_{r0}^* \bar{\Omega}_{\theta 0}^* m_0^*}{R_0^* \bar{q}_0^* \bar{\Omega}_{r0}^{*2} A^3} \left(1 - \frac{\bar{\Omega}_{\theta 0}^* k_0^*}{\bar{\Omega}_{r0}^* m_0^*}\right) (\tan^{-1} \gamma - \frac{\pi}{2})$$

$$- \left(\frac{\bar{\xi}_0 \bar{q}_{r0}^*}{R_0^* \bar{q}_0^* \bar{\Omega}_{r0}^{*2} A^2}\right) \frac{\bar{\Omega}_{\theta 0}^* \delta_2^* k_0^* m_0^* - \bar{\Omega}_{r0}^* (n^2 / R_0^{*2} + \delta_2^* m_0^{*2})}{n^2 / R_0^{*2} + k_0^{*2} + \delta_2^* m_0^{*2}}, \quad (3.20)$$

$$\Theta_{stg}^* = \Theta_0^* + \frac{\bar{\xi}_0 \delta_2^* \bar{q}_{r0}^* m_0^*}{R_0^* \bar{q}_0^* \bar{\Omega}_{r0}^* A^3} \left(1 - \frac{\bar{\Omega}_{\theta 0}^* k_0^*}{\bar{\Omega}_{r0}^* m_0^*}\right) \left(\frac{\pi}{2} - \tan^{-1} \gamma\right)$$

$$- \left(\frac{\bar{\xi}_0 \bar{q}_{r0}^*}{R_0^* \bar{q}_0^* \bar{\Omega}_{r0}^{*2} A^2}\right) \frac{\bar{\Omega}_{r0}^* \delta_2^* k_0^* m_0^* - \bar{\Omega}_{\theta 0}^* \delta_2^* (n^2 / R_0^{*2} + k_0^{*2})}{n^2 / R_0^{*2} + k_0^{*2} + \delta_2^* m_0^{*2}}, \quad (3.21)$$

where

$$\bar{q}_{r0}^* = \left(\frac{\partial^* \bar{q}}{\partial r}\right)_0,$$

$$\bar{\Omega}_{\theta 0}^* = \left(\frac{\partial^* \bar{\Omega}}{\partial \theta}\right)_0,$$

$$\bar{\Omega}_{r0}^* = \left(\frac{\partial^* \bar{\Omega}}{\partial r}\right)_0,$$

$$\delta_2^* = \frac{\bar{\xi}_0 \bar{q}_0}{(g / \theta_0)^2},$$

$$A^2 = \left(1 + \frac{\delta_2^* \bar{\Omega}_{\theta 0}^{*2}}{\bar{\Omega}_{r0}^{*2}}\right) \frac{n^2}{R_0^{*2}} + \delta_2^* \left(m_0^* - \frac{\bar{\Omega}_{\theta 0}^*}{\bar{\Omega}_{r0}^*} k_0^*\right)^2, \text{ and}$$

$$\gamma = \frac{k_0^* + \delta_2^* \frac{\bar{\Omega}_{\theta 0}^*}{\bar{\Omega}_{r0}^*} m_0^*}{A}.$$

As indicated by Eqs. 3.13-3.21, although the wave dispersion and group velocities has the same format as those in barotropic conditions in pseudo-height coordinates, the wave

stagnation radius and stagnation level share the similar format to those in baroclinic conditions in pseudo-height coordinates. The reason is based on the fact that the vertical wavenumber increases with time as wave-packets propagate radially outward and upward regardless of coordinates. For barotropic conditions,  $\bar{\Omega}_{\theta 0}^* = \left(\frac{\partial^* \bar{\Omega}}{\partial \theta}\right)_0 = 0$ , Eqs. 3.20-3.21

reduce to,

$$R_{stg}^* = R_0^* + \frac{\bar{\xi}_0}{R_0^* \bar{q}_0 \bar{\Omega}_{r0}^*} \frac{\bar{q}_{r0}^*}{\frac{n^2}{R_0^{*2}} + k_0^{*2} + \delta_2^* m_0^{*2}}, \quad (3.22)$$

$$\Theta_{stg}^* = \Theta_0^* + \frac{m_0^* \bar{\eta}_0 \bar{\xi}_0^2 \bar{q}_{r0}^*}{R_0^* N^2 \bar{q}_0 \bar{\Omega}_{r0}^* \Lambda^3} \left[ \frac{\pi}{2} - \tan^{-1} \left( \frac{k_0^*}{\Lambda} \right) - \frac{k_0^* \Lambda}{k_0^{*2} + \Lambda^2} \right], \quad (3.23)$$

where

$$\Lambda^2 = \frac{n^2}{R_0^{*2}} + \frac{\bar{\eta}_0 \bar{\xi}_0}{N^2} m_0^{*2}.$$

Eqs. 3.22-3.23 have the exact format as those of Eqs. 2.34-2.35 in barotropic conditions in pseudo-height coordinates.

### 3.5 ‘Critical’ Surface of Radial and Vertical Propagation of VRWs

As we showed previously, the wave dispersion relation obtained in the AB model framework can be reduced back to that in MK97’s 2D nondivergent model (Eq. 2.25). Under the same assumption of  $\bar{\eta}_0 \approx \bar{\xi}_0$ , the stagnation radius in barotropic conditions (Eq. 2.34) can be reduced back to that obtained by MK97, i.e.,

$$R_{stg} = R_0 + \frac{1}{R_0 \bar{\Omega}_{r0}} \frac{(\frac{\partial \bar{\eta}}{\partial r})_0}{\frac{n^2}{R_0^2} + k_0^2}. \quad (3.24)$$

Eq. 3.24 may be rewritten as,

$$\bar{\Omega}_{r0} \delta r_s = \frac{\bar{q}_f}{R_0 B_0}, \quad (3.25)$$

where  $\delta r_s = R_{stg} - R_0$ ,  $\bar{q}_f = (\frac{\partial \bar{\eta}}{\partial r})_0$ , and  $B_0 = \frac{n^2}{R_0^2} + k_0^2$ . Comparing Eq. 3.25 with the

dispersion relation in the 2D non-divergent model (Eq. 2.25), it seems to suggest the stagnation radius in the simplest 2D problem happens to equal the ‘critical’ radius determined by the initial wave-packet and the basic-state of the initial vortex. The feature of stagnation radius in 2D framework raises a question: Is this also true for the maximum propagation of VRWs in 3D baroclinic vortices? If so, it would suggest that the radial propagation and vertical propagation of VRWs are not independent but are closely related.

To answer this question, we examined the values of  $\bar{\Omega}_{r0}^* \delta r_s^*$  and  $\bar{\Omega}_{\theta 0}^* \delta \Theta_s^*$ . Tedious algebraic manipulation yields,

$$\begin{aligned} \bar{\Omega}_{r0}^* \delta r_s^* &= \bar{\Omega}_{r0}^* (R_{stg}^* - R_0^*) \\ &= \frac{\bar{\xi}_0 \delta_2^* \bar{q}_{r0}^* \bar{\Omega}_{\theta 0}^* m_0^*}{R_0^* \bar{q}_0^* \bar{\Omega}_{r0}^* A^3} \left(1 - \frac{\bar{\Omega}_{\theta 0}^* k_0^*}{\bar{\Omega}_{r0}^* m_0^*}\right) \left(\tan^{-1} \gamma - \frac{\pi}{2}\right), \\ &\quad - \left(\frac{\bar{\xi}_0 \bar{q}_{r0}^*}{R_0^* \bar{q}_0^* \bar{\Omega}_{r0}^* A^2}\right) \frac{\bar{\Omega}_{\theta 0}^* \delta_2^* k_0^* m_0^* - \bar{\Omega}_{r0}^* (n^2 / R_0^{*2} + \delta_2^* m_0^{*2})}{n^2 / R_0^{*2} + k_0^{*2} + \delta_2^* m_0^{*2}} \end{aligned} \quad (3.26)$$

$$\begin{aligned}
\bar{\Omega}_{\theta 0}^* \delta \Theta_s^* &= \bar{\Omega}_{\theta 0}^* (\Theta_{stg}^* - \Theta_0^*) \\
&= \frac{\bar{\xi}_0 \delta_2^* \bar{q}_{r0} \bar{\Omega}_{\theta 0}^* m_0^*}{R_0^* \bar{q}_0 \bar{\Omega}_{r0}^* A^3} \left(1 - \frac{\bar{\Omega}_{\theta 0}^* k_0^*}{\bar{\Omega}_{r0}^* m_0^*}\right) \left(\frac{\pi}{2} - \tan^{-1} \gamma\right), \\
&\quad - \left(\frac{\bar{\xi}_0 \bar{q}_{r0}}{R_0^* \bar{q}_0 \bar{\Omega}_{r0}^* A^2}\right) \frac{\bar{\Omega}_{\theta 0}^* \bar{\Omega}_{r0}^* \delta_2^* k_0^* m_0^* - \bar{\Omega}_{\theta 0}^{*2} \delta_2^* \left(\frac{n^2}{R_0^{*2}} + k_0^{*2}\right)}{n^2 / R_0^{*2} + k_0^{*2} + \delta_2^* m_0^{*2}}
\end{aligned} \tag{3.27}$$

$$\begin{aligned}
\bar{\Omega}_{r0}^* \delta r_s^* + \bar{\Omega}_{\theta 0}^* \delta \Theta_s^* &= \left(\frac{\bar{\xi}_0 \bar{q}_{r0}}{R_0^* \bar{q}_0 \bar{\Omega}_{r0}^* A^2}\right) \frac{-2\delta_2^* \bar{\Omega}_{r0}^* \bar{\Omega}_{\theta 0}^* k_0^* m_0^* + \bar{\Omega}_{r0}^{*2} \left(\frac{n^2}{R_0^{*2}} + \delta_2^* m_0^{*2}\right) + \delta_2^* \bar{\Omega}_{\theta 0}^{*2} \left(\frac{n^2}{R_0^{*2}} + k_0^{*2}\right)}{\frac{n^2}{R_0^{*2}} + k_0^{*2} + \delta_2^* m_0^{*2}} \\
&= \left(\frac{\bar{\xi}_0 \bar{q}_{r0}}{R_0^* \bar{q}_0 \bar{\Omega}_{r0}^* A^2}\right) \frac{\bar{\Omega}_{r0}^{*2} + \delta_2^* \bar{\Omega}_{\theta 0}^{*2} \frac{n^2}{R_0^{*2}} + \delta_2^* (\bar{\Omega}_{r0}^* m_0^* - \bar{\Omega}_{\theta 0}^* k_0^*)^2}{\frac{n^2}{R_0^{*2}} + k_0^{*2} + \delta_2^* m_0^{*2}}, \\
&= \frac{\bar{\xi}_0 \bar{q}_{r0}}{R_0^* \bar{q}_0 B_0^*} \\
&= \frac{\bar{q}_f^*}{R_0^* B_0^*}
\end{aligned} \tag{3.28}$$

where  $B_0^* = \frac{n^2}{R_0^2} + k_0^{*2} + \frac{\bar{\xi}_0 \bar{q}_0}{(g/\theta_0)^2} m_0^{*2}$ .

Remarkably, Eq.3.28 has the similar format to Eq.3.25. Then, does this expression also holds in the pseudo-height coordinates? The similar algebraic manipulation is made with Eqs. 2.32-2.33,

$$\begin{aligned}
\bar{\Omega}_{r0} \delta r_s &= \bar{\Omega}_{r0} (R_{stg} - R_0) \\
&= \frac{\delta_2 \bar{q}_f \bar{\Omega}_{z0} m_0}{R_0 \bar{\Omega}_{r0} A^3} \left(1 - \frac{\bar{\Omega}_{z0} k_0}{\bar{\Omega}_{r0} m_0}\right) \left(\tan^{-1} \gamma - \frac{\pi}{2}\right), \quad (3.29) \\
&+ \left(\frac{\bar{q}_f}{R_0 \bar{\Omega}_{r0}^2 A^2}\right) \frac{\delta_2 m_0 \bar{\Omega}_{r0} (\bar{\Omega}_{r0} m_0 - \bar{\Omega}_{z0} k_0) + (\bar{\Omega}_{r0}^2 + \delta_1 \bar{\Omega}_{r0} \bar{\Omega}_{z0}) \frac{n^2}{R_0^2}}{n^2 / R_0^2 + (k_0 + \delta_1 m_0)^2 + \delta_2 m_0^2}
\end{aligned}$$

$$\begin{aligned}
\bar{\Omega}_{z0} \delta z_s &= \bar{\Omega}_{z0} (Z_{stg} - Z_0) \\
&= \frac{\delta_2 \bar{q}_f \bar{\Omega}_{z0} m_0}{R_0 \bar{\Omega}_{r0} A^3} \left(1 - \frac{\bar{\Omega}_{z0} k_0}{\bar{\Omega}_{r0} m_0}\right) \left(\frac{\pi}{2} - \tan^{-1} \gamma\right), \\
&- \left(\frac{\bar{q}_f}{R_0 \bar{\Omega}_{r0}^2 A^2}\right) \frac{\delta_2 k_0 \bar{\Omega}_{z0} (\bar{\Omega}_{r0} m_0 - \bar{\Omega}_{z0} k_0) - [\delta_1 \bar{\Omega}_{r0} \bar{\Omega}_{z0} + \delta_1^2 \bar{\Omega}_{z0}^2 + \delta_2 \bar{\Omega}_{z0}^2] \frac{n^2}{R_0^2}}{n^2 / R_0^2 + (k_0 + \delta_1 m_0)^2 + \delta_2 m_0^2}
\end{aligned} \quad (3.30)$$

$$\begin{aligned}
\bar{\Omega}_{r0} \delta r_s + \bar{\Omega}_{z0} \delta z_s &= \left(\frac{\bar{q}_f}{R_0 \bar{\Omega}_{r0}^2 A^2}\right) \frac{[(\bar{\Omega}_{r0} + \delta_1 \bar{\Omega}_{z0})^2 + \delta_2 \bar{\Omega}_{z0}^2] \frac{n^2}{R_0^2} + \delta_2 (\bar{\Omega}_{r0} m_0 - \bar{\Omega}_{z0} k_0)^2}{\frac{n^2}{R_0^2} + (k_0 + \delta_1 m_0)^2 + \delta_2 m_0^2}, \\
&= \frac{\bar{q}_f}{R_0 B_0}
\end{aligned} \quad (3.31)$$

$$\text{where } B_0 = \frac{n^2}{R_0^2} + \left(k_0 - \frac{\bar{\xi}_0 \bar{v}_{z0}}{N_0^2} m_0\right)^2 + \frac{\bar{\xi}_0 \bar{q}_0}{N_0^4} m_0^2.$$

Equations 3.28 and 3.31 indicate that the stagnation radius and stagnation level fall on a ‘critical’ surface determined by the radial and vertical gradient of basic-state angular velocity and properties of initial wave-packet regardless of coordinates. In other words, the maximum radial and vertical distance traveled by VRW wave-packets is constrained by the

geometry of the ‘critical’ surface determined by the properties of initial wave-packets and basic-state vortices. Thus, an enhanced wave vertical propagation must be accompanied by suppression of wave radial propagation and vice versa.

### **3.6 Summary**

The wave dispersion relation and group velocities of VRWs in baroclinic vortices in the isentropic coordinate are found to have the same format as those in barotropic vortices in the pseudo-height coordinate. The difference is the representation of the Rossby deformation radius. This result is not a surprise considering that adiabatic vortex flow is virtually 2D when viewed in isentropic coordinates, which, to some extent, may be analogues to barotropic vortices in pseudo-height coordinates. However, the increase of vertical wavenumber with time in baroclinic conditions largely complicates the wave propagation feature as VRW wave-packets propagate radially outward and upward. It is found that the maximum radial and vertical distance traveled by VRW wave-packets is constrained by the geometry of the ‘critical’ surface determined by the properties of initial wave-packets and basic-state vortices. Thus, an enhanced wave vertical propagation must be accompanied by suppression of wave radial propagation and vice versa. This finding may have important implication on wave-mean-flow interaction and the associated mechanism for storm intensification, which will be addressed in Chapter 6.

## CHAPTER 4: Impact of Baroclinicity on VRW Propagation

### 4.1 Introduction

The generalized wave dispersion relation, group velocities, and stagnation radius and heights in both pseudo-height and isentropic coordinates and their implication on VRW propagation in barotropic and baroclinic vortices have been presented and discussed in Chapter 2 and 3. However, since the derived wave formulae are highly nonlinear involving with time-varying radial and vertical wavenumbers and depending on basic-state properties of vortices, a deeper understanding of the impact of baroclinicity on VRW propagation requires further investigation. In this chapter, the derived wave formulae will be applied to specific TC-like vortices to explore how baroclinicity affects the radial and vertical propagation of VRWs.

### 4.2 Initial Condition of TC-like Vortices

To appropriately compare with the results of MK97 and MM00 in barotropic conditions, the same basic-state swirl radial profile used in MK97 and MM00 is used in this study, which can be represented as,

$$\bar{v}_s(r) = v_m \frac{2(r/r_m)}{1+(r/r_m)^2} = \frac{2v_m r_m r}{r_m^2 + r^2}, \quad (4.1)$$

where subscript “s” denotes the value at the surface. The variable  $v_m$  is the maximum tangential velocity of a vortex and  $r_m$  is the radius of maximum wind (RMW). Following MK97 and MM00, vortices with both hurricane-strength (CAT-1) with  $v_m=36.8 \text{ ms}^{-1}$  and  $r_m=70 \text{ km}$  and tropical-storm-strength with  $v_m=14.7 \text{ ms}^{-1}$  and  $r_m=145 \text{ km}$  are investigated

in this study. The tangential velocity and relative vorticity radial profiles of these two vortices are shown in Fig. 4.1

For a better illustration, our investigation will be carried out in the pseudo-height coordinate. To construct baroclinic vortices, the surface tangential velocity profile is, then, extended in the vertical using the formula proposed by Nolan et al. (2007),

$$\bar{v}(r, z) = \bar{v}_s(r) \exp\left(-\frac{|z - z_0|^\alpha}{\alpha L^\alpha}\right), \quad (4.2)$$

where  $L$  indicates the depth of the barotropic part of a vortex,  $\alpha$  is the decay rate away from the barotropic zone, and  $z_0$  is the altitude of the maximum tangential velocity, which in our case is at the surface (i.e.,  $z_0=0$ ). Following Nolan et al. (2007), we take  $\alpha=2$ . By specifying different  $L$ , 3D vortices with different baroclinicities can be constructed. Here, I take  $L=7500$  m and  $L=5000$  m, which represent weak and strong baroclinicity, respectively. The vertical gradient of tangential velocity of these two vortices is plotted in Fig. 4.2.

For simplicity,  $N^2$  is set to a constant ( $N^2=1.2e^{-4}s^{-1}$ ). For a constructed 3D baroclinic vortex, once the main characteristics of an initial asymmetry, such as azimuthal wavenumber, initial radial and vertical wavenumbers, and initial asymmetry location ( $R_0$  and  $Z_0$ ), are specified, all other basic-state parameters, such as  $\bar{\Omega}_{r0}$ ,  $\bar{\Omega}_{z0}$ ,  $\bar{\xi}_0$ ,  $\bar{\eta}_0$ ,  $\bar{v}_{z0}$ ,  $B$ , and  $\bar{q}_f$ , needed to determine the wave trajectories and stagnation radius and height can be calculated.

### 4.3 Simplest Baroclinicity: Constant Vertical Shear of Tangential Velocity

Since the 3D baroclinic vortices constructed in this study have complicated vertical structures with varying vertical gradient of basic-state tangential velocity, to simplify the problem and highlight the impact of baroclinicity on VRW propagation, it is helpful to first consider the simplest baroclinic case with a constant vertical gradient of tangential velocity. In the first experiment, the radial and vertical propagation in the 2D nondivergent vortex, 3D barotropic vortex, and 3D baroclinic vortex with the hurricane-strength (i.e.,  $v_m=36.8 \text{ ms}^{-1}$  and  $r_m=70 \text{ km}$ ) is investigated. The mean vertical gradient of tangential velocity is set to  $\bar{v}_{z0}=-0.0032 \text{ s}^{-1}$ , which is the value averaged over the entire depth of the strong baroclinic vortex ( $L=5000$ ) at  $R_0 = r_m$ . The initial asymmetry is placed at  $R_0 = 100 \text{ km}$  and  $Z_0 = 0 \text{ m}$ . The initial radial wavenumber  $k_0$  and vertical wavenumber  $m_0$  are set to  $\frac{1}{100} \text{ km}^{-1}$  and  $\frac{1}{10} \text{ km}^{-1}$ , respectively.

The choice of wavenumbers and location of initial asymmetry is the same as MK97's analyses. Montgomery and Kallenbach considered a non-dimensional basic-state swirl profile in their study,  $\hat{v}(\hat{r}) = \frac{2\hat{r}}{1+\hat{r}^2}$ , where variables with over-hat  $\hat{\cdot}$  indicate their non-dimensional values. This expression of tangential velocity radial profile is equivalent to Eq. (4.1). The WKB analysis requires the tightly wound limit,  $\hat{k}\hat{R} \gg 1$ , to be satisfied. In MK97's WKB analysis, the radius where initial asymmetry is placed,  $\hat{R}_0$ , and initial radial wavenumber,  $\hat{k}_0$ , were taken as  $\hat{R}_0 = 1$  and  $\hat{k}_0 = 1$  so that  $\hat{k}_0\hat{R}_0 = 1$ . Strictly speaking, this does not meet the WKB's tightly wound limit. However, as I showed in

Chapters 2 and 3, the radial wavenumber increases with time as the wave-packet propagates radially outward. This causes the WKB tightly wound limit,  $\hat{k}\hat{R} \gg 1$ , to be valid as time goes on. The dimensional radius and radial wavenumber may be expressed as,  $R = \hat{R}/r_m$  and  $k = \hat{k}/r_m$ . Taking  $r_m = 100 \text{ km}$  and following MK97 to set  $\hat{R}_0 = 1$  and  $\hat{k}_0 = 1$ , then,  $R_0$  and  $k_0$  will be  $R_0 = 100 \text{ km}$  and  $k_0^{-1} = 100 \text{ km}$ , respectively. Using Eqs.2.21-2.22, it is easy to calculate the time evolution of radial wavenumber for the hurricane-strength monopole vortex constructed in this study. Figure 4.3 shows the time variation of radial wavenumber  $k$  and vertical wavenumber  $m$  with initial wavenumbers set to  $k_0^{-1}=100 \text{ km}$  and  $m_0^{-1}=10 \text{ km}$ . For an azimuthal wavenumber-2 asymmetry, at the 1<sup>st</sup> h and 5.5<sup>th</sup> h,  $k$  increases to  $6.4\text{e-}5 \text{ m}^{-1}$  and  $3.1\text{e-}4 \text{ m}^{-1}$ , and  $m$  increases to  $4.3\text{e-}4 \text{ m}^{-1}$  and  $1.9\text{e-}3 \text{ m}^{-1}$ , respectively. The corresponding radial and vertical wavelengths are:  $1/k=15.6 \text{ km}$  and  $3.2 \text{ km}$ ;  $1/m=2.3 \text{ km}$  and  $0.5 \text{ km}$ , respectively. Apparently, the WKB approximation becomes more and more valid as time goes on. Thus, the initial period may be considered as a spin-up period for WKB analysis. This gives me the confidence that the initial condition used in this experiment is appropriate to study the propagation of VRWs.

Figures 4.4 and 4.5 show the time evolution of group velocities and trajectories of azimuthal wavenumber-1, wavenumber-2, and wavenumber-3 wave-packets for the hurricane-strength vortex in which the initial radial wavenumber  $k_0$  and vertical wavenumber  $m_0$  are set to  $\frac{1}{100} \text{ km}^{-1}$  and  $\frac{1}{10} \text{ km}^{-1}$  respectively and the initial asymmetry is placed at  $R_0=100 \text{ km}$ ,  $Z_0=0 \text{ km}$ . As a comparison, the stagnation radii and heights computed by Eqs. 2.32-2.33 are also plotted in Fig. 4.5. Note that for an appropriate comparison, the

vortex " $\beta$ " effect in the 2D nondivergent vortex has been adjusted to the value equivalent to that in the 3D barotropic hurricane-strength vortex. Several interesting features are shown in Figs. 4.4 and 4.5, which are worthy to be emphasized as follows.

First, with the same " $\beta$ " effect, VRWs have a larger radial group velocity and can propagate a far radial distance in a 2D vortex than in a 3D vortex. Since VRWs can also propagate upward in a 3D vortex, which suggests that the vertical propagation of VRWs has an important bearing on their radial propagation consistent with the theoretical analysis presented in Chapters 2 and 3.

Second, low azimuthal wavenumber perturbations can propagate farther in radial and vertical directions than high azimuthal wavenumber perturbations. Vortex Rossby wave radial and vertical propagation reduces substantially as the increase of wavenumber. The maximum radial propagation distance (or stagnation radius) and vertical distance (or stagnation height) of wavenumber-1 asymmetry are more than double and nearly triple respectively of the distances of a wavenumber-2 asymmetry. Vortex Rossby wave with wavenumbers greater than 3 can barely propagate radially outward and upward. This result is consistent with that of MM00 and other studies.

Third, the vertical propagation of VRW is permitted in barotropic vortices despite the fact that the basic-state vortices lack the vertical change in tangential velocity. How VRWs can vertically propagate in barotropic vortices is an interesting question. It may be understood in light of the vertical propagation of planetary Rossby waves (PRW) in a continuously stratified fluid schematically illustrated by Fig. 4.6. In a stratified fluid with a rigid lid at the bottom and top boundaries in the northern Hemisphere, a southward motion at the low level requires high pressure on its right facing down-wind direction (i.e., on the

west of the motion) according to the geostrophic balance. Similarly, a northward motion at the low level induces high pressure on the east and low pressure on the west. Since the vertical displacements are restricted at the top and bottom of the stratified fluid, the mid-level fluid must respond with large vertical displacements in order to generate the pressure changes at the low level. The mid-level density surface must upwell right over the low-level high pressure to generate cold anomaly. Likewise, mid-level warm anomaly must develop over the low-level low pressure. In a continuously stratified fluid, such maximum anomaly at the mid-level must be resulted from the upward wave propagation since each layer is internally connected. In the meantime, on the  $\beta$  plane the variation of Coriolis parameter causes meridional flow to be convergent or divergent. A southward decrease of  $f$  will cause the increase of wind speed assuming a uniform pressure gradient, and thus, a divergence. Similarly, a northward increase of  $f$  will cause a convergence at the low level. The resulting convergence-divergence pattern calls for transverse velocities both in zonal and vertical, each partially relieving the convergence-divergence of the meridional flow. This determines the main characteristics of PRW propagation in a stratified fluid. The picture depicted above may be extended to a monopole vortex. A radially outward and inward motion may be analogous to the southward and northward motion, respectively. For the same reason, a stratified barotropic vortex (in our case the stratification is determined by  $N^2$ ) should support the vertical propagation of VRWs.

Baroclinicity significantly promotes the vertical propagation of VRWs (Figs. 4.5d-4.5f). As I showed in Chapters 2 and 3, the vertical gradient of angular velocity,  $\overline{\Omega}_{z0}$ , in baroclinic vortices causes the increase of vertical wavenumber as wave packets propagate upward, an effect that should limit the vertical propagation of VRWs by itself. Apparently,

this effect is overwhelmed by the vertical gradient of PV. Like the radial gradient of PV that supports the radial propagation of VRWs, the vertical gradient of PV should promote the vertical propagation of VRWs.

It is also shown in Fig. 4.5 that baroclinicity suppresses VRW radial propagation. This result is consistent with the theoretical derivation presented in Chapter 3 that radially propagating VRWs are strongly constrained by the vertically propagating waves via a ‘critical’ surface. Thus, the enhanced vertical propagation of VRWs by baroclinicity should be accompanied with the suppression of wave radial propagation. However, our results seem to be in conflict with what was found by Peng et al. (2014a and 2104b) who showed that the baroclinicity promotes the radial propagation of VRWs in a two-layered model. The cause for this difference is likely a consequence of the fact that the vertical propagation of VRWs is not supported in their two-layered model.

To better understand the characteristics of VRW propagation in barotropic and baroclinic vortices and their sensitivity to initial asymmetry and the basic-state of a vortex, a set of sensitivity experiments are performed to examine how initial radial wavenumber ( $k_0$ ), initial vertical wavenumber ( $m_0$ ), radius where initial asymmetry is located ( $R_0$ ), RMW ( $r_m$ ), and maximum tangential velocity ( $v_m$ ) affect the VRW propagation associated with azimuthal wavenumber-1 and wavenumber-2 asymmetries. In these experiments, the baseline parameters are taken as follows:  $k_0 = \frac{1}{100} km^{-1}$ ,  $m_0 = \frac{1}{10} km^{-1}$ ,  $r_m = 70 km$ ,  $v_m = 36.8 ms^{-1}$ ,  $R_0 = 70 km$ ,  $Z_0 = 0 km$ , and  $\bar{v}_{z0} = -0.0032 s^{-1}$ . In each sensitivity experiment, only one parameter allows to vary while the rest keeps unchanged.

Figure 4.7 shows the stagnation radii and heights as the function of radial wavenumber  $k_\theta$  for azimuthal wavenumber-1 and wavenumber-2 asymmetry. Consistent with previous analyses, wavenumber-1 asymmetry shows substantial radial and vertical propagation compared with wavenumber-2 asymmetry. Baroclinicity suppresses radial propagation but enhances wave vertical propagation. It is clear that asymmetries with larger initial radial wavelength (smaller radial wavenumber) can propagate a longer distance in the radial and vertical directions than smaller radial wavelength asymmetries. But the dependence of the maximum propagation distance on radial wavenumber decreases as radial wavelength increases. As the figure indicated, for wavenumber-2 asymmetry the maximum propagation distance does not change much for radial wavelength greater than 100 km.

The sensitivity of VRW radial and vertical propagation to vertical wavenumber is shown in Fig. 4.8. The dependence of wave radial propagation on vertical wavenumber shares the similar characteristics to the dependence of wave radial propagation on radial wavenumber in the sense that small vertical wavenumber favors the wave radial propagation. However, such sensitivity decreases as vertical wavenumber decreases. For  $m_0^{-1} > 10$  km, the wave radial propagation is virtually insensitive to the further increase of vertical wavelength. This fact is true for both barotropic and baroclinic vortices. Interesting phenomena are shown in VRW vertical propagation. In baroclinic vortices, the dependence of wave vertical propagation on vertical wavenumber is similar to that of wave radial propagation. However for barotropic vortices, there exists a critical vertical wavelength about 3-4 km at which the wave vertical propagation reaches the peak. Vortex Rossby waves with large vertical wavelength are trapped in the low layer. Baroclinicity

substantially promotes the vertical propagation for large vertical wavelength perturbations. The reason is likely a result of the fact that the vertical gradient of basic-state vorticity provides an additional restoring mechanism for VRW vertical propagation as discussed in Chapters 2 and 3.

Figure 4.9 shows the dependence of VRW propagation on the radius where initial asymmetry is placed. It clearly shows that there is a critical radius for initial asymmetry where radial and vertical propagation reaches the maximum. The critical radius for radial propagation is slightly larger than that of vertical propagation. Since the RMW of the vortex is set to 70 km in the experiment, Fig. 4.9 shows that perturbations near the RMW can have the maximum radial and vertical propagation. Wave propagation reduces significantly for asymmetries excited away from the RMW likely due to the small vortex " $\beta$ " effect there. It is interesting to note that baroclinicity only has a marginal effect on the stagnation height for wavenumber-1 asymmetry in the vicinity of the critical radius despite the fact that baroclinicity shows a strong impact on wave radial propagation, suggesting that the relationship among VRW propagation, baroclinicity, and central radius of initial asymmetry is highly nonlinear.

The sensitivity of VRW radial and vertical propagation to RMW is shown in Fig. 4.10. For barotropic vortices, wave radial propagation does not appear to be much affected by RMW for RMW greater than 50 km. However, wave radial propagation is substantially suppressed by baroclinicity for storms with larger RMW. Since the initial asymmetry is placed at 70 km in this experiment, this result suggests that for larger size storms asymmetries excited inside the RMW can barely propagate radially outward in baroclinic conditions. On the other hand, asymmetries located near the RMW show the maximum

vertical propagation in baroclinic vortices. Both asymmetries inside and outside the RMW are trapped. The promotion of vertical propagation by baroclinicity also reaches the maximum for asymmetries near the RMW most likely because of the large vertical gradient of basic-state vorticity there.

Fig. 4.11 shows the sensitivity of VRW propagation to the maximum tangential velocity. For hurricane-strength vortices (i.e.,  $> 33$  m/s), the increase of maximum tangential velocity generally suppresses wave radial propagation but enhances wave vertical propagation. This is mainly based on the fact that the large maximum tangential velocity at the surface leads to strong vortex baroclinicity for a vortex whose vertical structure is determined by Eq. 4.2. As we showed previously, baroclinicity favors the vertical propagation of VRWs, and thus, it must be accompanied by the suppression of wave radial propagation constrained by the ‘critical’ surface represented by Eq. 3.28. This result suggests that as storm intensity increases asymmetries induced by diabatic heating or friction tend to propagate more vertically upward than radially outward.

#### **4.4 Extension to More Realistic Baroclinic TC Vortex**

Although the impact of baroclinicity on VRW propagation is clearly illustrated in Figs. 4.4-4.5 and Figs. 4.7-4.11, the constant vertical gradient of tangential velocity used in the analyses oversimplifies the vertical structure of a baroclinic vortex. To obtain a global picture of VRW propagation, we investigated the radial and vertical propagation of azimuthal wavenumber-1 and wavenumber-2 wave packets in the 3D baroclinic hurricane-strength and tropical-storm-strength vortices with strong ( $L=5000$  m) and weak ( $L=7500$  m) baroclinicity described in section 4.2. To simplify the problem, the initial radial and

vertical wavenumbers are set to  $1/70 \text{ km}^{-1}$  and  $1/10 \text{ km}^{-1}$  respectively in both hurricane-strength and tropical-storm-strength vortices. Figure 4.12 shows the stagnation radii of azimuthal wavenumber-1 asymmetries excited at different locations (radius and height) in both hurricane-strength and tropical-storm-strength vortices with weak and strong baroclinicity. Several interesting features are worthy to be emphasized here. First, perturbations excited at the surface near the RMW can have strong radial propagation in both hurricane-strength (RMW=70 km) and tropical-storm-strength (RMW=145 km) vortices consistent with the previous analyses. Second, asymmetries excited at the surface can propagate radially farther in the strong baroclinic vortex than in the weak baroclinic vortex. This result seems to be somewhat in conflict with the previous conclusion that baroclinicity limits the wave radial propagation. However, we note that the baroclinicity (measured by the vertical gradient of tangential velocity indicated by the dashed contours) at the surface is nearly identical in the weak and strong baroclinic vortices. The nonlinear relation of Eq. 2.23 results in the larger stagnation radii in the strong baroclinic vortex than the weak baroclinic vortex. As baroclinicity becomes stronger with the increase of height, the wave radial propagation in the strong baroclinic vortex is quickly suppressed. At about 4 km altitude, waves can propagate farther in radius in the weak baroclinic vortex than in the strong baroclinic vortex. Finally, the difference of stagnation radii between tropical-storm-strength and hurricane-strength vortices is only marginal, suggesting that storm intensity does not have much influence on wave radial propagation. Similar results for wave radial propagation are found for azimuthal wavenumber-2 asymmetries except for a much shorter radial distance travelled by VRW packets (Fig. 4.13). An important difference

is that for wavenumber-1 asymmetries the longest wave radial propagation occurs near the RMW whereas it is shifted to the outside of RMW for wavenumber-2 asymmetries.

The stagnation heights for wavenumber-1 asymmetries are shown in Fig. 4.14. Unlike the maximum radial propagation occurring at the surface, waves excited at the surface can barely propagate upward because of the weak baroclinicity there. Thus, asymmetries generated at the surface are basically trapped in the low layer. Asymmetries excited aloft can effectively propagate upward supported by baroclinicity. For the maximum vertical propagation, waves must be excited aloft in the low to mid troposphere within the RMW. Asymmetries excited outside the RMW cannot effectively propagate upward. It is also interesting to see that wave vertical propagation is substantially suppressed in the tropical-storm-strength vortex compared with that in the hurricane-strength vortex. This is most likely due the fact that the weak vertical gradient of tangential velocity in the tropical-storm-strength vortex suppresses the vertical propagation of VRWs. Thus, one may expect the stronger vertical propagation as storm intensity gets stronger. Fig. 4.15 shows the stagnation heights for azimuthal wavenumber-2 asymmetries. Similar results to those of wavenumber-1 asymmetries are obtained except for much shallower vertical propagation. Particularly for tropical-storm-strength vortices, asymmetries cannot effectively propagate upward.

#### **4.5 Summary and Conclusions**

Applying the generalized wave formulae derived in Chapter 2 to baroclinic monopole vortices, we investigated the impact of baroclinicity on the radial and vertical propagation of VRWs. The key findings are summarized as follows.

First, our calculations show that baroclinicity promotes the vertical propagation of VRWs. Physically, this is easy to understand: just like the radial gradient of basic-state vorticity that supports radial propagation of VRWs, the vertical gradient of vorticity and mean-flow should favor vertical propagation of VRWs. However, due to the nonlinear effect, the impact of baroclinicity on VRW propagation is complicated. For the baroclinic monopole vortices constructed in this study, waves excited at the surface behave like those in barotropic vortices in that they are trapped in the low layer with substantial radial propagation, whereas waves excited in the low to mid troposphere of inner-core region can most effectively propagate upward but their radial propagation is largely suppressed. In contrast, perturbations excited outside the RMW cannot effectively propagate upward. The implication is that the wave-mean-flow interaction associated with the asymmetries generated aloft by the diabatic heating of inner eyewall and outer rainband and by surface friction may not simply follow what was depicted by the 2D nondivergent model and 3D barotropic model of MK97 and MM00. Numerical simulations are needed further to clarify the issue of wave-mean-flow interaction in baroclinic vortices.

Second, our analyses show that only low azimuthal wavenumber (1 and 2) asymmetries can have meaningful radial and vertical propagation. The radial and vertical propagation of high wavenumber asymmetries is negligible. The characteristics of wave propagation depend strongly on the initial radial wavenumber and vertical wavenumber of asymmetries, the initial location (both radius and height) where asymmetries are excited, RMW and maximum tangential velocity of vortices, and the strength and vertical structure of basic-state baroclinicity. In general, asymmetries excited in the vicinity of RMW can propagate farther than those away from the RMW. This result suggests that asymmetries

associated with eyewall and outer rainbands may play different roles in storm intensification.

The above important features of VRW propagation in baroclinic vortices are obtained from pure linear theoretical analyses in the AB model framework without considering the detailed vortex thermodynamic structure, and thus, it is interesting to see if the theoretically predicted wave features can be reproduced in numerical simulations that include all neglected but possibly important factors. Moreover, the theoretical analyses presented here lack the ability to address the issues regarding wave-mean-flow interaction and its role in storm intensification. To explore these issues, a series of nonhydrostatic simulations by the Weather Research and Forecasting (WRF) model based on the same baroclinic monopole vortices and asymmetric perturbations constructed in this chapter have been conducted. The results show that the main features of simulated wave propagation are remarkably consistent with our theoretical predictions. The simulations further show that the unique radial and vertical wave propagation in baroclinic vortices leads to interesting wave-mean-flow interaction with characteristics different from that in barotropic vortices. These results will be presented in the next two chapters.

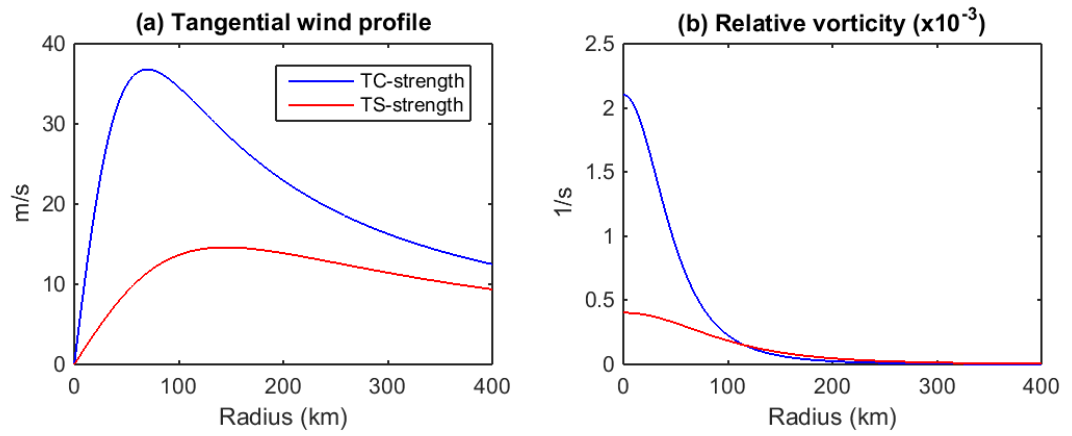


Fig. 4.1: Basic-state swirl profiles for hurricane-strength and tropical-storm-strength vortices used in this study. (a): Tangential velocity (m/s); (b): relative vorticity ( $1/s$ ).

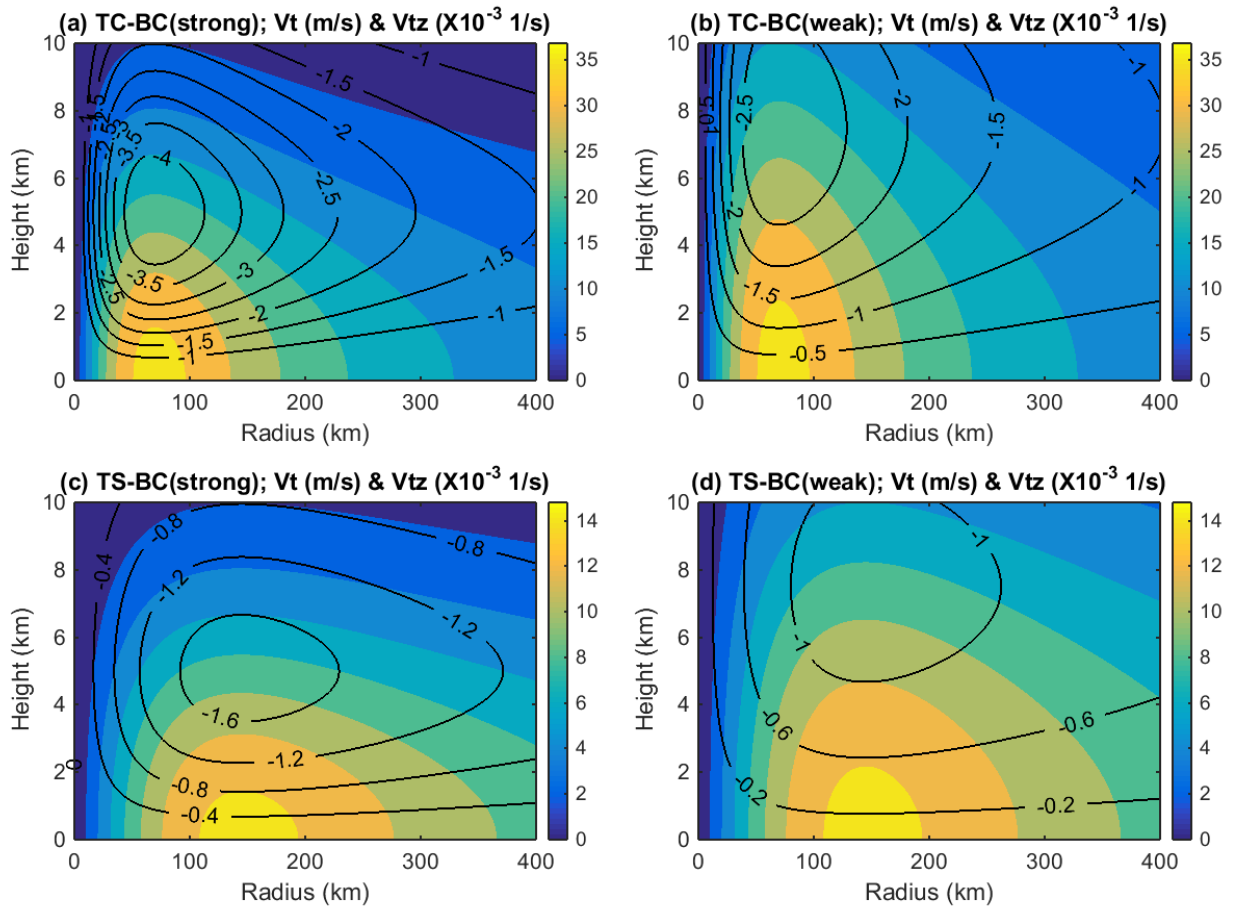


Fig. 4.2: Radius-height plots of tangential velocity (m/s, color shades) and vertical gradient of tangential velocity ( $10^{-3} 1/s$ , contours). (a): Hurricane-strength vortex with strong baroclinicity; (b): Hurricane-strength vortex with weak baroclinicity; (c): Tropical-storm-strength vortex with strong baroclinicity; (d): Tropical-storm-strength vortex with weak baroclinicity.

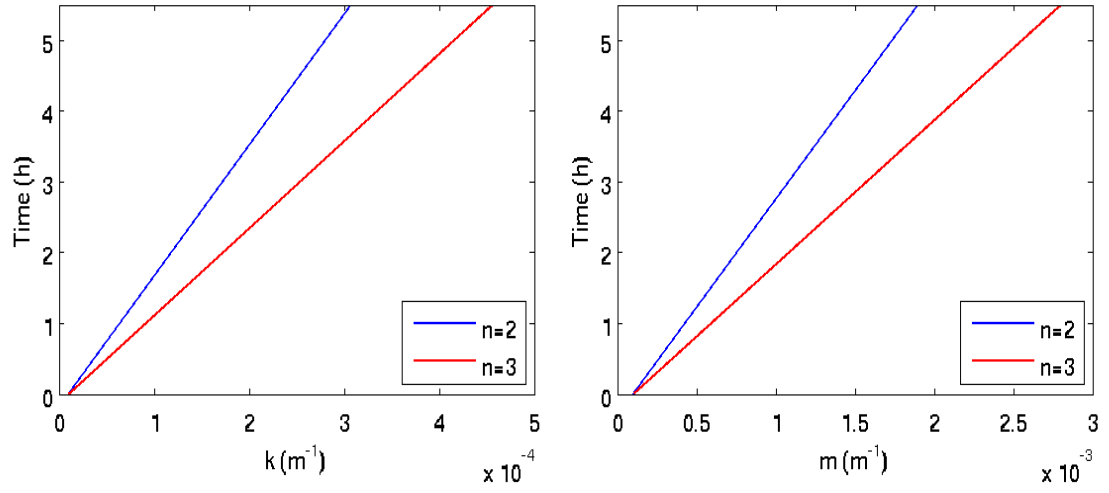


Fig. 4.3: Time variation of radial wavenumber  $k$  and vertical wavenumber  $m$  for azimuthal wavenumber 2 and 3 for the hurricane-strength vortex constructed in this study.

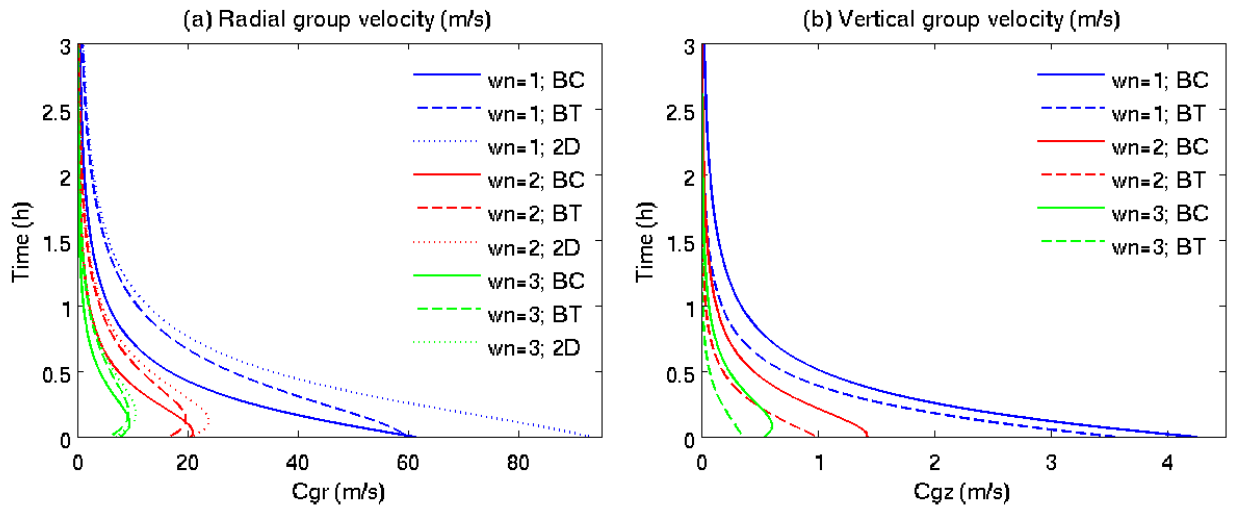


Fig. 4.4: Radial (a) and vertical (b) group velocities of wavenumber-1, wavenumber-2, and wavenumber-3 in hurricane-strength 2D non-divergent, 3D barotropic, and 3D baroclinic vortex.

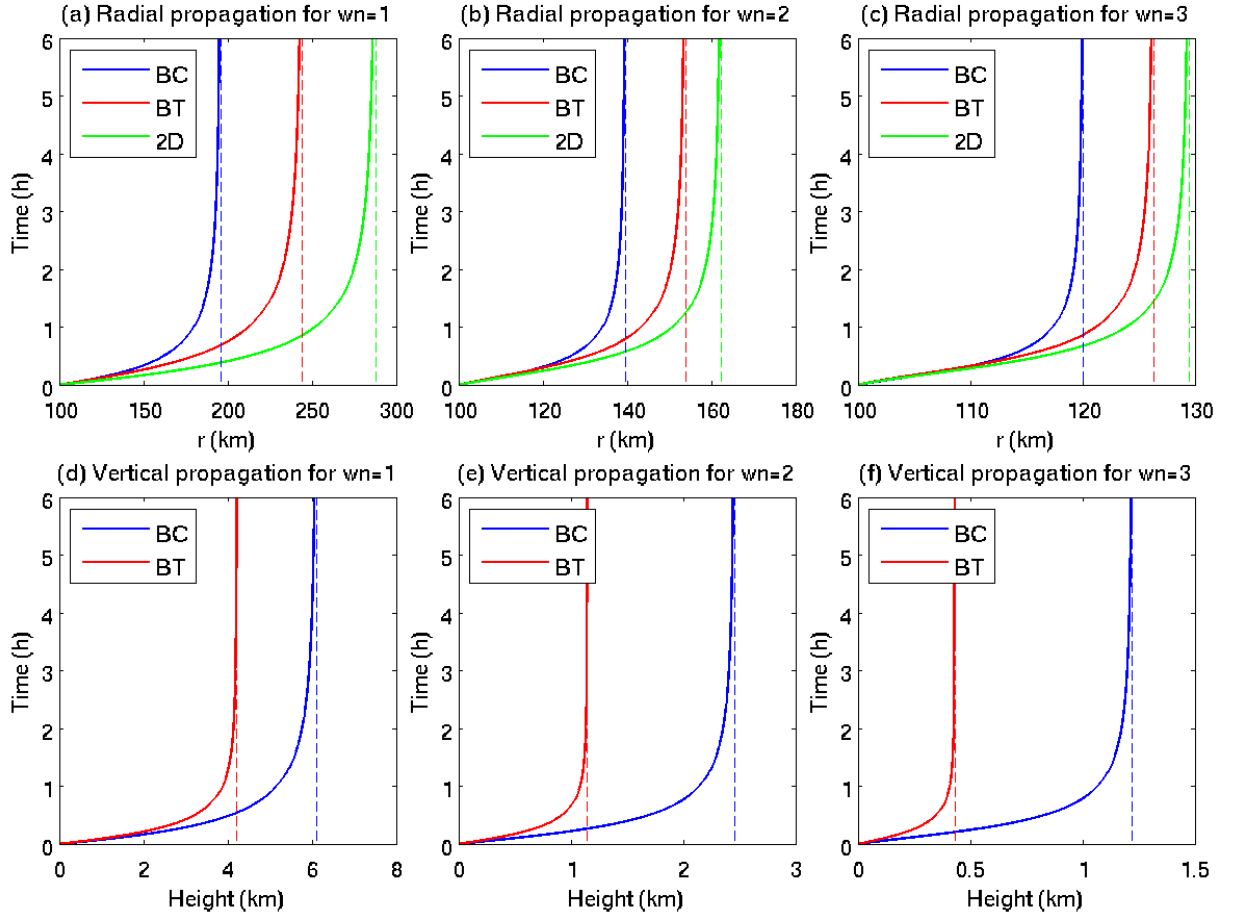


Fig. 4.5: Wave radial trajectories (upper row) and vertical trajectories (bottom row) of wavenumber-1, wavenumber-2, and wavenumber-3 in 2D nondivergent (green), 3D barotropic (red), and 3D baroclinic (blue) vortices. The dashed vertical lines indicate the stagnation radii and heights computed by Eqs. 2.32-2.33.

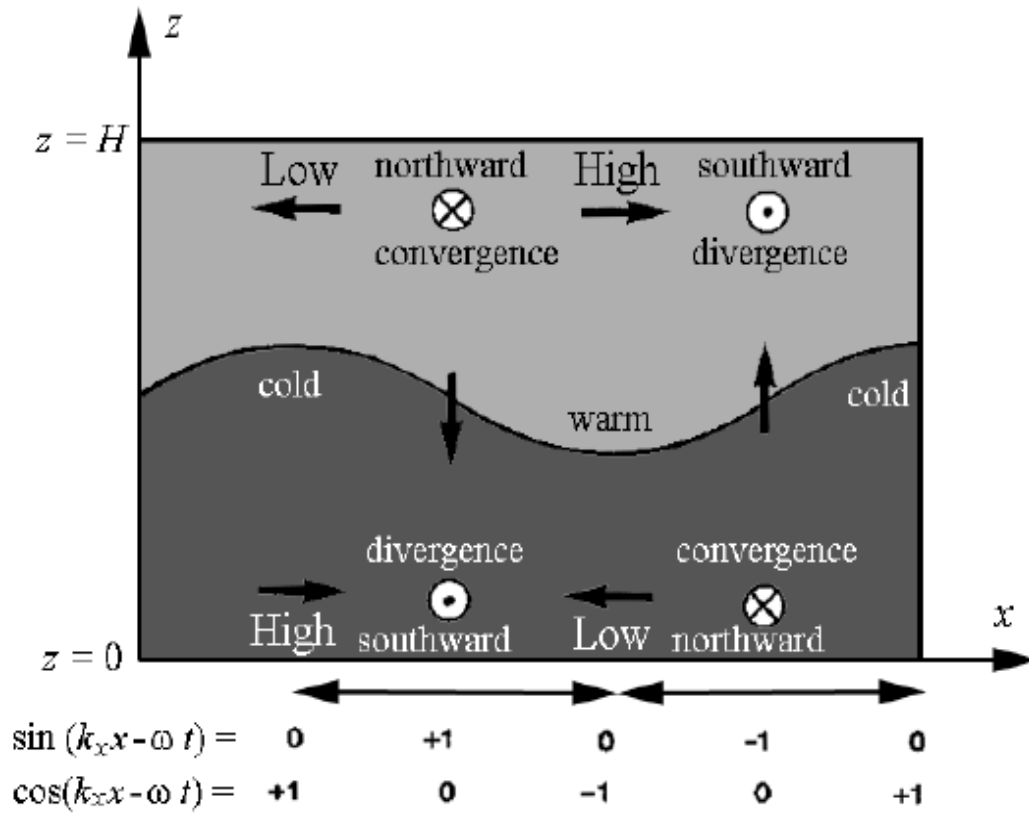


Fig. 4.6: Structure of planetary Rossby wave propagation in a barotropically stratified fluid (after Cushman-Roisin and Beckers 2006).

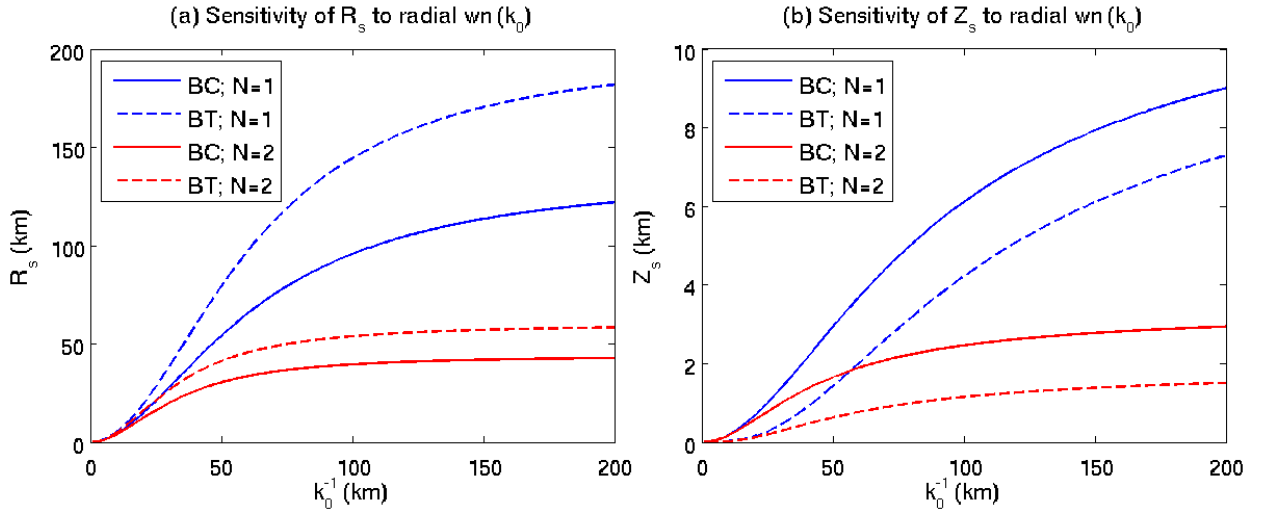


Fig. 4.7: Sensitivity of stagnation radii (a) and stagnation heights (b) to initial radial wavenumber,  $k_0$ .

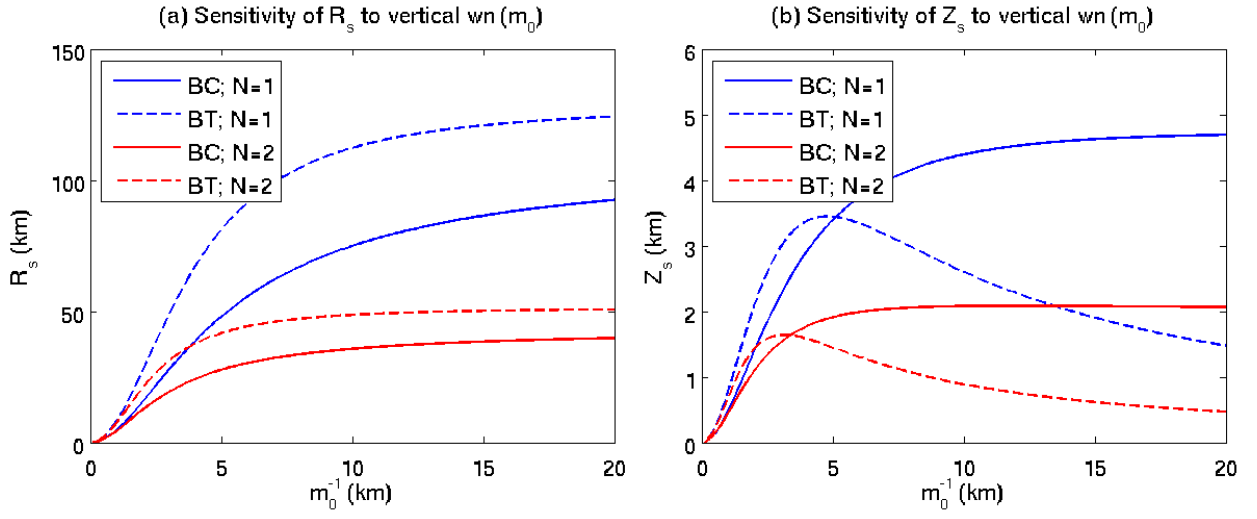


Fig. 4.8: Sensitivity of stagnation radii (a) and stagnation heights (b) to initial vertical wavenumber,  $m_0$ .

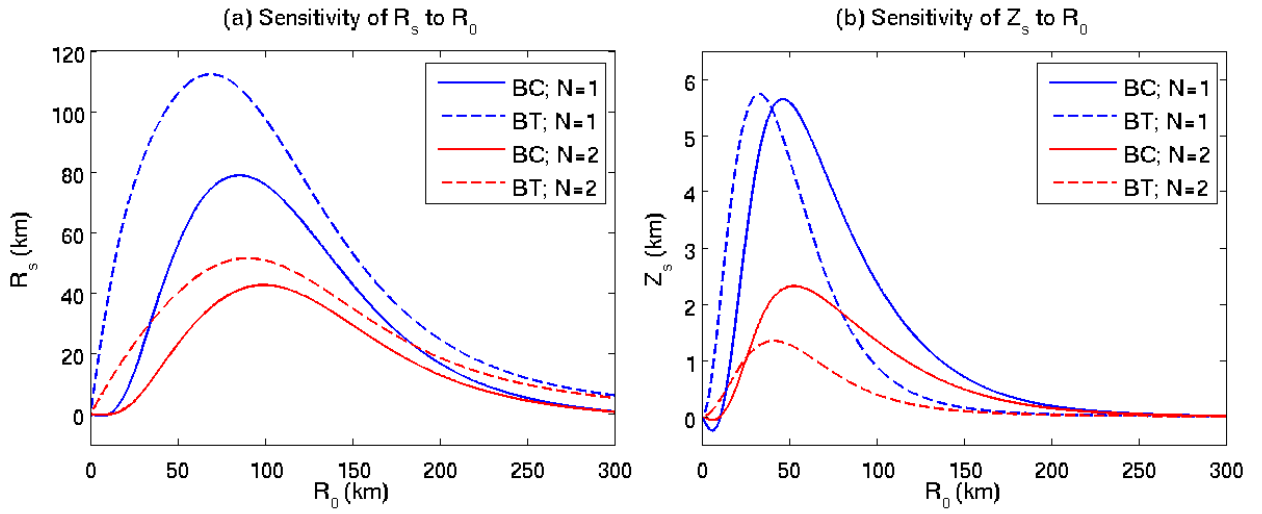


Fig. 4.9: Sensitivity of stagnation radii (a) and stagnation heights (b) to the radius where the asymmetry is initially placed.

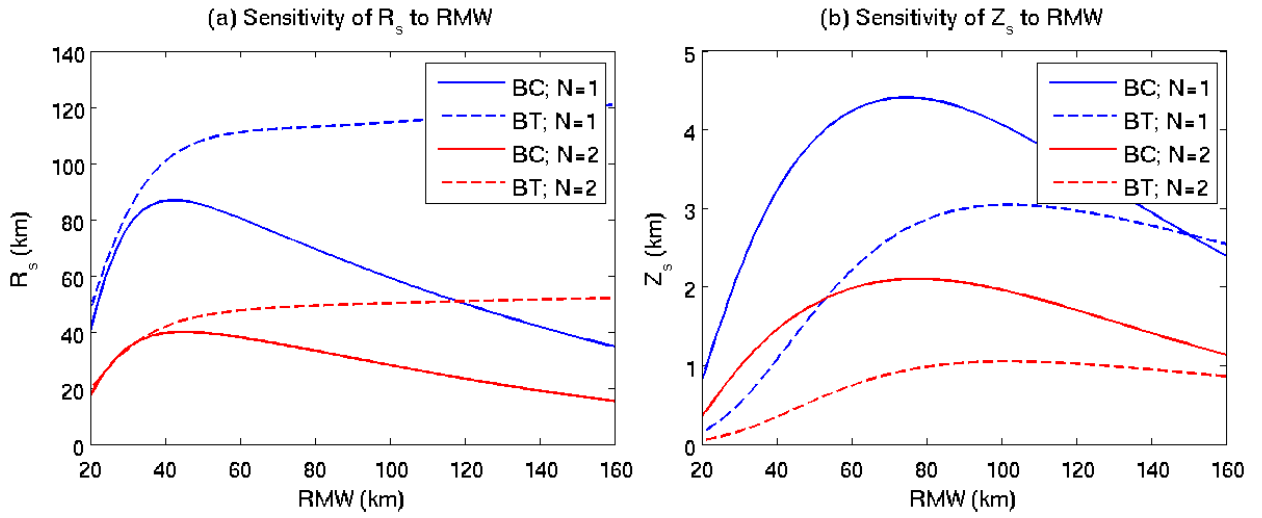


Fig. 4.10: Sensitivity of stagnation radii (a) and stagnation heights (b) to RMW.

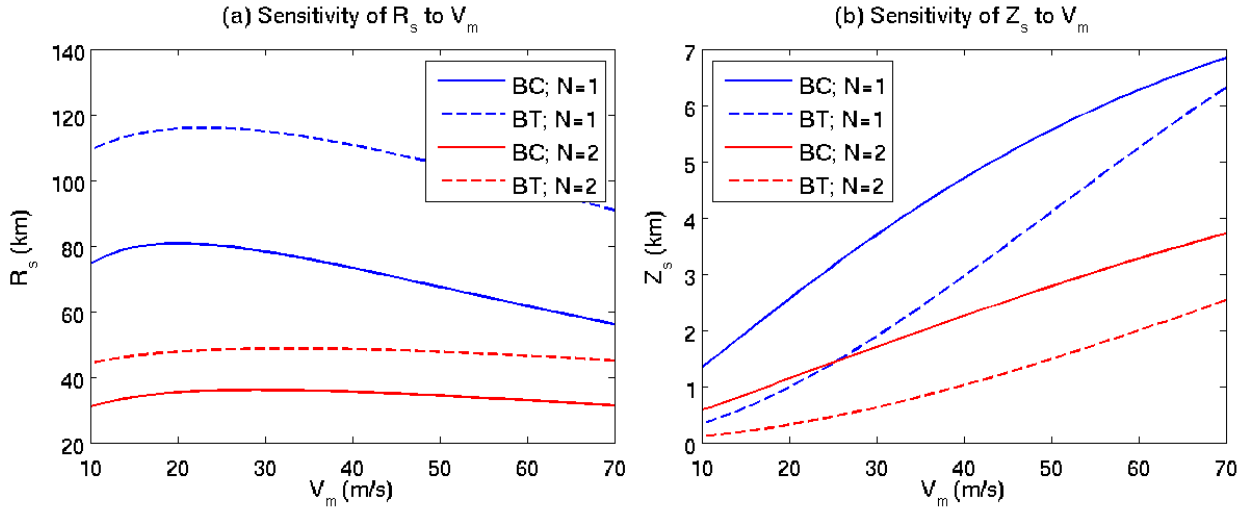


Fig. 4.11: Sensitivity of stagnation radii (a) and stagnation heights (b) to maximum tangential velocity.

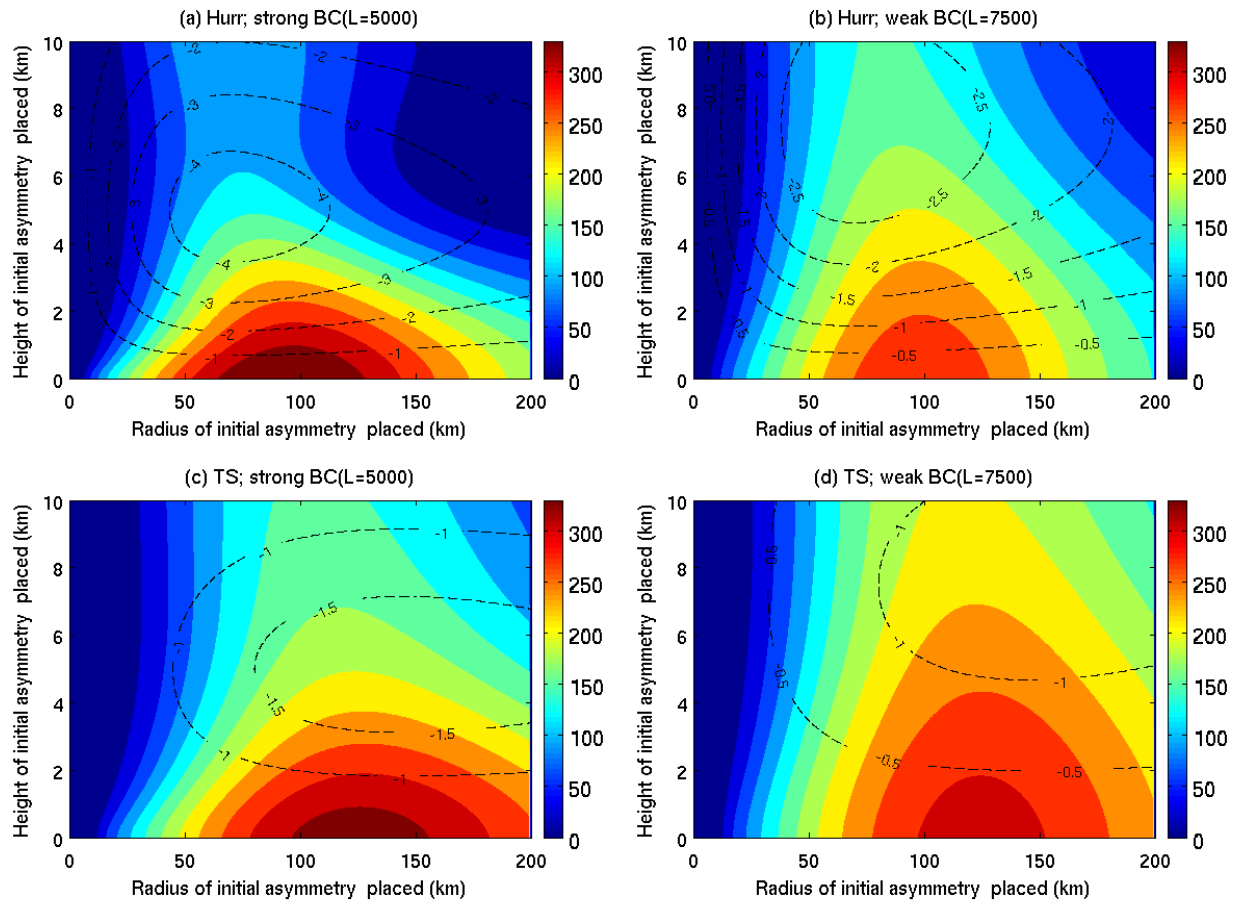


Fig. 4.12: Stagnation radii (km, color shades) for azimuthal wavenumber-1 asymmetries excited at different radii (x-axis) and heights (y-axis) for (a): a hurricane-strength vortex with strong baroclinicity ( $L=5000$ ); (b): a hurricane-strength vortex with weak baroclinicity ( $L=7500$ ); (c): a tropical-storm-strength vortex with strong baroclinicity ( $L=5000$ ); and (d): a tropical-storm-strength vortex with weak baroclinicity ( $L=7500$ ).

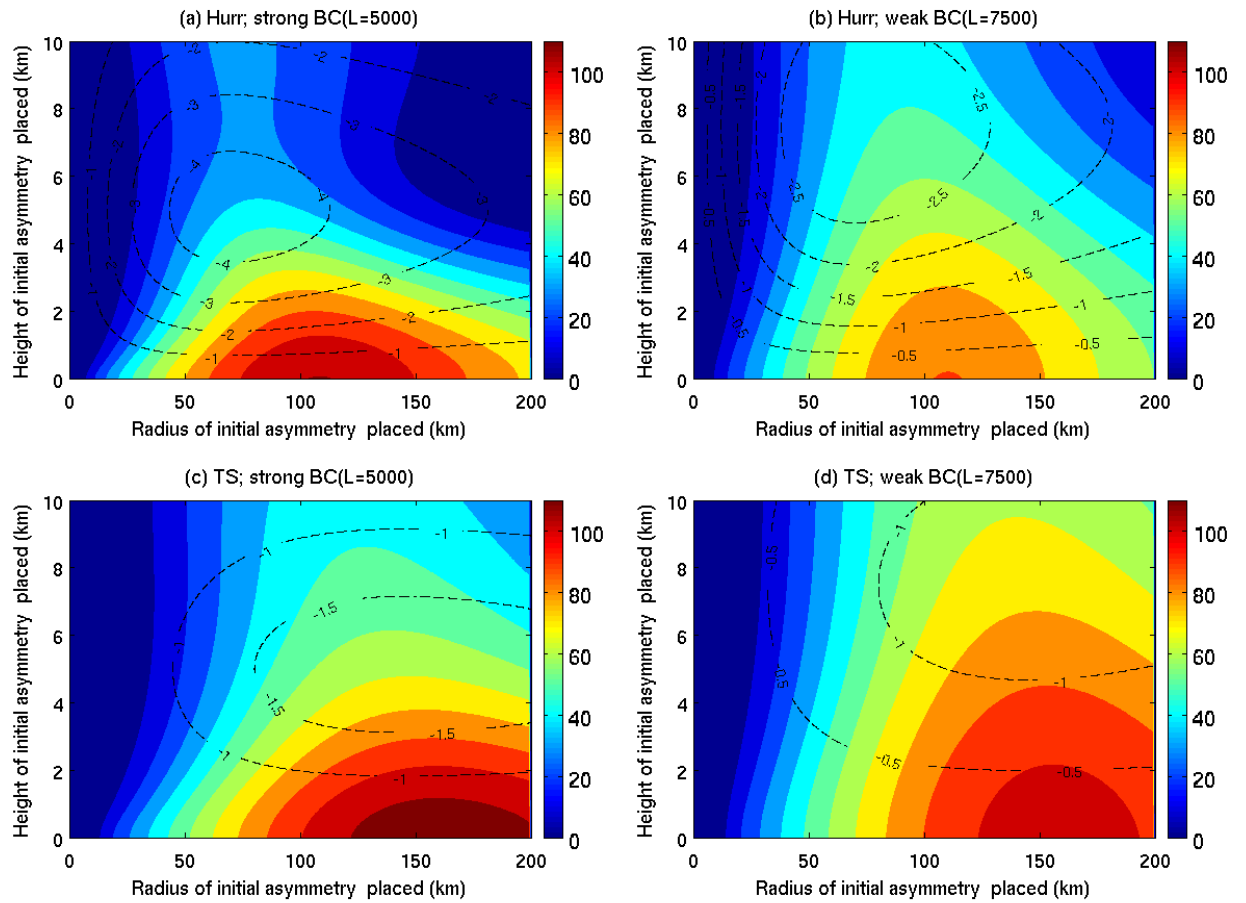


Fig. 4.13: The same as Fig. 4.12 but for azimuthal wavenumber-2 asymmetries.

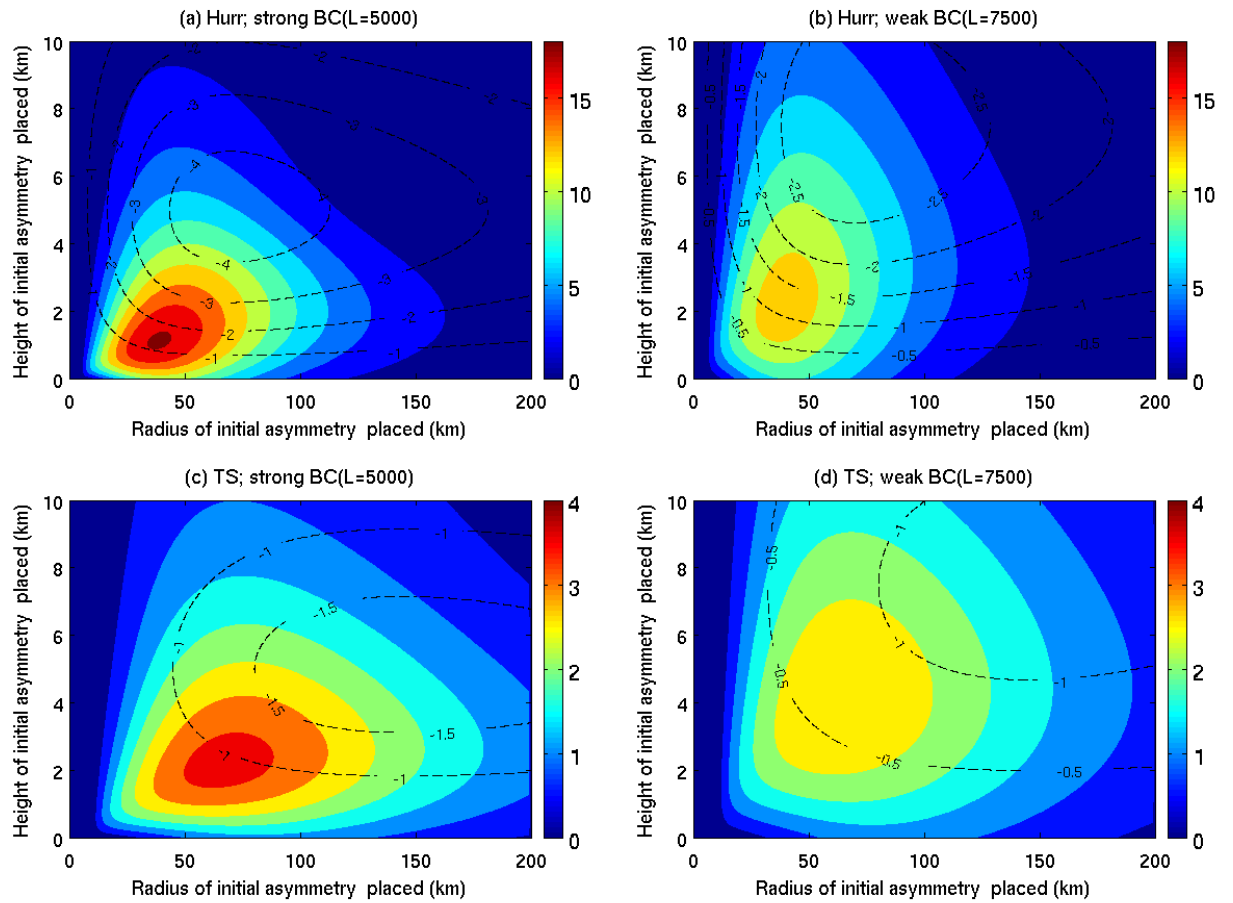


Fig. 4.14: Stagnation height (km, color shades) for azimuthal wavenumber-1 asymmetries excited at different radii (x-axis) and heights (y-axis) for (a): a hurricane-strength vortex with strong baroclinicity ( $L=5000$ ); (b): a hurricane-strength vortex with weak baroclinicity ( $L=7500$ ); (c): a tropical-storm-strength vortex with strong baroclinicity ( $L=5000$ ); and (d): a tropical-storm-strength vortex with weak baroclinicity ( $L=7500$ ).

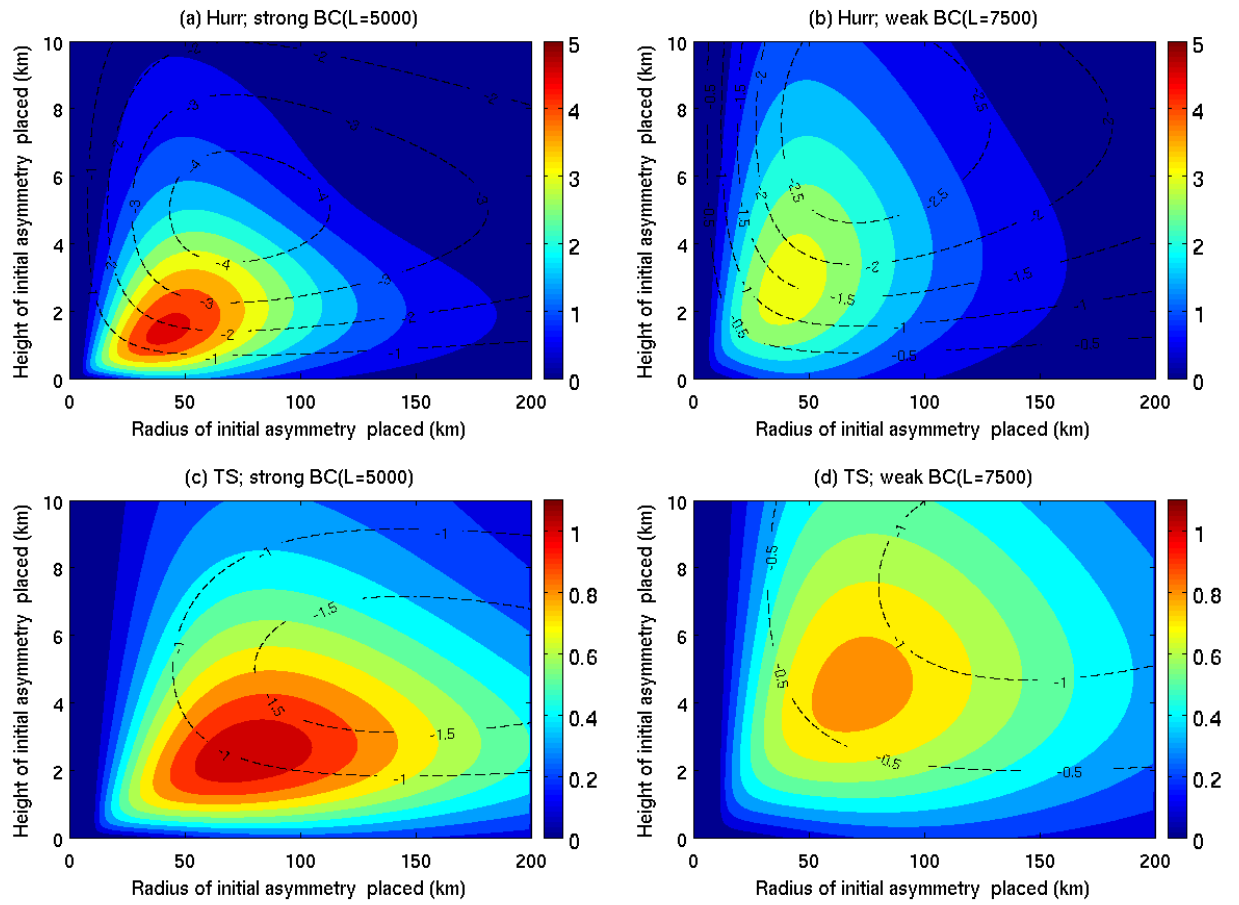


Fig. 4.15: The same as Fig. 4.14 but for azimuthal wavenumber-2 asymmetries.

# CHAPTER 5: WRF Simulation of VRW Propagation in Baroclinic TC-like Vortices. Part I: Asymmetric Structure and Evolution

## 5.1 Introduction

In pervious chapters, a generalized VRW theory in the 3D baroclinic vortex has been developed within the AB model framework. Using the WKB analysis, the wave dispersion relation, group velocities, and stagnation radius and height of VRWs have been successfully derived in both pseudo-height and isentropic coordinates. As stated in Section 2.1, the AB theory views a 3D asymmetric TC as a rapidly rotating vortex but with a slow macroscopic evolution governed by the order one divergence (SM93; McWilliams 1995). The basic assumption of the AB theory is represented by Eq. 2.1, which may be rewritten as,

$$R^2 = \frac{D_v^2() / Dt^2}{S^2} \ll 1, \quad (5.1)$$

where  $R = \frac{D_v() / Dt}{S}$  is considered as the Rossby number of a TC vortex. The tangential wind may be decomposed into its symmetric and asymmetric components as,

$$v = \bar{v} + \sum_{n \geq 1} v'_n, \quad (5.2)$$

where n indicates the azimuthal wavenumber. Assuming that the local change rate of mean tangential wind,  $\frac{\partial \bar{v}}{\partial t}$ , has the same magnitude as the advective rate,  $\frac{\bar{v}}{r} \frac{\partial \bar{v}}{\partial \lambda}$ , in the material derivative. Then, applying Eq. 5.1 to tangential wind, the AB assumption for azimuthal wavenumber-n asymmetry becomes,

$$R_n^2 = \frac{n\bar{v}^2 / r^2}{S^2} \ll 1, \quad (5.3)$$

where to obtain Eq. 5.3, a simple scaling,  $\frac{D_v \bar{v}}{Dt} \sim \frac{\partial \bar{v}}{\partial t} \sim \frac{\bar{v}}{r} \frac{\partial \bar{v}}{\partial \lambda} \sim \frac{n\bar{v}}{r}$ , has been applied. The inertial stability,  $S$ , in a constant height surface of a symmetric vortex can be written as (SM93),  $S^2 = \bar{\eta} \bar{\xi} = (f + \frac{1}{r} \frac{\partial(r\bar{v})}{\partial r})(f + 2\frac{\bar{v}}{r}) = (f + \frac{\bar{v}}{r} + \frac{\partial \bar{v}}{\partial r})(f + 2\frac{\bar{v}}{r})$ . Thus, Eq. 5.3 may be rewritten as,

$$R_n^2 = \frac{n\bar{v}^2 / r^2}{(f + \frac{\bar{v}}{r} + \frac{\partial \bar{v}}{\partial r})(f + 2\frac{\bar{v}}{r})} \ll 1. \quad (5.4)$$

Near the RMW of a rapid rotating vortex,  $f \ll \frac{\bar{v}}{r}$  should be true. This suggests that the Rossby number for wavenumber-1 asymmetry,  $R_1^2$ , should be smaller than 0.5. Indeed, the detailed scaling analysis performed by SM93 showed that  $R_1^2 \ll 1$  is generally satisfied for most of areas of Hurricane Gloria (1985). For wavenumber-2 asymmetry, the same rough scaling estimate suggests that  $R_2^2$  is at the order of 1, which would indicate that the AB approximation is valid only for wavenumber-1 asymmetry but not for higher wavenumber asymmetries. However, Moller and Montgomery (1999, hereafter MM99) argued that such a scaling analysis may be a little too inaccurate or “naïve” since the material derivative  $\frac{D_v(\cdot)}{Dt}$  may be substantially smaller than the simple scaling estimate due to cancellation between the local change and advection in  $\frac{D_v(\cdot)}{Dt}$ .

To investigate if the AB approximation remains to be valid for higher wavenumber asymmetries, MM99 closely examined the characteristics of wavenumber-1, wavenumber-2, and wavenumber-3 asymmetries simulated by a barotropic AB model and by a primitive equation (PE) shallow-water model. The comparisons show that the AB model simulated wave propagation and wave-mean-flow interaction are remarkably similar to those simulated by the PE model not only for wavenumber-1 asymmetry but for wavenumber-2 and wavenumber-3 asymmetries as well. MM99 further explored the underlying reason why the AB model can qualitatively reproduce the results of the PE model despite  $R_n^2 > 1$  for  $n > 1$  obtained from the simple scaling analysis. Their analysis confirmed that the square of local Rossby number is indeed much smaller than the value of simple scaling analysis, i.e.,  $R^2 = \frac{D_v^2 \bar{v} / Dt^2}{S^2} \ll \frac{n \bar{v}^2 / r^2}{S^2}$ , because of the cancelation between the local change and advection terms.

Although MM99's conclusion rooted the application of AB theory to high wavenumber asymmetries in a solid ground, MM99's investigation was based on a barotropic model. Our theoretical derivation and analyses presented in the previous chapters show that baroclinicity can have important bearings on the wave kinematic of the VRWs. What remain to be unaddressed are (a) if our theoretical prediction of VRW propagation in 3D baroclinicity vortices by the linearized WKB analyses under the AB approximation framework can be reproduced by 3D non-hydrostatic models and (b) how baroclinicity affects the wave-mean-flow interaction in vortex intensification. To answer these questions, the non-hydrostatic Weather Research and Forecasting (WRF) model is used for the study. This chapter presents the results of validating our theoretical prediction

of VRWs using WRF simulations and examining the structural change of asymmetries during the vortex axisymmetrization in WRF simulations.

## 5.2 Numerical Experiment Design and WRF Model Setup

The WRF model with the Advanced Research WRF (ARW) dynamical core, version 3.3.1, is used for all simulations performed in this study, the WRF-ARW is a fully compressible, nonhydrostatic model (Shamarock et al. 2008), and has been widely used for both real and idealized TC simulations. In all simulations performed in this study, the model surface is set to be water only, and the sea surface temperature (SST) is uniformly fixed to  $28^{\circ}\text{C}$ . All the map factors are set to 1 and the reciprocal of the earth radius is set to 0 so that the computations are carried out on a Cartesian coordinate grid. All the simulations are performed on an f-plane with a constant Coriolis parameter set to a value equivalent to that at  $20^{\circ}\text{N}$ . The periodic lateral boundary condition and symmetric lateral boundary condition (free-slip wall) are applied to the western/eastern boundaries and southern/northern boundaries, respectively (Nolan 2011). All the simulations contain two two-way nested square domains with a horizontal resolution of 6, 2km, respectively. The outer and inner domains are both configured by  $361 \times 361$  gridpoints. The inner domain gives a size of  $720\text{km} \times 720\text{km}$ , which is large enough to cover the evolution of the inner core structure of a simulated TC. All the simulations use 43 vertical levels with a model top at 25hPa. During all the simulations, the model physics is closed and the sub-grid scale (SGS) diffusion is neglected by specifying zero eddy exchange coefficient  $K_m$  and  $K_h$ .

### 5.3 Basic State Vortices and Asymmetry Initialization

#### 5.3.1 Methodology of Balanced Vortices Construction

In this study, we decompose a generic variable  $s$  into the azimuthal-mean of the variable and the deviation from the mean in a cylindrical coordinate as,

$$s(r, \lambda, z, t) = \bar{s}(r, z, t) + s'(r, \lambda, z, t). \quad (5.5)$$

The perturbations are then represented as a sum of functions with harmonic variations in the azimuthal direction. A decomposed perturbation with azimuthal wavenumber  $n$  ( $n > 0$ ) is called  $wn$ - $n$  perturbation. For example, the vorticity perturbation field with azimuthal wavenumber 2 is simply termed  $wn$ -2 vorticity. The wavenumber zero component, then, represents the mean field. We use the mean fields to describe the basic-state vortices.

All the simulations are initialized with an idealized vortex embedded in a homogeneous quiescent background. The vortex is placed at the center of the domains, and the surface layer radial profile is specified with the same formula used in MK97 (i.e., Eq 4.1). We consider the hurricane-strength vortices (CAT-1 vortices) with  $v_m = 36.8 \text{ m/s}$ ,  $r_m = 70 \text{ km}$ . The mean velocity field is extended into the vertical using Eq 4.2, the same used in Nolan et. al (2007). The radius-height structure of tangential wind of basic-state vortices with strong and weak baroclinicity is shown in Fig. 5.1 and Fig. 5.2, respectively. For details of construction of the wind field of 3D baroclinic vortices, please refer to Section 4.1. In our theoretical analysis, the background stratification is prescribed with a constant  $N^2 = 1.2 \times 10^{-4} \text{ s}^{-2}$ . The detailed thermodynamic structure of the vortex is not needed in the WKB analyses. In 3D non-hydrostatic WRF simulations, however, the initial vortex

thermodynamic structure needs to be determined. Here, we assume that the initial thermodynamics fields that hold the vortex determined by Eqs. 4.1-4.2 are in gradient wind balance and the hydrostatic balance. In a pseudo-height coordinate, the pseudo-height  $z$  is defined as (Hoskins and Bretherton (1972)),

$$z = \left[ 1 - \left( \frac{\bar{p}}{p_0} \right)^{\frac{\gamma-1}{\gamma}} \right] \frac{\gamma}{\gamma-1} H_s, \quad (5.6)$$

where  $p_0 = 10^5 Pa$  is the reference pressure,  $H_s = 10km$  is the scale height, and  $\gamma$  is the ratio of specific heats. Once pseudo-heights are specified, the mean pressure on each pseudo-height can be calculated by Eq. 5.2. The radius-height distribution of mean pressure in the pseudo-height coordinate is shown in Fig 5.3. The increments in pseudo height  $\delta z$  are connected to the increments in the physical height  $\delta h$  by the equation (Hoskins and Bretherton 1972),

$$\bar{\theta} \delta z = \theta_0 \delta h, \quad (5.7)$$

where  $\theta_0$  is the reference potential temperature taken as 300 K. For a certain environmental static stability  $N^2$ , the thermodynamic field of a vortex with the tangential wind determined by Eqs. 5.1-5.2 can be determined by the hydrostatic balance, gradient wind balance, and thermal wind relation represented by Eqs. 2.2-2.4. The detailed procedures are described as follows.

To be consistent with our theoretical analyses, a constant environmental stratification of  $N^2=1.2e^{-4}s^{-1}$  is also used in the WRF simulations. From Eqs. 2.4-2.3, the mean geopotential  $\bar{\phi}$  and mean potential temperature  $\bar{\theta}$  fields can be determined. First, for the homogeneous surrounding far away from the vortex inner-core region ( $r=1000km$ ),

the geopotential  $\bar{\phi}$  on each level is obtained by multiplying  $z$  by gravity  $g$ . An inward integration of  $\bar{\phi}$  based on Eq. 2.3 yields the value for each grid point. Second,  $\bar{\theta}$  at the radius ( $r=1000\text{km}$ ) on each level is obtained by integrating  $N^2 = \frac{g}{\theta_0} \frac{\partial \bar{\theta}}{\partial z}$  upward based on the specified  $N^2$ , where  $\bar{\theta}$  at the surface is assumed to equal to  $\theta_0$ . Finally,  $\bar{\theta}$  on each grid point is obtained via an inward integration of Eq. 2.4. In such a way, all thermodynamics variables that hold the wind field of a vortex,  $\bar{v}(r, z)$ , can be determined. The radial–height distribution of  $\bar{\theta}$  for the hurricane-strength vortices with  $N^2 = 1.2e - 4s^{-1}$  is shown in Fig 5.4. In the next section, I will discuss why the mean vortex flow in the low to mid troposphere is baroclinic whereas that near the surface can be considered as quasi-barotropic flow.

### ***5.3.2 Baroclinic Flow and Quasi-Barotropic Flow in 3D Baroclinic Vortices***

In fluid dynamics, the baroclinicity of a stratified fluid measures how the misaligned gradient of pressure is from the gradient of density. In a barotropic atmosphere, the density lines (surfaces with constant density) are parallel to the isobars (surfaces with constant pressure), whereas in baroclinic atmosphere the density lines cross the isobars. Since density is related to temperature, it is also true that the isotherms cross the isobars in the baroclinic atmosphere. As showed in Fig 5.3, the isobars in the pseudo-height coordinates are parallel to the horizontal plane, thus, examining the tilting of isobars in a vortex provides a convenient way to identify the baroclinicity of the basic-state vortex flow.

Fig 5.4 shows the isotherms in the pseudo-height coordinates for both weak and strong baroclinic vortices under the environmental stratification  $N^2 = 1.2e - 4s^{-1}$ . The exponential function of  $\bar{v}_z$  (Eq. 4.2) leads to the large isotherm's slope in the low- to middle- troposphere in the vortex inner-core region. The low boundary of the region with apparent isotherm slope is approximately 2 km. The upper boundary is at 10 km and 12 km in strong and weak baroclinic vortices, respectively. Radially, this region is approximately from the vortex center to  $r=110$ km. The baroclinicity below  $z=2$ km in both strong and weak baroclinic vortices, however, is very weak since the slope of the isotherms is nearly zero. Thus, although the basic-state of the vortex is baroclinic as a whole, the mean flow near the surface may be considered as quasi-barotropic.

In our theoretical derivations, we have shown the distinct features of VRW propagation in barotropic and baroclinic condition. In baroclinic condition, the vortex ' $\beta$ ' effect  $\bar{q}_f$ , includes an extra term associated with the vertical gradient of the mean PV. In the meantime, the vertical shearing effect associated with the vortex baroclinicity results in the increase of vertical wavenumber. The combined effects promote the vertical propagation of VRWs. However, the maximum VRW propagation distance is strictly constrained by the critical surface (Eq. 3.31). Thus, a suppression of radial propagation must occur due to the promoted vertical propagation.

Fig 5.5 shows the radius-height distribution of  $\bar{q}_f$  overlaid with the corresponding vortex radial shear  $r\bar{\Omega}_r = r\partial\bar{\Omega}/\partial r$  (Fig 5.5a) and vortex vertical shear  $\bar{v}_z = \partial\bar{v}/\partial z$  (Fig 5.5b) of the weak baroclinic vortex. The vortex ' $\beta$ ' effect is indicated by the color shades, while the vortex radial/vertical shearing effect is shown by the dashed lines. The maximum

vortex ‘ $\beta$ ’ effect is located at the surface near  $r=40\text{km}$ . The strong vortex ‘ $\beta$ ’ effect extends to a height  $z=6\text{km}$  in the vortex inner core region (70% of the peak value). The maximum vortex radial shear occurs in the vicinity of the RMW at the surface where the vortex vertical shear is almost the weakest. On the other hand, the maximum vortex vertical shear is located in the middle troposphere near the RMW where the vortex radial shear reduces more than half of its maximum. A similar distribution of  $\bar{q}_f$ , vortex radial shearing, and vertical shearing can be found in the strong baroclinic vortex (Fig 5.6), where the maximum vortex ‘ $\beta$ ’ effect still falls at  $r=40\text{km}$  but is elevated to  $z=2.5\text{km}$ . The distribution of both vortex radial shearing and vertical shearing is nearly the same as that in the weak baroclinic vortex except that the vortex vertical shearing is stronger than that in the weak baroclinic vortex. Figures 5.5 and 5.6 clearly illustrate the distinct feature of vortex ‘ $\beta$ ’ effect and vortex shearing effect of the baroclinic and the quasi-barotropic mean flow in a baroclinic vortex. I will show shortly that the characteristics of VRW propagation in the 3D non-hydrostatic WRF simulations are mainly determined by the baroclinic and quasi-barotropic mean flow of the vortex and are consistent with our theoretical analyses.

### ***5.3.3 Experiment Design and Asymmetry Initialization***

In order to clearly illustrate the distinct VRW propagation features in the baroclinic and quasi-barotropic mean flow, the initial symmetric vortices are perturbed by an asymmetry whose radial-height distribution is prescribed by the same formula used in MM00. The first set of experiments (named as LB01 hereafter) is based on the weak baroclinic vortex in which the maximum of initial asymmetry is placed at the RMW ( $r_c = r_m$ ) and on the surface ( $z_c = 0$ ). In order to examine if our theoretical analyses can be

extended to higher wavenumber asymmetries, both azimuthal  $wn-1$  and  $wn-2$  asymmetries are investigated in this study. The second set of the experiments (named as LB02 hereafter) is also based on the weak baroclinic vortex but with the center of asymmetries ( $wn-1$  and  $wn-2$ ) placed at  $r_c = r_m, z_c = 5 \text{ km}$ . Experiments LB01 and LB02, thus, allow us to investigate how VRWs propagate in the baroclinic and quasi-barotropic mean flow of the weak baroclinic vortex. The design of experiments HB01 (with the center of asymmetry located at  $r_c = r_m, z_c = 0 \text{ km}$ ) and HB02 (with the center of asymmetry located at  $r_c = r_m, z_c = 5 \text{ km}$ ) is the same as that of LB01 and LB02 but for the strong baroclinic vortex. All initial asymmetries have a radial width of 200 km and vertical width of 20 km. The horizontal structure of initial asymmetry with  $wn-1$  and  $wn-2$  is shown in Fig 5.7. As shown in the figure, the radial width for the positive (negative) perturbation is 100 km, and thus, an entire wave has a radial width of 200 km. Likewise, the vertical width of the prescribed asymmetry is 20 km. Similar to MK97 and MM00, the amplitude of initial asymmetry is set to 60% of the basic-state symmetric vorticity at  $r_m$ . Figure 5.8 shows the radial-height distribution of initial basic-state symmetric vorticity and asymmetric perturbation vorticity. Note that such a construction of initial asymmetry is consistent with that in our theoretical analyses.

#### **5.4 Verification of VRW Propagation**

This section aims to answer two important questions of VRW: If the theoretically predicted VRW does exist in 3D non-hydrostatic WRF simulations? If so, can the simulated VRW propagation by WRF be quantitatively described by the theoretical prediction? To answer these two questions, I carefully examined the wave packets in the WRF simulations.

Fig. 5.9 depicts the time evolution of the real part of Fourier coefficients of relative vorticity ( $\zeta_2$ ) and vertical velocity ( $w_2$ ) for the wn-2 asymmetry at the 1 km altitude in experiment LB01. Since the negative components of Fourier coefficients are merely the mirror of the positive components, for a clear illustration only the positive components of the Fourier coefficients are plotted in the figure. The radius where the center of initial asymmetric vorticity is placed is marked by the triangle. The radially outward propagating wave packets are clearly observed. With the aid of the black dashed lines marked in Fig. 5.9a, the radial group velocity can be estimated, which gives a value of  $\frac{110\text{km}-70\text{km}}{9.5\text{h}-6.5\text{h}} \times 2\pi = 23.3\text{m/s}$  at the reference radius  $r = r_m$ . This estimate is consistent with the theoretically predicted radial group velocity shown in Fig. 4.4a. In addition, the curvatures of the color shades in Fig. 5.9a suggest the existence of stagnation radii for the outward propagating wave packets, since the wave packets slow down due to the increase of radial wavenumber via the vortex shearing effect. The stagnation radius shown in Fig. 5.9a is approximately at  $r=140\text{km}$ , which is also consistent with the WKB prediction shown in Fig. 4.5b. This result suggests that waves excited near the surface in the quasi-barotropic mean flow of the 3D baroclinic vortex closely follow the theoretical prediction of VRW propagation in barotropic vortices by the WKB analyses.

As a comparison, the real part of Fourier coefficients of vertical velocity ( $w_2$ ) for the wn-2 asymmetry is shown in Fig. 5.9b. The wave packets indicated by  $w_2$  continue radiating outward with time in stark contrast to radial propagating feature of  $\zeta_2$ , which is confined in the inner-core region and cannot radiate beyond the stagnation radius. MK97 argued that the dynamics of VRWs that have stagnation radii is distinct from that of freely

propagating gravity–inertia waves. Since VRWs and gravity–inertia waves have their signatures in the vorticity and vertical velocity fields, respectively, it indicates that the wave packets shown in Fig. 5.9a are indeed the VRWs but not gravity–inertia waves.

Fig. 5.10 shows the evolution of  $\zeta_2$  and  $w_2$  at  $z=2.5$  km in experiment LB02 in which the center of initial asymmetric vorticity is placed at  $z=5.0$  km. Unlike the wave propagation in the quasi-barotropic mean flow, the outward propagation of  $\zeta_2$  in the baroclinic mean flow is more confined in the vortex inner-core region, suggesting the suppression of wave radial propagation by the strong baroclinicity. The difference of wave packets between VRWs shown by  $\zeta_2$  and gravity–inertia waves shown by  $w_2$  is more prominent in this case. The VRW group velocity shows a strong dependence on wave radial wavenumber evidenced by the curvature of the wave trajectories. On the other hand, the outward radiating wave packets shown in  $w_2$  are nearly parallel, suggesting that the gravity-inertial waves are nondispersive, i.e. the waves are independent of wave radial wavenumber.

The vertical group velocity is examined in a similar way. Fig. 5.11 shows the time evolution of vertical distribution of  $w_2$  vorticity  $\zeta_2$  in LB02 at the radius  $r=30$ km, where strong wave upward propagation occurs. The curvature of  $\zeta_2$  in the time-height plot implies the decrease of vertical group velocity with time caused by the vortex vertical shearing effect discussed in Chapters 2 and 3. Strong upward propagation can be observed from 9 h to 12 h (indicated by the dashed lines Fig. 5.11). A crude estimate gives the vertical group velocity of  $\frac{7\text{km}-4\text{km}}{12\text{h}-9\text{h}} \times 2\pi = 1.74\text{m/s}$ , which is slightly larger than the theoretical prediction shown in Fig. 4. At about 16h, the upward propagation reaches the stagnation

height. In next section, more evidences are provided to show that the WRF simulated VRW propagation is consistent with our linear theoretical predictions using WKB analyses.

## **5.5 VRW Propagation Features in Baroclinic Vortices**

### **5.5.1 *Propagation of $Wn-2$ Asymmetry in the Quasi-barotropic Regime of a Baroclinic Vortex***

As stated in the introduction, the AB theory from which the VRW propagation theory was derived may still be applied to asymmetries with azimuthal wavenumber  $n>1$  based on MM99's investigation. Here, I'll provide further evidence that the AB approximation works well for  $wn-2$  asymmetry at least for the case investigated in this study. In this section, I'll present the wave propagation of  $wn-2$  asymmetry in the quasi-barotropic regime of a baroclinic vortex in the WRF simulations.

Experiment LB01 was designed to investigate the wave propagation for asymmetries in the quasi-barotropic regime at the surface of a weak baroclinic vortex. Fig. 5.12 shows the radial-height distribution of  $wn-2$  vorticity at different time during the simulation. Examinations show that new waves are excited by the initial asymmetry after the 1<sup>st</sup> h into the simulation in the inner-core region centered at 40 km where the vortex ' $\beta$ ' effect is the strongest as indicated in Fig. 5.5. At the 2<sup>nd</sup> h into the simulation, the amplitude of the newly generated inner-core waves is comparable to that of the initial asymmetry whose amplitude has been largely reduced at the time (Fig.5.12a). The phenomenon that the inner waves can be excited by the initial asymmetry placed in the vicinity of RMW has been reported in many previous studies (e.g., MK97; MM99; Peng et al. 2008, 2014a and 2014b). For the monopole vortex constructed in this study, the vortex ' $\beta$ ' effect decreases

radially outward after it reaches its peak at about 40 km. For this reason, the outer component of the initial asymmetry evolves in the region with relatively weaker vortex ' $\beta$ ' effect, and therefore, wave axisymmetrization at those larger radius is weaker and slower. MK97 argued that because of the weak axisymmetrization at the larger radii, the initially prescribed asymmetries act as the quasi-steady asymmetric forcing to the vortex inner-core region. As a result, the inner-core waves will be continuously excited till the outer disturbances become sufficiently weak. MM99 also pointed out that the deformation of the initial asymmetry will lead to the up-shear tilting of asymmetry inside the center of the initial asymmetry, which supports the excitation of wave activities there. Since the growth of the inner waves must be at the expense of the mean flow, the vortex will be temporarily weaker because of the wave excitation. However, I will show in Chapter 6 the outward propagation of waves can effectively shift the up-shear tilting of asymmetries to down-shear tilting, which allows the waves energy to be axisymmetrized into the mean flow. The detailed processes of wave-mean-flow interaction that leads to the vortex intensification will be discussed shortly.

As shown in Fig. 5.12, it is apparent that the radial wavenumber increases with time as the initial prescribed and the induced asymmetries propagate radially outward. This is consistent with the WKB analysis that the vortex radial shearing effect causes the increase of radial wavenumber. Also note that the increase of radial wavenumber inside the RMW appears to be larger than that outside the RMW. This is most likely due to the fact that the vortex ' $\beta$ ' effect is stronger inside of the RMW. As indicated by the theoretical analyses, the increase of radial wavenumber leads to the cease of the outward propagation at the stagnation radius. MK97 pointed out that the existence of stagnation radius is an important

feature that distinguishes VRW from the gravity wave. The cease of radial propagation of the wave packets is clearly shown in Fig. 5.12. At the 12<sup>th</sup> h, the inner asymmetries have migrated to the radius about  $r=90\text{km}$  and the initial asymmetry has propagated to the radius  $r=130\text{km}$  (Fig. 5.12d). Since the initial asymmetry is placed at the RMW (75km) and the inner waves are excited at 40 km, the net distance travelled by both wave packets is approximately 50-55 km. This radial distance is consistent with the theoretical prediction of  $wn-2$  asymmetry by the WKB analysis (Fig. 4.5).

It is also worthy to note that no apparent wave vertical propagation is observed in this experiment. This is consistent with the theoretical analyses in Chapter 4 that the asymmetries excited near the surface cannot effectively propagate upward, suggesting that the VRW propagation in the quasi-barotropic regime of a baroclinic vortex basically follows the theoretical prediction of VRWs in barotropic vortices. In summary, except for the excitation of waves in the vortex inner-core region, the simulated wave packets in experiment LB01 possess the basic VRW features predicted by the linear WKB analyses presented in Chapter 4.

### ***5.5.2 Propagation of $Wn-2$ Asymmetry in the Baroclinic Regime of a Baroclinic Vortex***

The basic-state vortex of experiment LB02 is exactly the same as that of LB01, but the center of the initial asymmetry is placed in the middle troposphere ( $z=5\text{km}$ ) at the RMW where the mean flow falls in the baroclinic regime of the constructed vortex. Thus, this experiment along with the LB01 allows us to investigate how baroclinicity affects the VRW propagation in a weak baroclinic vortex. Figure 5.13 shows the radial-height structure of  $wn-2$  vorticity at different time during the simulation. Again, the inner waves are excited

at the radius near 40 km by the initial asymmetry in the early time of the simulation. However, unlike LB01, the height of wave excitation extends to the low troposphere and the waves show a significant upward propagation. This is consistent with the theoretical analysis presented in Chapter 4 (Fig. 4.14) that the waves excited at the low to middle troposphere in the inner-core region can most effectively propagate upward. In addition to the excitation of inner waves, the initially prescribed asymmetry also propagates upward. It is apparent that the vertical wavenumber of both the primary asymmetry and inner excited waves increases as the wave packets propagate upward. This is an important feature of VRW in baroclinic vortices that the vortex vertical shearing causes the vertical wavenumber to increase according to our theoretical derivation.

Figure 5.13 also shows that the vertical propagation of inner and outer waves is different. The former travels a larger vertical distance than the latter. This may be attributed to the fact that the inner waves propagate under the stronger vortex ' $\beta$ ' effect. Despite the nonlinear effect and other complications, the vertical distance traveled by the wave packets appears to be consistent with the linear theoretical prediction shown in Fig. 4.14. The comparison between Figs. 5.12 and 5.13 shows that the wave packets in the baroclinic regime are confined more in the inner-core region than those in the quasi-barotropic regime. This is also consistent with the theoretical conclusion that the promotion of wave vertical propagation must be accompanied by the suppression of wave radial propagation because of the constraint of the 'critical' surface.

To further illustrate the difference of wave propagation in the quasi-barotropic and baroclinic regimes of a baroclinic vortex, Fig. 5.14 compares the horizontal plane view of the positive Fourier coefficients of  $wn-2$  vorticity at the 12<sup>th</sup> h in LB01 and LB02, where

for a clear illustration the negative Fourier coefficients have been removed as they are merely the axisymmetric mirror of the positive coefficients. In the quasi-barotropic regime, the propagation of inner excited waves and outer initially prescribed waves is clearly separated. The inner waves are highly sheared by the mean flow and confined inside the radius of  $r=90\text{km}$ , whereas the outer waves can propagate up to the radius of  $r=150\text{km}$  (Fig. 5.14a). The wave packets in the baroclinic regime (Fig. 5.14b) show a quite different feature. The increase of radial wavenumber in LB02 is much slower than that in the quasi-barotropic regime of LB01. As I showed previously, the wave packets in the baroclinic regime are largely sheared in the vertical. As a result, the inner wave propagation ceases at the radius of  $r=70\text{km}$ , while the outer waves can only reach the maximum radius of  $r=120\text{km}$ .

To highlight the differences of VRW propagation in strong and weak baroclinic vortices, Figure 5.15 compares the radial-height structure of azimuthal-mean  $wn-2$  vorticity at the 6<sup>th</sup> h into the simulation in the four experiments, LB01, LB02, HB01 and HB02. The difference in wave propagation in experiments LB01 and HB01 is only marginal. The waves are basically trapped in the low layer with similar radial propagation. Notable difference in wave propagation is shown in LB02 and HB02. The vertical propagation of VRWs is more prominent in the strong baroclinic vortex than that in the weak baroclinic vortex. In the meantime, the wave radial propagation is substantially suppressed in the strong baroclinic vortex. I'll show in Chapter 6 that these VRW propagation features due to different baroclinicity have important bearings on the wave-me-flow interaction and vortex intensification.

### 5.5.3 *Wave Propagation of Wn-1 Asymmetries*

In Chapter 4, the difference in wave propagation between wn-1 and wn-2 asymmetries has been analyzed based on the theoretical derivations. It remains to be unclear if these differences obtained in the linear analyses are physically robust. To answer this question, the same experiments as LB01, LB02, and HB01, an HB02 but with the wn-2 asymmetry replaced by wn-1 asymmetry have been performed. The results from LB01 and LB02 are presented in this section. As stated previously, wn-1 asymmetry tends to induce a fast-growing mode perturbation in the inner-core region (MK97, MM00, and Peng et al. 2008). This ‘pseudomode’ did not appear to affect the growth of the normal modes according to MK97’s 2D non-divergent simulations. I’ll show shortly, however, that this ‘pseudomode’ appears to have a complication on the VRW propagation in the WRF simulations.

The wave propagation of wn-1 asymmetry in the quasi-barotropic regime of the weak baroclinic vortex at different time is shown in Fig. 5.16. Compared with the wn-2 asymmetries, the increase of radial wavenumber for wn-1 asymmetries is slower. This result is consistent with the theoretical derivation (Eq. 2.21) that the rate of radial wavenumber increase is proportional to the azimuthal wavenumber. As the figure indicated, the wn-1 wave packet can propagate farther in radial direction. The maximum radius that the waves can reach is about 180 km (compared with  $r=150\text{km}$  for wn-2). The results of LB01 with wn-1 and wn-2 asymmetries basically confirmed the WKB’s prediction of VRWs in barotropic vortices that higher wavenumber asymmetries are more affected by the vortex radial shearing effect, and thus, their radial propagation is more confined, leading to a shorter stagnation radius. A key difference of wave propagation between wn-

1 and  $w_n-2$  asymmetries is that the inner waves excited by the  $w_n-1$  asymmetry near the surface are not totally trapped in the low layer even in the quasi-barotropic regime. As indicated in Fig. 5.16, wave activities are seen in the middle troposphere, which is not expected according to the theoretical analyses that wave excited near the surface cannot effectively propagate upward. I suspect that the vertical propagation of  $w_n-1$  asymmetry in the quasi-barotropic regime may be caused by the fast growing of the ‘pseudomode’.

The wave propagation of  $w_n-1$  asymmetry in the baroclinic mean flow is shown in Fig. 5.17. Intense vertical propagation is seen in the simulation. The stagnation height for  $w_n-1$  is about  $z=13\text{km}$ , which is much higher than that for  $w_n-2$ , and the radial propagation is, therefore, confined more to the inner core region of the vortex consistent with the theoretical analysis. At the 20<sup>th</sup> h into the simulation, it appears that the wave propagation can be divided into two pathways. One is dominated by the vertical propagation and barely can propagate beyond the RMW, and the other shows strong radial propagation but is trapped in the low layer. It remains to be a question if such a complication feature of  $w_n-1$  wave packets is caused by the nonlinear effect or by the ‘pseudomode’. Further investigation is needed.

The horizontal wave structures of  $w_n-1$  asymmetry in quasi-barotropic and baroclinic regimes are shown in Fig. 5.18. Similar to  $w_n-2$  asymmetries (Fig. 5.14), the inner waves are more subjected to the vortex “ $\beta$ ” effect. As a result, a much faster increase of radial wavenumber for inner waves is seen than that of outer waves. In the baroclinic regime, the vortex radial shearing effect is weaker, and thus, the increase of radial wavenumber is slower than that in the quasi-barotropic regime. But because of the strong

baroclinicity, which enhances the wave vertical propagation, the wave radial propagation is suppressed in LB02.

## 5.6 Summary

The nonlinear and nonhydrostatic WRF simulations are performed to investigate the structures and evolution of asymmetric features in 3D baroclinic vortices. Two hurricane-strength vortices with strong and weak baroclinicity are constructed. Based on the strength of basic-state baroclinicity, it is shown that the constructed 3D baroclinic vortices may be divided into a quasi-barotropic regime near the surface and a baroclinic regime in the low to middle troposphere. To investigate the impact of baroclinicity on VRW propagation, eight numerical experiments are designed in which  $w_{n-1}$  and  $w_{n-2}$  asymmetries are introduced in the quasi-barotropic regime and baroclinic regime in the strong and weak baroclinic vortices. The main conclusions are summarized as follows.

- 1) Fourier decomposition of the simulated vorticity and vertical velocity fields indicates that the wave packets shown in the vorticity field possesses the basic features of VWRs including the increase of radial and vertical wavenumber as waves propagate radially outward and upward and the existence of wave stagnation radii and heights. These waves are fundamentally different from the gravity–inertia waves.
- 2) In the experiments in which initial asymmetries are placed near the surface, the wave propagation in 3D baroclinic vortices has the similar characteristics to that in MK97's 2D and MM00's 3D barotropic vortices. Significant radially outward propagating wave packets are found in both strong and weak baroclinic vortices, which can be attributed to the quasi-barotropic mean flow near the surface in both vortices. Both the initial wave

packet and the waves excited inside the RMW where the vortex ' $\beta$ ' effect is the maximum can reach the stagnation radii close to the theoretical predictions. The wn-2 asymmetry is found to be trapped in the low layer. However, due to the effect of fast growing pseudo-mode, the wn-1 asymmetry shows a slightly upward propagation.

3) In the experiments in which the initial asymmetries are placed at  $z=5$  km, the wave propagation shows different characteristics from that in the quasi-barotropic mean flow. The waves can effectively propagate upward but with their radial propagation confined in the inner-core region. The wave excited at radius where the vortex ' $\beta$ ' effect is the maximum can propagate to reach the stagnation height predicted by the theoretical analyses.

4) The simulated radial and vertical propagation of wn-2 asymmetry is remarkably similar to the theoretical prediction obtained by the linear WKB analyses within the AB model framework. This result confirms MM99's conclusion that the AB approximation can be extended at least to wn-2 asymmetry despite the large local Rossby number indicated by the scaling analysis.

5) A key difference in wave propagation between wn-1 and wn-2 asymmetries is that the increase of radial and vertical wavenumber with time is much faster in the latter, causing waves to be more confined in the region where waves are excited. This result is consistent with the theoretical analysis that only low wavenumber asymmetries can have meaningful radial and vertical propagation.

weak baroclinic vortex ( $L = 7500$ )

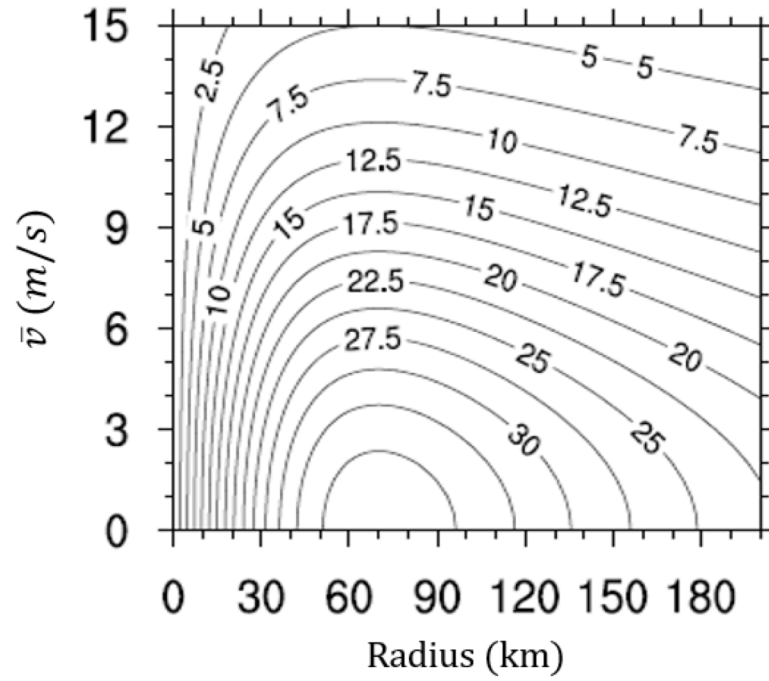


Fig. 5.1: Radius-height distribution of initial azimuthal velocity for the hurricane-strength vortex with weak baroclinicity.

strong baroclinic vortex ( $L = 5000$ )

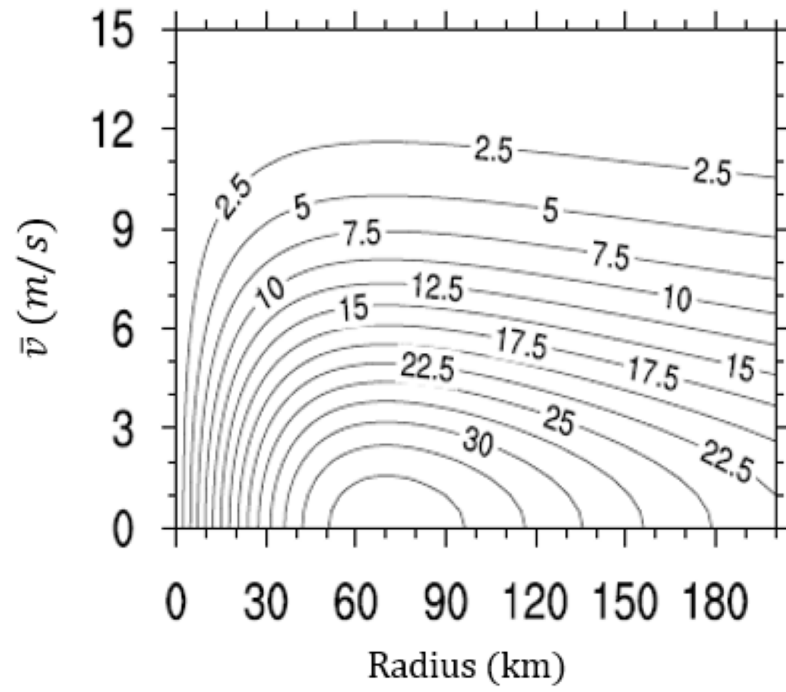


Fig. 5.2: Radius-height distribution of initial azimuthal velocity for the hurricane-strength vortex with strong baroclinicity.

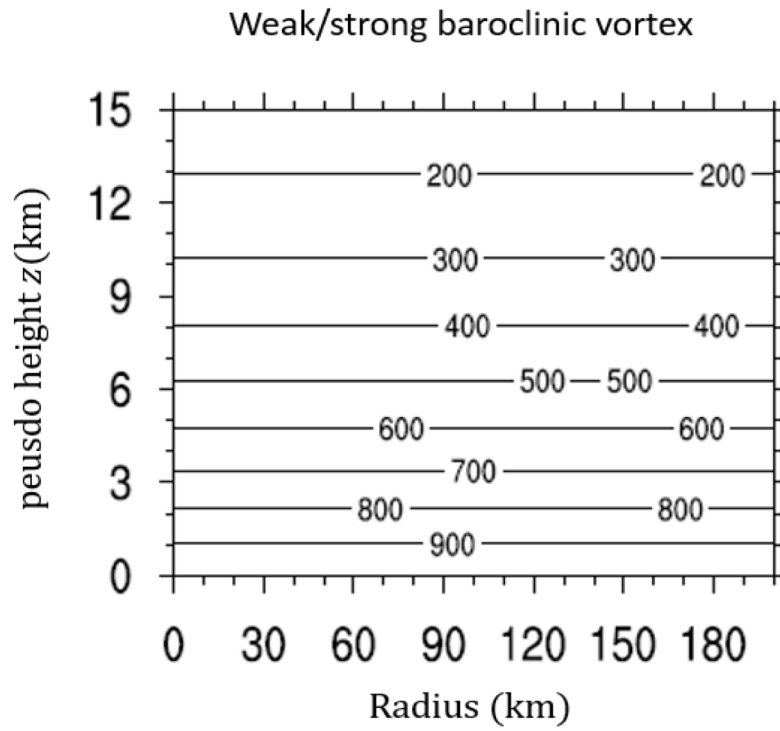


Fig. 5.3: Radius-height distribution of initial mean pressure (mb), which is the same for both weak and strong baroclinic vortices.

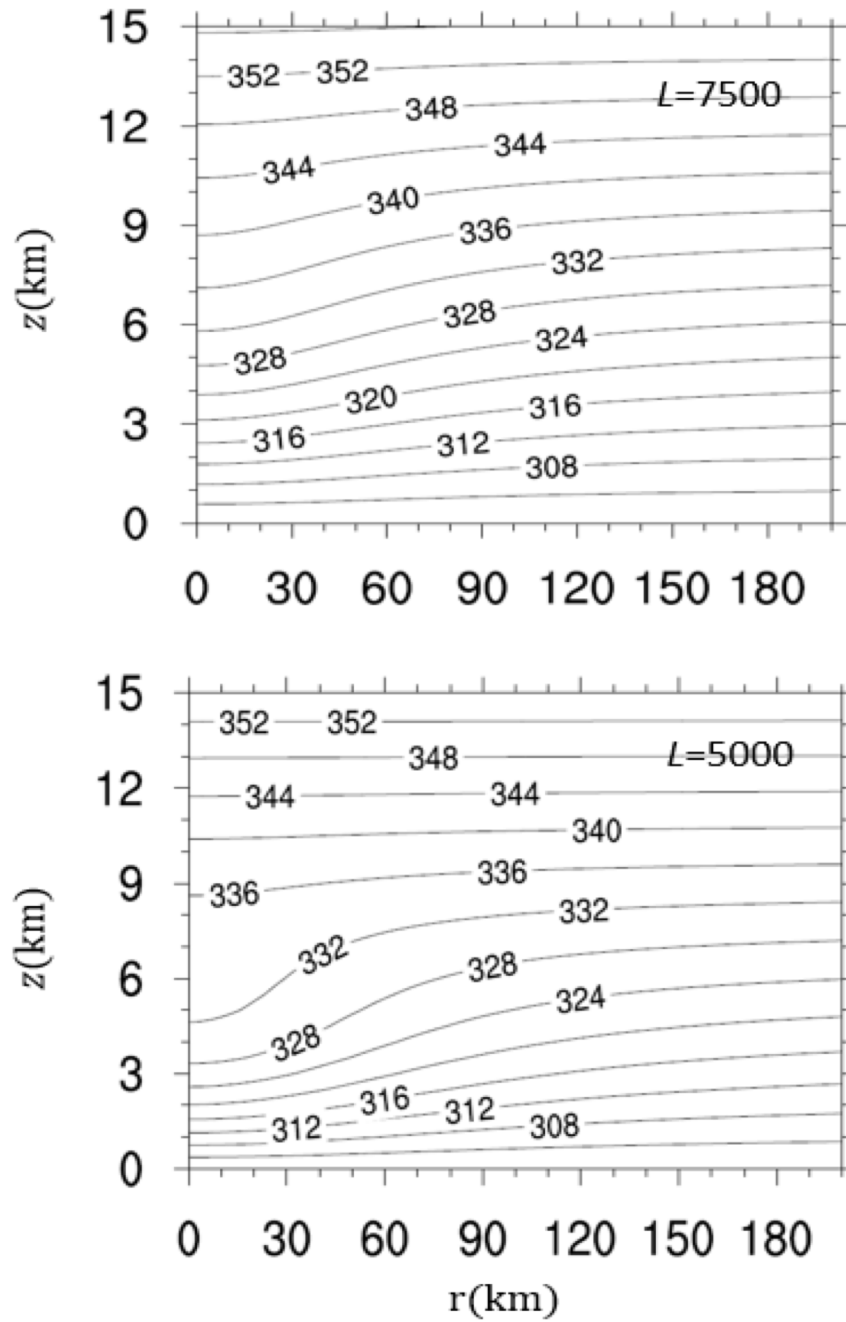


Fig. 5.4: Radius-height distribution of initial mean potential temperature (K) for both weak and strong baroclinic vortices.

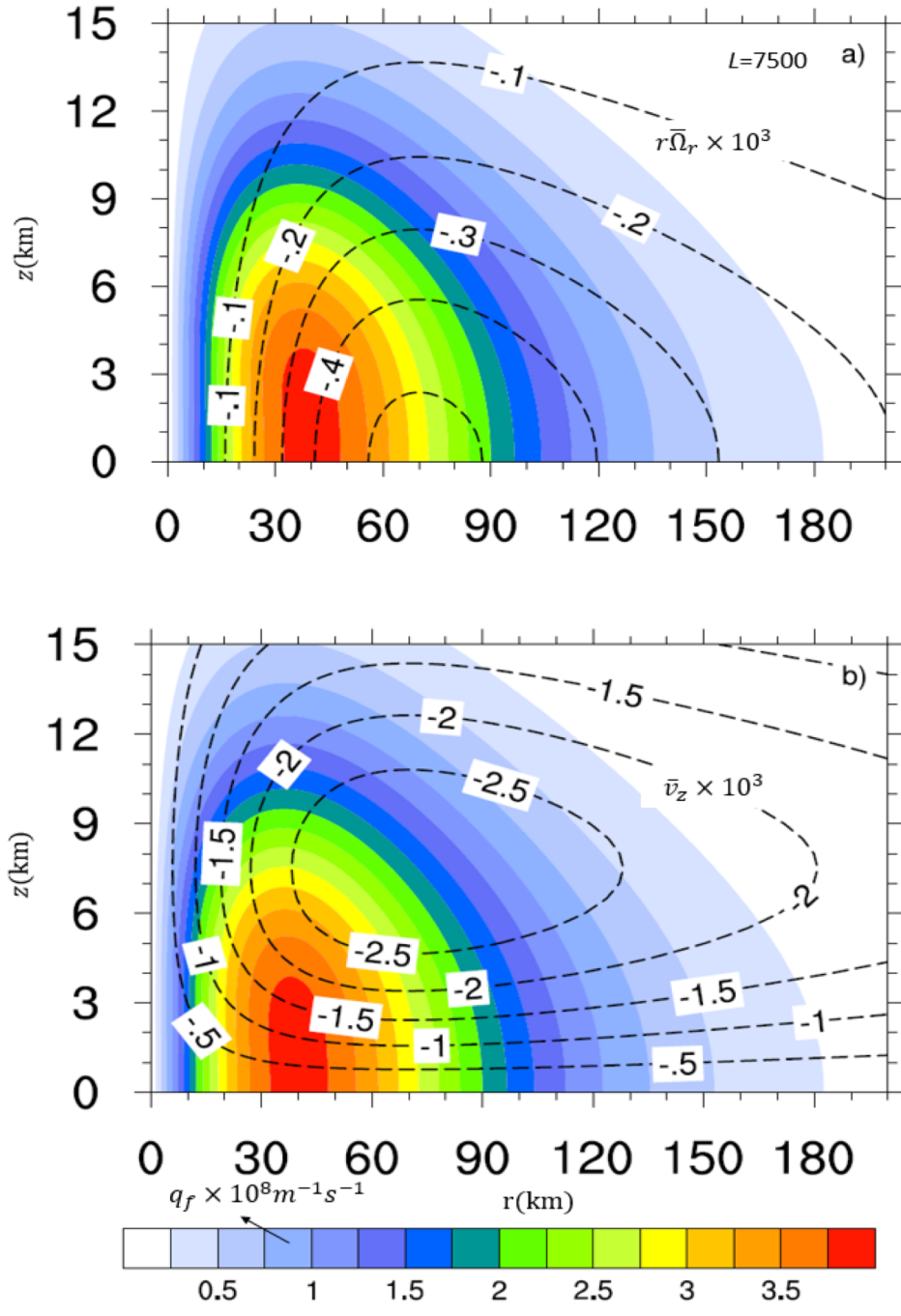


Fig. 5.5: a) Initial radius-height distribution of the vortex  $\beta$  effect parameter  $q_f$  (color shades; scaled by  $10^{-8}m^{-1}s^{-1}$ ) and vortex radial shear  $r\bar{\Omega}_r$  (dashed lines; scaled by  $10^{-3}m^{-1}s^{-1}$ ) of the weak baroclinic vortex; b) is the same as a) except that the dashed lines indicates the vortex vertical shear  $\bar{v}_z$ .

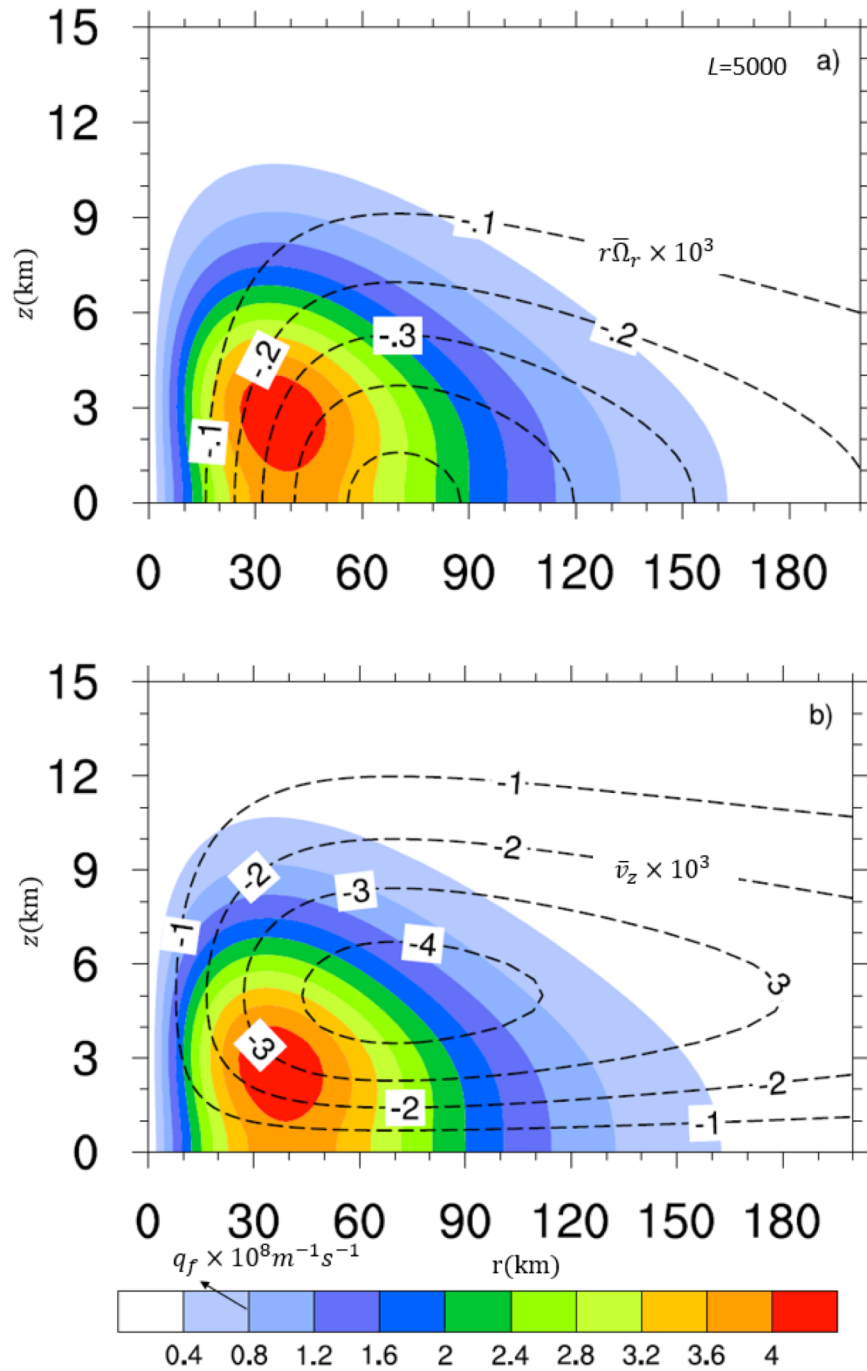


Fig. 5.6: the same as Fig 5.5 but for the strong baroclinic vortex.

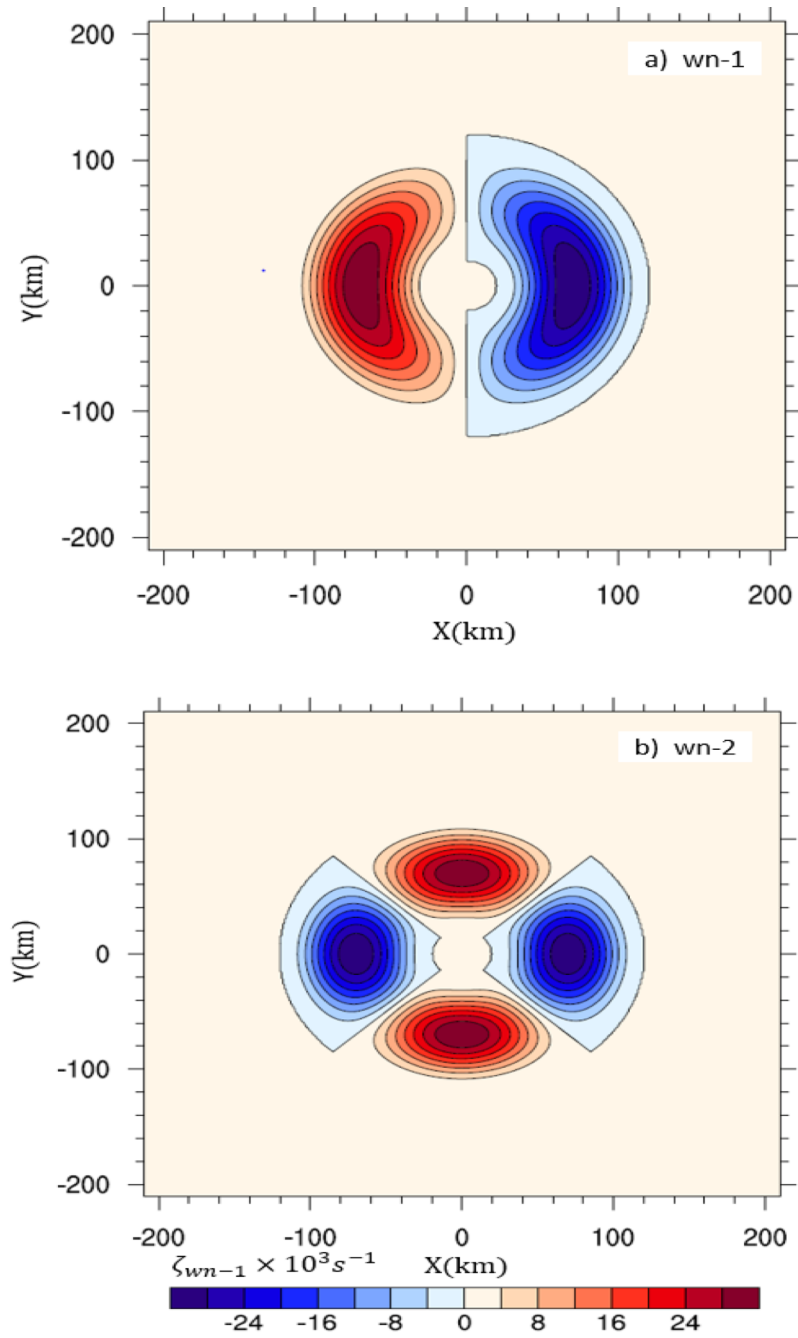


Fig. 5.7: Horizontal structure of initial asymmetric vorticity for a) azimuthal wavenumber one (wn-1) and b) azimuthal wavenumber two (wn-2) at the height where the asymmetry amplitude is the maximum (i.e.,  $z=0\text{km}$  for LB01 and HB01;  $z=5\text{km}$  for LB02 and HB02).

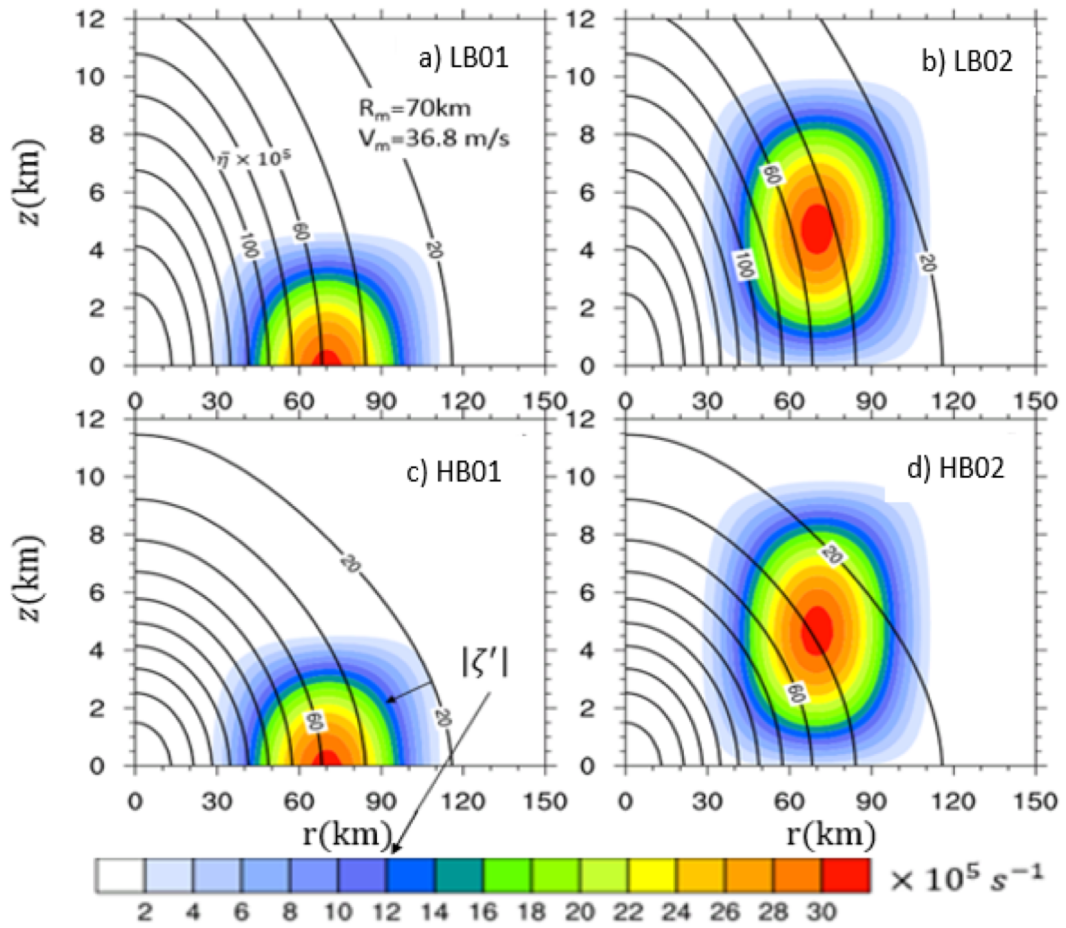


Fig. 5.8: Radius-height distribution of initial basic-state symmetric vorticity (solid lines) and asymmetric perturbation vorticity (color shades) for (a) HB01, (b) HB02, (c) LB01, and (d) LB02. Vorticity has been multiplied by a factor of  $10^5$ .

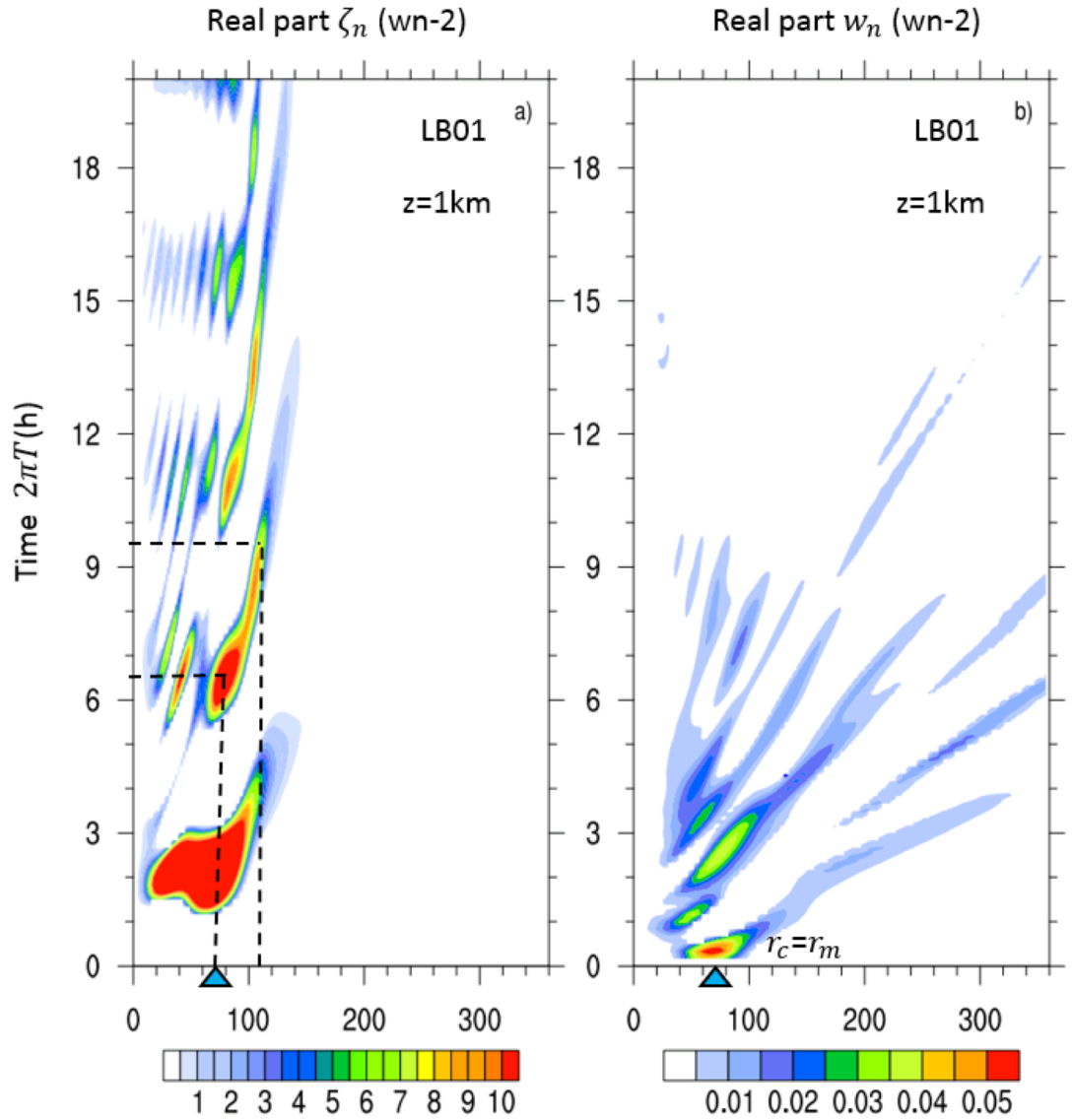


Fig. 5.9: Time–radius Hovmoller plots of the real part of the Fourier coefficients of (a) relative vorticity and (b) vertical velocity at 1 km altitude for  $w_n-2$  asymmetry in experiment LB01. Since the negative components of Fourier coefficients are merely the mirror of the positive components, for a clear illustration only positive components of Fourier coefficients are plotted. Triangle marks the center of the initial asymmetry,  $r_c = r_m$ . Dashed lines indicate the outward propagation of VRW packets.

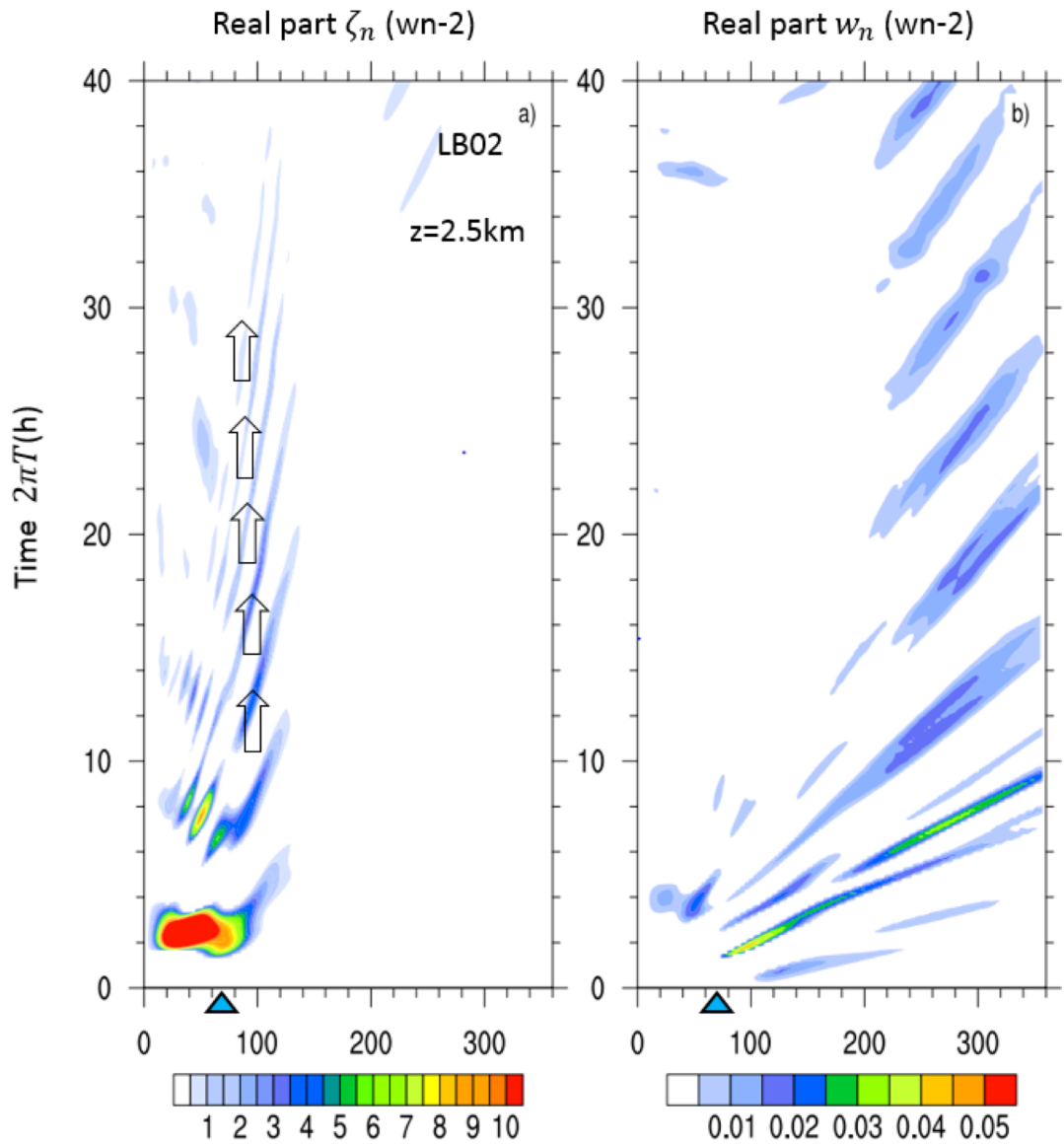


Fig. 5.10: The same as Fig 5.9 but for the wn-2 asymmetry at  $z=2.5\text{km}$  in experiment LB02. The thin arrow in (a) indicates the upward propagation of wave packets.

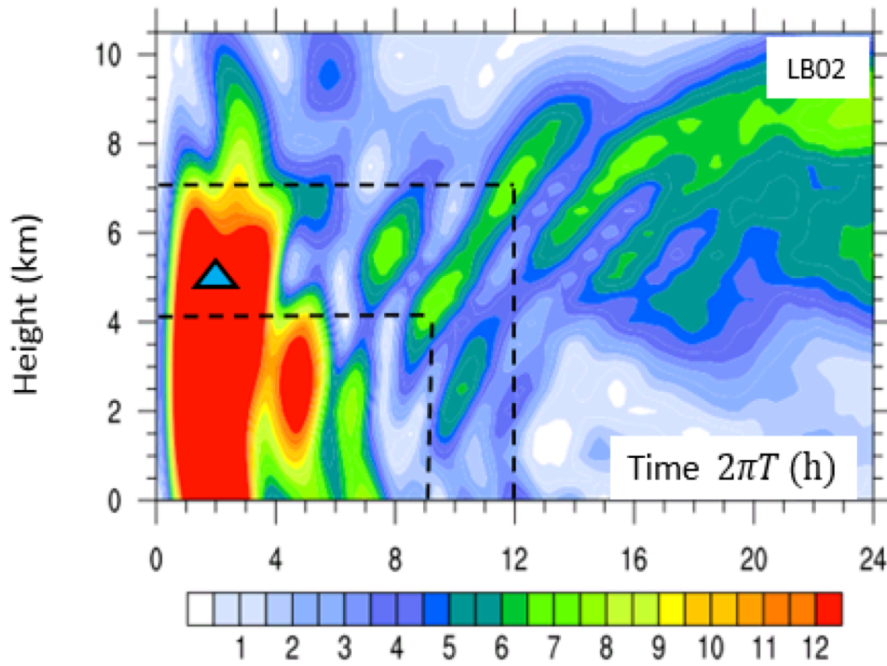


Fig. 5.11: Height-time plots of  $wn-2$  vorticity at the radius of 30 km in experiment LB02. Triangle marks the height where the center of initial asymmetry is placed (i.e.,  $z_c = 5$ km).

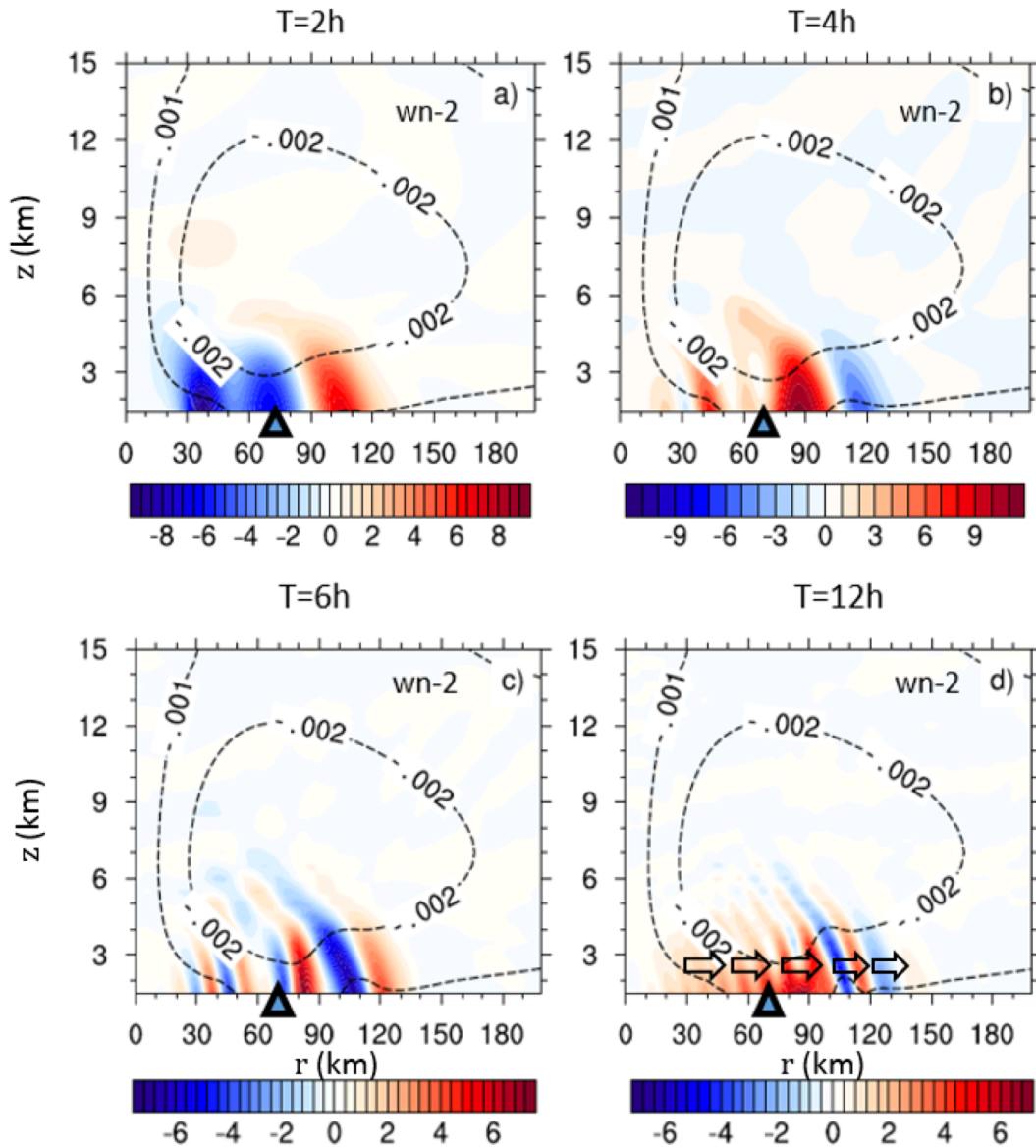


Fig. 5.12: Radial-height distribution of  $wn-2$  vorticity (color shades) and vertical gradient of azimuthal-mean tangential wind (dashed contours) after (a) 4h, (b) 6h, (c) 12h and (d) 20h from experiment LB01. Vorticity ( $s^{-1}$ ) has been multiplied by a factor of  $10^5$ . Solid horizontal arrows in (d) indicate the radial propagation of wave packets in quasi-barotropic condition. Triangle marks the radius where the center of initial asymmetry is placed.

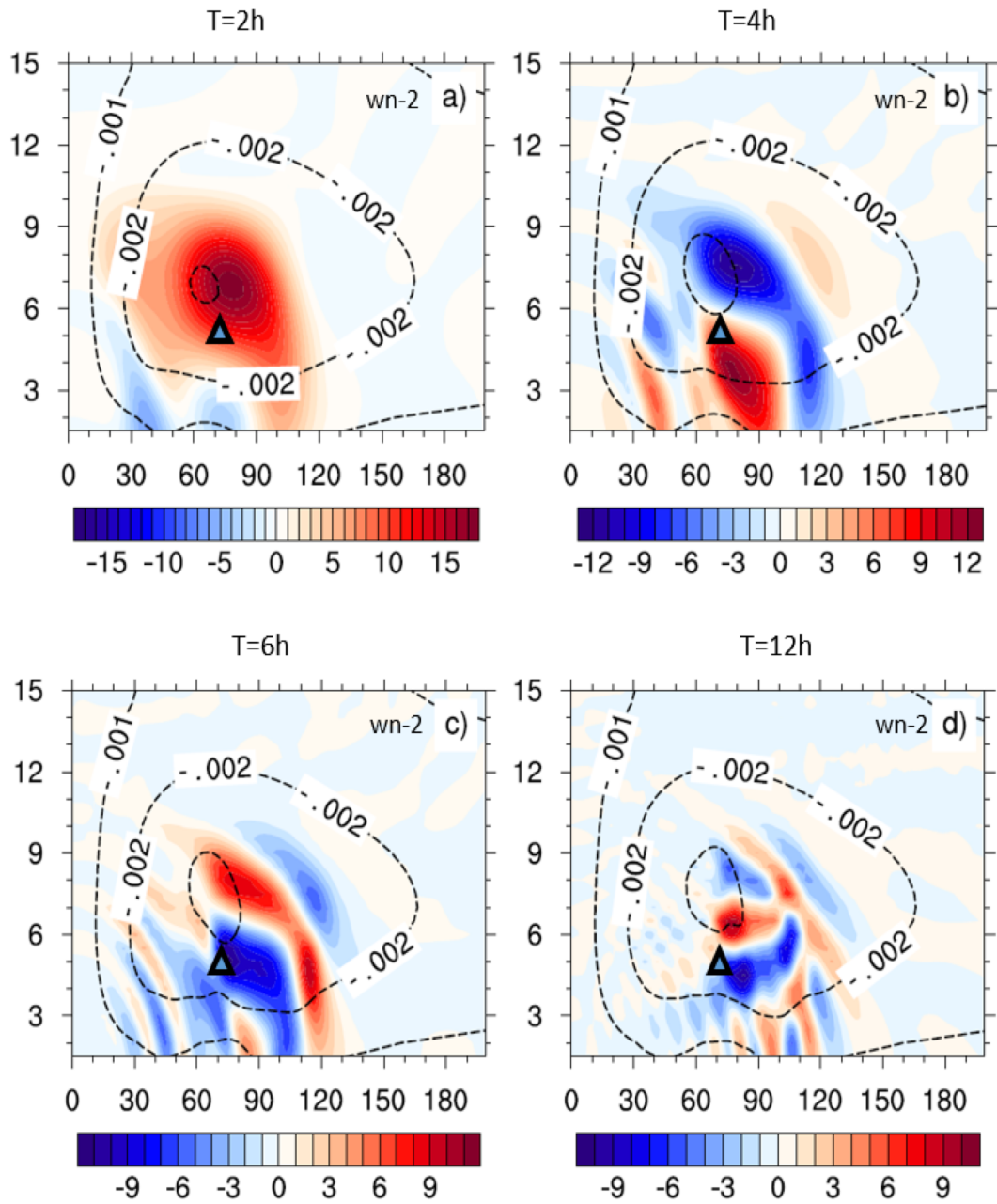


Fig. 5.13: The same as Fig 5.12 but for wn-2 asymmetry in experiment LB02 in which the center of initial asymmetry is placed at  $z=5.0$  km.

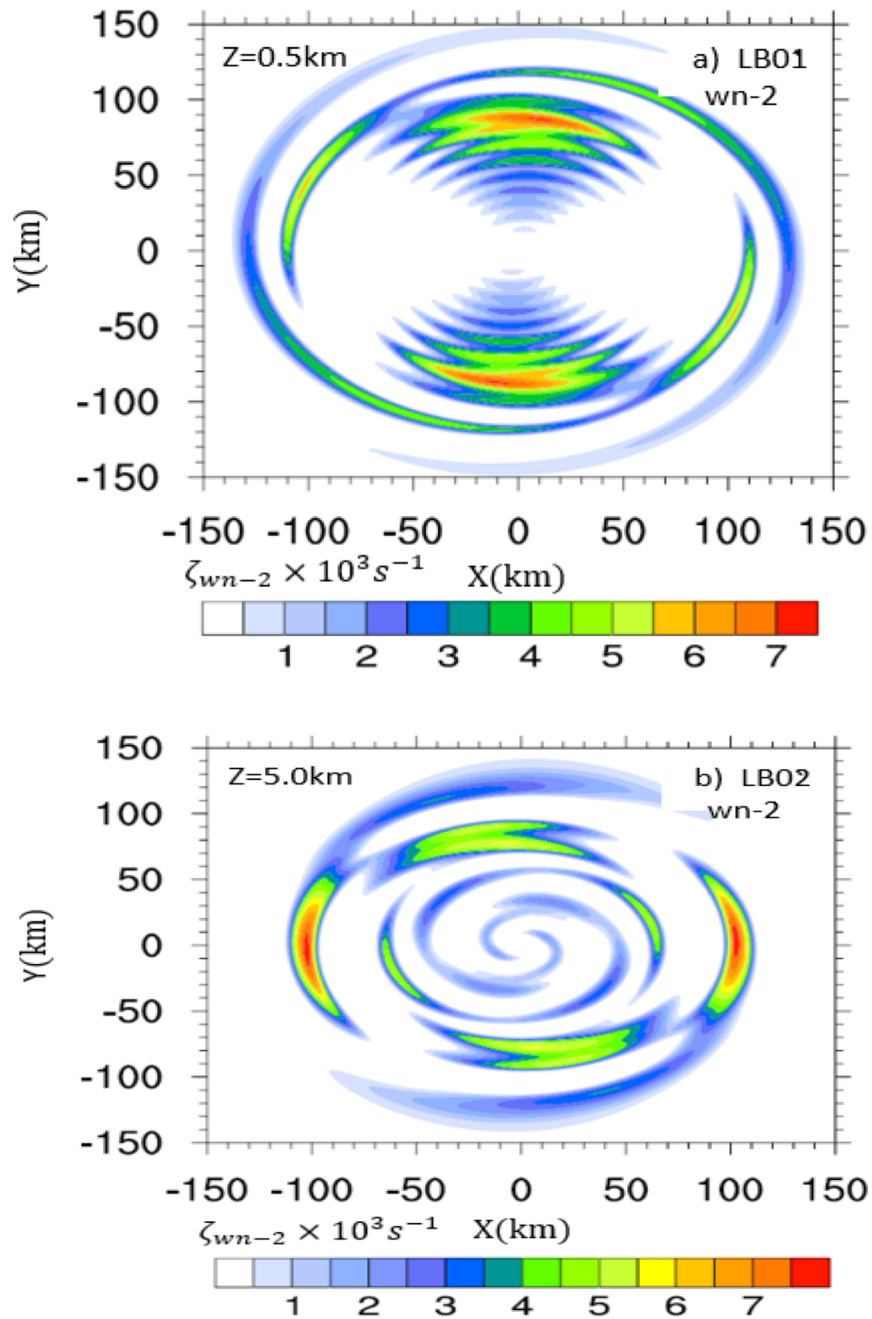


Fig. 5.14: (a) Horizontal plane view of positive Fourier coefficients of  $w_{n-2}$  vorticity at  $z=0.5$  km at 20 h in experiment LB01. (b): The same as (a) but for  $w_{n-2}$  asymmetry at  $z=5$  km at 20 h in experiment LB02. Vorticity ( $s^{-1}$ ) has been multiplied by a factor of  $10^5$ . Note that the negative Fourier coefficients show the same structure but are  $90^\circ$  off phase.

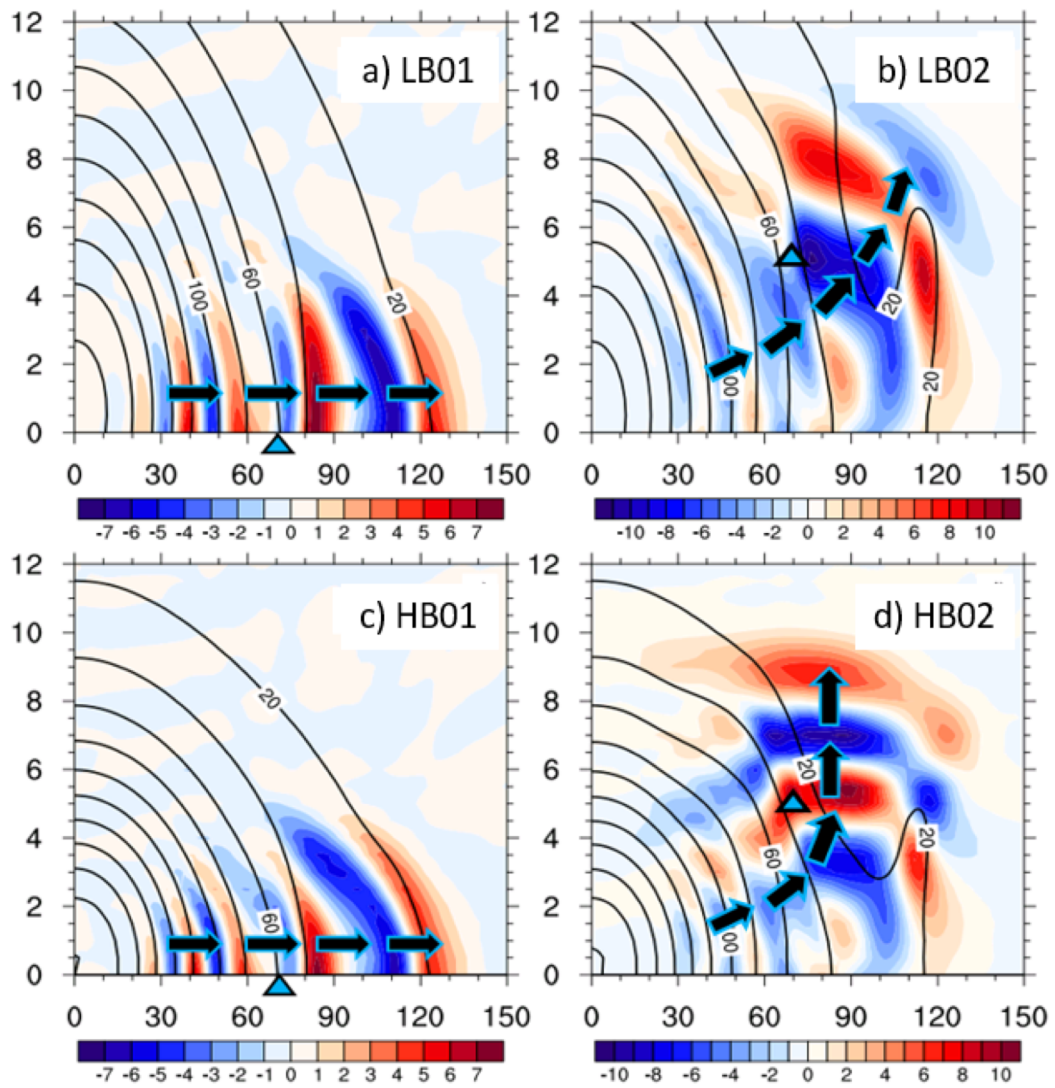


Fig. 5.15: Radial-height distribution of basic-state vorticity (black contours) and  $wn-2$  asymmetric vorticity (color shades) at 6h for experiments (a): LB01, (b): LB02, (c): HB01, and (d): HB02. Vorticity ( $s^{-1}$ ) has been multiplied by a factor of  $10^5$ . Solid arrows in each panel indicate the propagation of wave packets.

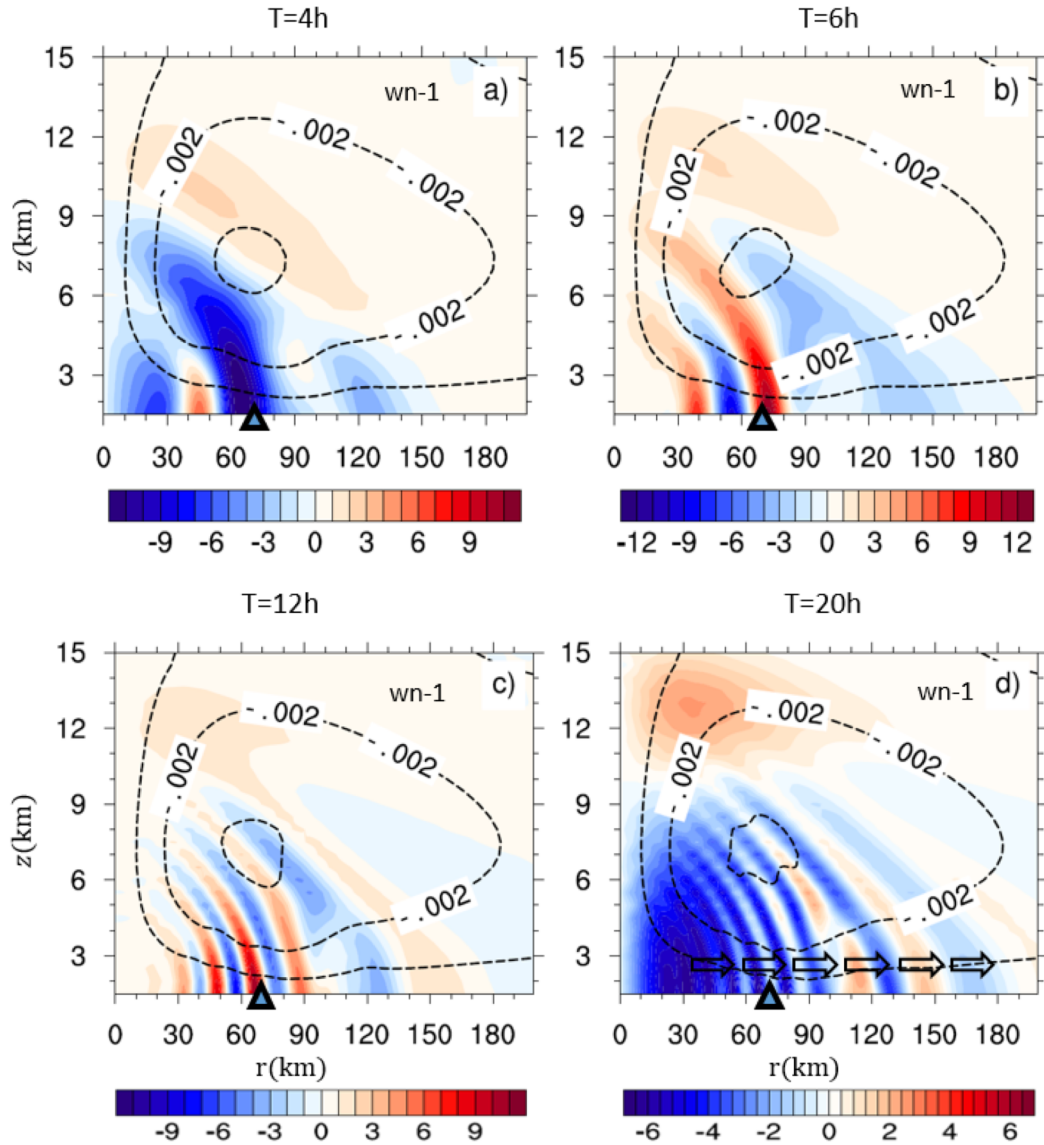


Fig. 5.16: Radial-height distribution of wn-1 vorticity (color shades) and vertical gradient of azimuthal-mean tangential wind (dashed contours) after (a): 4h, (b): 6h, (c): 12h, and (d): 20h from experiment LB01. Vorticity ( $s^{-1}$ ) has been multiplied by a factor of  $10^5$ . Solid horizontal arrows in (d) indicate the radial propagation of wave packets in quasi-barotropic condition. Triangle marks the radius where the center of initial asymmetry is placed.

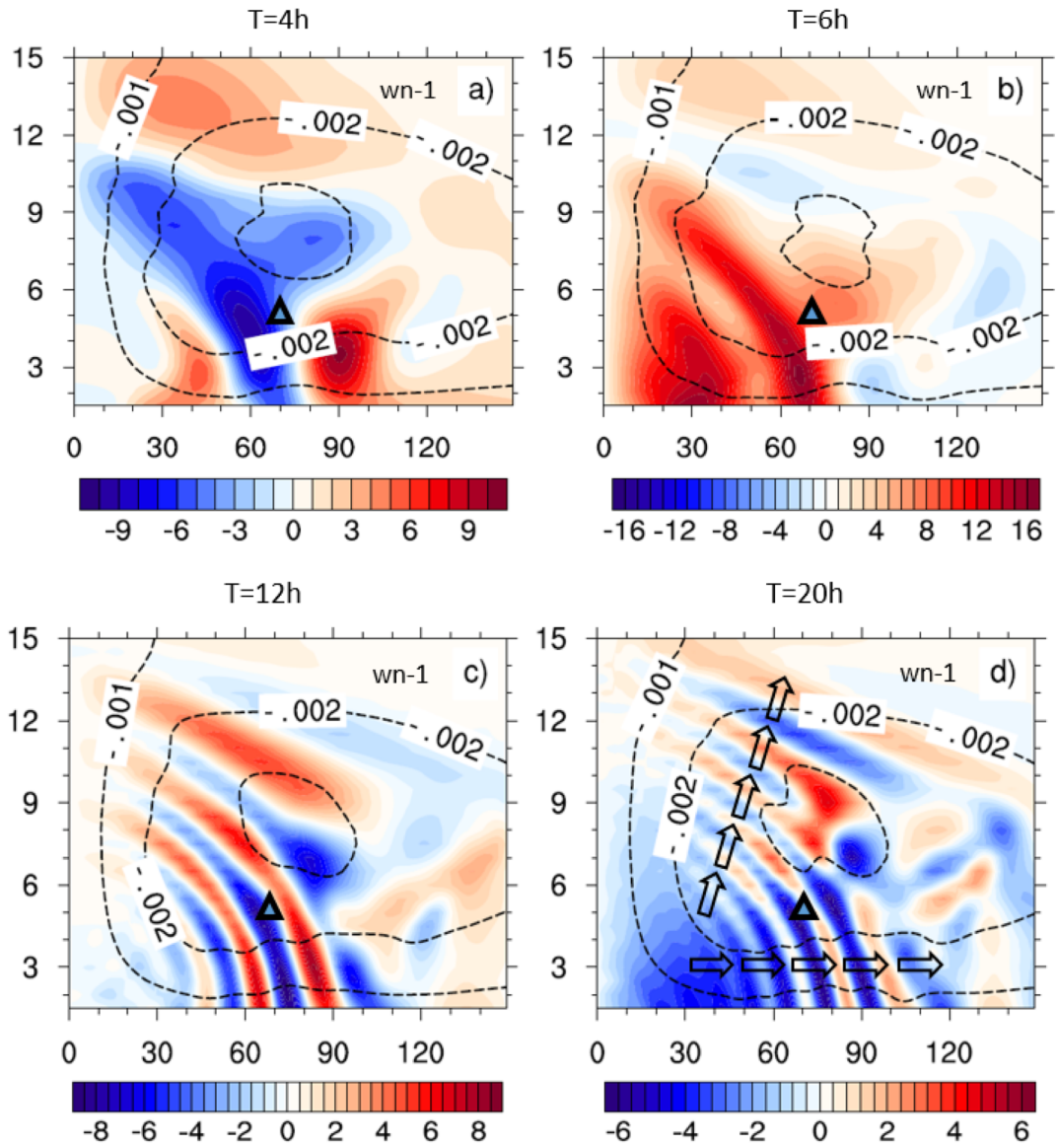


Fig. 5.17: The same as Fig 5.16 but for  $w_{n-1}$  asymmetry in experiment LB02 in which the center of initial asymmetry is placed at  $z=5.0\text{km}$ .

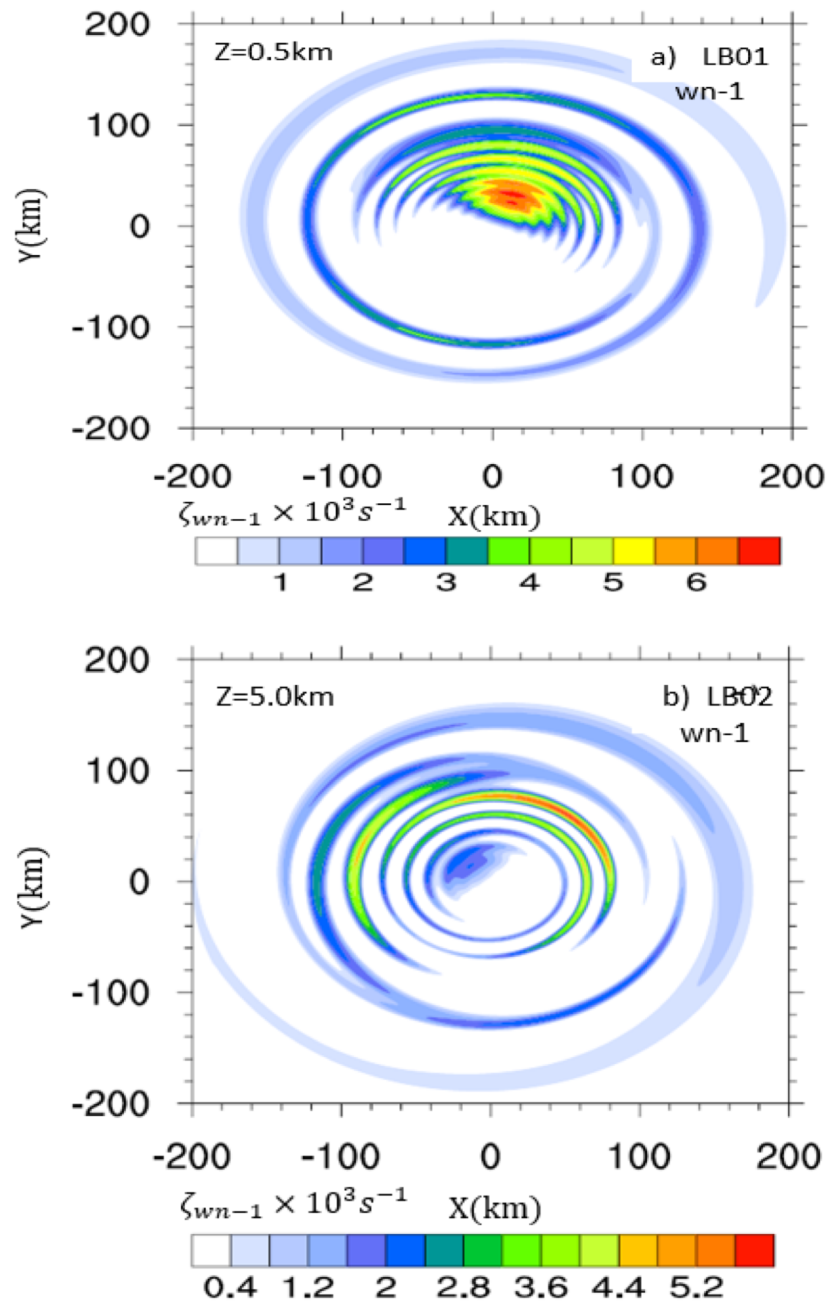


Fig. 5.18: (a) Horizontal plane view of positive Fourier coefficients of  $w_n-1$  vorticity at  $z=0.5$  km at 20 h in experiment LB01. (b): The same as (a) but for  $w_n-1$  asymmetry at  $z=5$  km at 20 h in experiment LB02. Vorticity ( $\text{s}^{-1}$ ) has been multiplied by a factor of  $10^5$ . Note that the negative Fourier coefficients are the axisymmetric mirror of positive Fourier coefficients.

## Chapter 6: WRF Simulation of VRW Propagation in Baroclinic TC-like Vortices. Part II: Wave-Mean-Flow Interaction

### 6.1 Introduction

It has long been recognized that energy can be transferred upscale from the asymmetric disturbance into the mean flow through the eddy momentum flux. This process is known as axisymmetrization and has been shown to play an important role in TC vortex structural change and intensification. VRW theory provides an excellent framework for understanding the axisymmetrization process from the wave-mean-flow interaction perspective. In this chapter, the impact of baroclinicity on wave-mean-flow interaction will be discussed in terms of the change in mean tangential wind of a vortex associated with various processes including the wave activities using the numerical data from the WRF simulations presented in Chapter 5.

### 6.2 Budget Equation of Mean Tangential Wind

A straightforward way to understand the internal mechanisms of TC vortex intensification is to examine the individual contributions of various processes to the net change in tangential winds. In this regard, a detailed budget analysis of mean tangential wind tendency equation is useful. The inviscid azimuthal momentum equation in a cylindrical pseudo height coordinate on an  $f$  plane can be represented as,

$$\frac{\partial v}{\partial t} = -u \frac{\partial v}{\partial r} - v \frac{\partial v}{r \partial \lambda} - w \frac{\partial v}{\partial z} - u \frac{v}{r} - fu - \frac{\partial \phi}{r \partial \lambda}, \quad (6.1)$$

where the meaning of symbols used in the equation is same as that in previous chapters. All variables can be decomposed into the azimuthal mean and the deviations from the mean in the form of,

$$u(r, \lambda, z, t) = \bar{u}(r, z, t) + u'(r, \lambda, z, t), \quad (6.2)$$

$$v(r, \lambda, z, t) = \bar{v}(r, z, t) + v'(r, \lambda, z, t), \quad (6.3)$$

$$w(r, \lambda, z, t) = \bar{w}(r, z, t) + w'(r, \lambda, z, t), \quad (6.4)$$

$$\phi(r, \lambda, z, t) = \bar{\phi}(r, z, t) + \phi'(r, \lambda, z, t). \quad (6.5)$$

Substituting Eqs. 6.2-6.5 into Eq. 6.1, it yields,

$$\begin{aligned} \frac{\partial(\bar{v} + v')}{\partial t} = & -(\bar{u} + u') \frac{\partial(\bar{v} + v')}{\partial r} - (\bar{v} + v') \frac{\partial v'}{r \partial \lambda} - (\bar{w} + w') \frac{\partial(\bar{v} + v')}{\partial z}, \\ & -(\bar{u} + u') \frac{(\bar{v} + v')}{r} - f(\bar{u} + u') - \frac{\partial \phi'}{r \partial \lambda}. \end{aligned} \quad (6.6)$$

Taking the azimuthal-mean of Eq. 6.6, the azimuthal-mean tangential wind tendency equation can be obtained,

$$\frac{\partial \bar{v}}{\partial t} = -\bar{u} \bar{\eta} - \bar{w} \frac{\partial \bar{v}}{\partial z} - \overline{u' \eta'} - \overline{v' \frac{\partial v'}{\partial \lambda}} - \overline{w' \frac{\partial v'}{\partial z}}, \quad (6.7)$$

where  $\bar{\eta} = f + \frac{\bar{v}}{r} + \frac{\partial \bar{v}}{\partial r}$  is the absolute vorticity. An equivalent azimuthal-mean tangential wind tendency equation in the flux form may be further obtained by combining the continuity equation. Multiplying both sides of the continuity equation (Eq. 2.8) by  $(-v')$ , it yields,

$$0 = -v' \frac{\partial(ru')}{r \partial r} - v' \frac{\partial v'}{r \partial \lambda} - v' \frac{\partial w'}{\partial z} = -v' \frac{\partial u'}{\partial r} - v' \frac{\partial v'}{r \partial \lambda} - v' \frac{\partial w'}{\partial z} - \frac{u'v'}{r}. \quad (6.8)$$

Adding Eq. 6.6 and Eq. 6.8 together, and then, taking the azimuthal-mean, one can obtain the azimuthal-mean tangential wind tendency equation in the flux form,

$$\frac{\partial \bar{v}}{\partial t} = \overline{-u\eta} - \bar{w} \frac{\partial \bar{v}}{\partial z} - \frac{\partial(r^2 \overline{u'v'})}{r^2 \partial r} - \frac{\partial \overline{v'^2}}{\partial \lambda} - \frac{\partial \overline{w'v'}}{\partial z}. \quad (6.9)$$

From Eq. 6.7 (or Eq. 6.9), it is clear that the change in azimuthal-mean tangential wind can

be caused by both the axisymmetric processes ( $\overline{-u\eta} - \bar{w} \frac{\partial \bar{v}}{\partial z}$ ) and asymmetric processes

( $-\frac{\partial(r^2 \overline{u'v'})}{r^2 \partial r} - \frac{\partial \overline{v'^2}}{\partial \lambda} - \frac{\partial \overline{w'v'}}{\partial z}$ ). The axisymmetric process induced tangential wind tendency

is caused by the advection by the mean radial and vertical velocity. Recall that the mean

secondary circulation ( $\bar{u}$  and  $\bar{w}$ ) is not included in the theoretical derivation and analyses

of wave kinematic. Thus, the WRF simulations allow us to investigate the role of vortex

symmetric in response to asymmetric eddy forcing in vortex intensification. The

asymmetric process induced tangential wind tendency consists of three terms associated

with the radial eddy momentum flux divergence, vertical eddy momentum flux divergence,

and azimuthal eddy tangential wind variance divergence. Term  $-\frac{\partial \overline{v'^2}}{\partial \lambda}$  is considered as

small and often neglected in the budget analysis. Term  $-\partial(r^2 \overline{u'v'})/(r^2 \partial r)$  may be

decomposed into two terms  $-2\overline{u'v'}/r$  and  $-\partial \overline{u'v'}/\partial r$ . It is clear that the spin-up of a

vortex can result from either  $\overline{u'v'} < 0$  or decrease of  $\overline{u'v'}$  with  $r$ . The last term suggests

that the spin-up of a vortex can also be realized via the decrease of  $\overline{w'v'}$  with  $z$ . The

importance of these terms resulting from the asymmetric wave activities to vortex

intensification will be examined using the numerical data from the WRF simulations.

### 6.3 A Review of Wave-Mean-Flow Interaction in Barotropic Vortices

Using a 2D nondivergent barotropic model, MK97 first demonstrated that the eddy flux divergence associated with the radially propagating VRWs provides a mechanism to accelerate the vortex mean flow. In the 2D nondivergent barotropic framework, Eq. 6.7 reduces to,

$$\frac{\partial \bar{v}}{\partial t} = -\overline{u' \eta'}. \quad (6.10)$$

The change in the mean tangential wind over a time period  $\tau$ , then, can be written as,

$$\delta \bar{v} = \int_0^\tau \frac{\partial \bar{v}}{\partial t} dt = -\int_0^\tau \overline{u' \eta'} dt. \quad (6.11)$$

In order to clearly show the importance of vortex " $\beta$ " effect to the wave-mean-flow interaction, MK97 compared two experiments that are exactly the same except for the location where the initial asymmetry was placed. In the first experiment, the initial asymmetry was placed at a radius sufficiently far from the RMW (e.g., six, eight or nine times of the RMW) so that the radial gradient of vortex basic-state vorticity was negligible but the vortex shearing effect remained to be effective. The calculations showed that  $\delta \bar{v}$  induced by the eddy radial flux divergence exhibited a nearly symmetric reverse 'S' shape with the acceleration and deceleration of the mean flow on the up-shear side and down-shear side respectively, a pattern similar to the result in the rectilinear case of the zonal flow with a constant shear (Farrell 1987). Since the magnitude of the acceleration and deceleration is nearly identical, only redistribution of vortex mean flow but no net acceleration of the vortex was found.

In the second experiment, the center of initial asymmetry was placed right at the RMW where the radial gradient of the mean vorticity ( $\partial\bar{\eta}/\partial r$ ) is much larger than that in the first experiment. The results showed a significant outshift of the reverse ‘S’ shaped  $\delta\bar{v}$  (Fig. 6.1) in contrast to the symmetric reverse ‘S’ in the first experiment. In addition, the zero in  $\delta\bar{v}$  occurs at the very radius shown to be the stagnation radius of radially outward propagating VRW packets in both numerical simulation and WKB prediction. The maximum acceleration is larger than the deceleration and the maximum acceleration occurs outside the central radius of the initial asymmetry. MK97 pointed out that the role of vortex " $\beta$ " effect ( $\partial\bar{\eta}/\partial r$ ) here is to oppose the vortex shearing effect ( $r\partial\bar{\Omega}/\partial r$ ) in order to move both the stagnation radius and the wave-mean-flow interaction radius away from the center of the initial asymmetry. The net acceleration of the mean flow due to the vortex " $\beta$ " effect shown in Fig. 6.1 suggests that the sheared disturbances in the inner-core region of a vortex can intensify the vortex via wave-mean-flow interaction.

The asymmetric reverse ‘S’ shaped  $\delta\bar{v}$  with larger acceleration than deceleration via the wave-mean-flow interaction in the vortex-inner core region was also found in MM99’s 2D AB model and M00’s 3D AB model. These studies suggest that during the evolution of a vortex the energy of the asymmetries can be axisymmetrized into the mean flow inside the maximum of the eddy momentum fluxes. In this way, the VRW radial propagation induced by the vortex " $\beta$ " effect provides a mechanism to intensify a vortex.

Young and William (2005) investigated vortex intensification via wave-mean-flow interaction in barotropic vortices from the perspective of energy conversion. They found that the energy conversion between asymmetric disturbances and vortex mean flow depends on the horizontal tilting of the disturbances with respect to the mean flow. Their

basic finding may be schematically illustrated by Fig. 6.2, which conceptually shows two different types of tilting of an asymmetric disturbance with respect to the vortex mean flow on a horizontal plane. To make it simple, the azimuthal-mean tangential wind speed at the three radii (indicated by the thin curves with arrows) is assumed to be the same so that the radial gradient of mean angular velocity is negative everywhere in this vortex. In this simple setting, the sign of the energy conversion between asymmetric disturbances and vortex mean flow is solely determined by the radial eddy momentum flux  $-\overline{u'v'}$ . As illustrated by the figure, the sign of  $-\overline{u'v'}$  depends on the horizontal tilting of a perturbation with respect to the vortex mean flow. As illustrated in Fig. 6.2a, a cyclonic eddy can be divided by a line into two parts. On the southwest part of the eddy, the flow associated with the eddy has positive radial and tangential wind components ( $u' > 0, v' > 0$ ) because of the assumed constant mean tangential wind and zero mean radial flow in the barotropic setting. For the same reason, the eddy on the northeast part of the eddy possesses negative radial and tangential wind components with respect to the mean flow ( $u' < 0, v' < 0$ ). Thus, the net effect of this tilted eddy is to generate a positive radial eddy momentum flux ( $\overline{u'v'} > 0$ ). According to Eq. 6.9, this eddy may cause decrease of mean tangential wind via term  $-2\overline{u'v'}/r$ . In this case, the eddy may grow at the expense of the mean flow in this case. As shown in Fig. 6.2a, since the line that separates the eddy is tilted up against the increase of vortex angular velocity with the decrease of radius, the tilting of the eddy with respect to the vortex mean flow is named as the up-shear tilting. In the situation shown in Fig. 6.2b, the eddy is tilted in an opposite way to what is shown in Fig. 6.2a, and thus, it is named as the down-shear tilting. In this case, in contrast to the first case, on both sides of the line that separates the eddy, negative radial eddy momentum flux is generated

( $\overline{u'v'} < 0$ ). As a result, a down-shear tilted eddy will act to accelerate the vortex mean flow term  $-2\overline{u'v'}/r$  according to Eq. 6.9. Since the vortex is barotropic, what is shown in Fig. 6.2 applies to all levels of the vortex. Thus, depending on the orientation of eddy tilting, asymmetric disturbances can either accelerate the vortex mean flow or amplify by drawing energy from the mean flow.

However, there are several questions that remain to be addressed. First, the assumption that the background tangential wind in which an eddy is embedded is constant may only be valid for small eddies but is inappropriate for large eddies that can span a large range of radii. For varying mean tangential wind, the sign of  $u'v'$  will be much more complicated than what is depicted in Fig. 6.2. Second, even in the simplest setting of Fig. 6.2, it is unclear in what situation the divergence of radial eddy momentum flux ( $-\partial\overline{u'v'}/\partial r$ ) can accelerate the vortex mean flow. Third, in barotropic conditions, it is impossible to know how the vertical eddy flux divergence affects the acceleration or deceleration of mean tangential wind. Fourth, it is unclear to what extent the baroclinicity can change the horizontal tilting of eddies shown in Fig. 6.2, and if eddy vertical tilting resulting from VRW vertical propagation has significant impact on vortex intensification. Finally, the symmetric response to asymmetric eddy forcing needs to be further evaluated in baroclinic vortices. To investigate these issues, budget analyses of azimuthal-mean tangential wind have been carried out using the output from the WRF simulations performed in this study. The results of budget analyses and the impact of baroclinicity on wave-mean-flow interaction are discussed in the next section.

## 6.4 Wave-Mean-Flow Interaction in 3D Baroclinic Vortices

The WRF simulations discussed in this section are the same as those presented in Chapter 5. They are LB01, LB02, HB01, and HB02. The detailed numerical design has been described in section 5.3. Although both wn-1 and wn-2 asymmetries are investigated in this study, due to the ‘pseudomode’ generated in the wn-1 experiments, for the sake of clarity only results from the wn-2 experiments are here.

### 6.4.1 Wave Phase Tilting

The horizontal tilting of wn-2 vorticity in the quasi-barotropic and baroclinic regimes of a baroclinic vortex is first examined. Fig. 6.3 compares the positive Fourier coefficients of wn-2 asymmetric vorticity at  $z=0.5$  km as function of radius and azimuthal angle at 30 min, 4 h, and 8 h in experiment LB01 with those at  $z=5.0$  km in experiment LB02. The negative Fourier coefficients have been removed in the plots for clarity since they are merely the mirror of the positive Fourier coefficients. In this radius-azimuthal-angle coordinate, tilting of asymmetries is defined by the orientation of the phase line, a line that connects the maximum of Fourier coefficients of wave packets. Since the mean flow rotates cyclonically (from left to right in the x-axis), an upright phase line (i.e., parallel to y axis) indicates zero tilting of the asymmetries with respect to the radial gradient of mean angular velocity. If a phase line is tilted in such a way that the azimuth angle increases with the increase of radius, then, it indicates an up-shear tilting. Likewise, a down-shear tilting corresponds to a tilted phase line whose azimuth angle decreases with the increase of radius.

In the quasi-barotropic mean flow of LB01, the inner wave packets induced by the initial asymmetry show an up-shear tilting structure at the 30<sup>th</sup> min into the simulation (Fig. 6.3a). This is consistent with the conceptual model shown in Fig. 6.2 that growing eddies

should have an up-shear tilting structure. As the inner wave packets propagate radially outward, which is evident from the figures, the up-shear tilting of the waves gradually shifts to nearly upright. The horizontal structure of inner waves is apparently different from that of outer waves originated from the initially prescribed asymmetry. The outer wave packets are always down-shear tilted throughout the simulation, suggesting that the eddy energy of the outer waves are being symmetrized into the mean flow. Thus, through the radially outward propagating inner and outer VRW wave packets, the mean energy of the vortex is being redistributed. As we discussed earlier, without the vortex “ $\beta$ ” effect, such a redistribution of energy will not lead to vortex intensification. However, the vortex “ $\beta$ ” effect can cause the acceleration to be larger than deceleration depending on the strength of vortex “ $\beta$ ” effect and radial shearing effect. The distinct tilting structures of the inner and outer wave packets appear to be separated at the radius about 90km, which is the very stagnation radius of inner waves according to the theoretical analyses in Chapter 4 and WRF simulation verification in Chapter 5.

The wave horizontal tilting of in the baroclinic mean flow of LB02 (Figs. 6.3b, 6.3d, 6.3f) is fairly similar to that in the quasi-barotropic mean flow of LB01 except that the inner wave packets are always up-shear tilted, suggesting that inner waves keep growing during the simulation. This is probably caused by the enhanced vertical propagation of wave packets under strong baroclinicity.

The vertical phase tilting at the radius of  $r=60$  km in LB01 and LB02 is shown in Fig. 6.4. The reference radius of  $r=60$  km is chosen based on the consideration that waves inside the RMW can effectively propagate upward. In the early stage of the simulations, the wave packets in LB01 are nearly upright below 4 km. Above that, waves are down-

shear tilted. But wave packets are confined below 6 km because the asymmetry is initially placed at the surface where mean flow is quasi-barotropic. In LB02, since the initial asymmetry is placed at 5 km in the baroclinic regime, wave packets are seen at high levels up to 10 km. At the 30<sup>th</sup> min into the simulation, wave packets are down-shear tilted throughout the vertical column except for the low 2 km where wave packets are in-between upright and weakly up-shear tilted. At the 6<sup>th</sup> h into the simulation, wave packets are seen at the higher altitudes due to the vertical propagation of VRWs. All wave packets are shown to be down-shear tilted except for the low 1 km in LB02 where a weak up-shear tilting is seen. In all cases, it is shown that the down-shear tilting increases with the height. Thus, should  $-2\overline{u'v'}/r$  be the dominant term in the mean tangential wind budget, the symmetrization of eddy energy into the mean flow would be more efficient at higher altitudes due to vortex baroclinicity. This may be one of the major differences in wave-mean-flow interaction between barotropic and baroclinic vortices.

#### ***6.4.2 Tangential Wind Budget Analyses***

The wave-mean-flow interaction in the quasi-barotropic and baroclinic mean flow of 3D baroclinic vortices are further examined through analyzing the budget of the mean tangential wind tendency equation (Eq. 6.9). Fig. 6.5 compares radius-height structure of the net tendency of the mean tangential wind directly from the model output with the tendency components associated with the eddy flux divergence term and mean advection term at the 2<sup>nd</sup> and 4<sup>th</sup> h into the simulation in LB01. The tendency decomposition clearly shows that the eddy momentum flux divergence associated with wn-2 asymmetries dominates the tangential wind budget and the effect of mean advection is negligible. This

result is a little surprise considering that the symmetric response to asymmetric forcing is one of the key mechanisms for TC intensification according Nolan et al. (2007). The reason for this difference may be complex. Partially, it may be due to the continuous asymmetric forcing imposed in Nolan et al. (2007)'s simulation; whereas no external forcing is prescribed in our simulation. The insignificance of mean advection to tangential wind tendency may also be attributed to the quasi-barotropic mean flow in this experiment. I'll show shortly that asymmetries in the baroclinic mean flow can substantially enhance the vortex symmetric response to asymmetric forcing.

The vortex spin-up is mainly caused by the positive radial momentum flux (i.e.,  $-\overline{u'v'} > 0$ , solid lines in Fig. 6.5) ranging from  $r=30$  km to  $r=130$  km. Two peaks of positive  $-\overline{u'v'}$  can be observed at the 2<sup>nd</sup> h (Fig.6.5c). As discussed previously, this conversion of eddy energy to the mean flow should correspond to the shift of eddy orientation from the up-shear tilting to down-shear tilting due to the wave radial and vertical propagation. At the 6<sup>th</sup> h, the reduction of the inner positive  $-\overline{u'v'}$  indicates that the eddy kinetic energy has been symmetrized into the mean flow via the down-shear tilted wave packets. In addition to the vortex spin-up induced by  $-\overline{u'v'} > 0$ , part of the acceleration of the mean tangential wind should be attributed to the increase of  $-\overline{u'v'}$  with  $r$ , which is also evidenced in the figure. The deceleration of the mean flow around  $r=110$  km should be resulted from  $-\partial\overline{u'v'}/\partial r$ .

The budget analyses for LB02 and HB02 are shown in Fig. 6.6 and Fig. 6.7, respectively. This is to examine the vortex intensification via wave-mean-flow interaction in the baroclinic mean flow of vortices with weak and strong baroclinicity. Again, the tendency of mean tangential wind is dominated by the radial eddy momentum flux

divergence term. However, there are several distinct features worthy to be emphasized here. First, unlike the peaks of  $-\overline{u'v'}$  occurring at the surface during the entire simulation of LB01, both the inner and outer peaks of  $-\overline{u'v'}$  in LB02 and HB02 move upward with time due to the vertical propagation of wave packets supported by the baroclinicity. Second, the vertical structure of positive and negative tangential wind tendency in LB01 is nearly upright (Fig. 6.5). However, the positive and negative tangential wind tendencies in LB02 and HB02 show a significant inward tilting with height. This vertically tilted structure should be related to the vertical propagation of VRWs in the baroclinic mean flow of the vortex. As I showed previously, baroclinicity promotes vertical propagation of VRWs but suppresses wave radial propagation. Since baroclinicity increases with height for the constructed vortex used in this study, the increasingly suppressed wave radial propagation with height causes the inward tilting of tangential wind tendency in the radius-height plot. Third, the maximum of the positive  $-\overline{u'v'}$  is transported further upward in HB02 compared with that in LB02. This is due to the stronger baroclinicity prescribed in HB02. Finally, the contribution from the mean advection to tangential wind tendency increases substantially in HB02. This result suggests that baroclinicity not only can affect asymmetric wave activity but also has an important bearing on the vortex symmetric response to asymmetric forcing. The reason is that strong baroclinicity in HB02 induces a much stronger secondary circulation  $(\bar{u}, \bar{w})$  than that in LB01 and LB02.

### ***6.4.3 Vortex Mean Flow Change Induced by Asymmetry***

In order to examine the mean flow change induced by asymmetry via the wave-mean-flow interaction, two additional experiments are performed. These two experiments

are exactly the same as LB01, LB02, HB01, and HB02 but are performed without initial asymmetry. Thus, by examining the difference between the simulations with and without the prescribed asymmetry, the impact of asymmetry on vortex mean flow change can be quantified. Fig. 6.8 compares the radius-height structure of mean flow change induced by the initial asymmetries in experiments LB01, LB02, and HB02 at the 1<sup>st</sup> h and 12<sup>th</sup> h into the simulations, where color shades represent the mean vorticity change ( $\delta\bar{\zeta}$ ) and the solid/dashed lines represent the mean tangential wind change ( $\delta\bar{v}$ ). The maximum acceleration and the radius/height where it occurs are indicated in the legends. Despite the differences in basic-state of the vortex and initial asymmetry, the changes in  $\bar{\zeta}$  and  $\bar{v}$  share certain common features. In the early stage of the simulations (1<sup>st</sup> h), deceleration occurs on both sides of acceleration and the inner deceleration is larger than the acceleration, indicating that mean energy is being used to excite wave activity. The maximum increase of vorticity occurs at the radius where  $\delta\bar{v}$  is zero, and the vorticity depletion occurs on both sides of vorticity argument. The radius-height structure of  $\delta\bar{v}$  and  $\delta\bar{\zeta}$  and their relationship change substantially as time goes on. At the 12<sup>th</sup> h into the simulations, the change in  $\bar{v}$  in all cases exhibits the reverse “S” similar to that in MK97. The fact that the acceleration is larger than the deceleration suggests the eddy energy is transferred from the asymmetries to the mean flow. The changes in  $\bar{\zeta}$  and  $\bar{v}$  show an opposite pattern to that in the early simulation hours. The maximum vorticity depletion now corresponds well with zero in  $\delta\bar{v}$  and vorticity arguments occurring on both sides of vorticity depletion.

In addition to the common features shared by the different simulations, Fig. 6.8 also show several important differences between them. In LB01, at the 1<sup>st</sup> h into the simulation, a deceleration of the mean flow and the reduction of the mean absolute vorticity occur

around  $r=30$  km, which is due to the wave excitation around the maximum vortex " $\beta$ " effect. The maximum acceleration is shifted outward from 67km to 75km and is amplified from  $0.29 \text{ ms}^{-1}$  to  $1.0 \text{ ms}^{-1}$  from the 1<sup>st</sup> h to 12<sup>th</sup> h (Fig. 6a and 6b). The zero in  $\delta\bar{v}$  corresponds well with the stagnation radius 90km at the 12<sup>th</sup> h. The inner deceleration almost disappears at the 12<sup>th</sup> h, suggesting the up-shear tilted inner wave packets have been shifted to the down-shear tilting. The radial profiles of  $\delta\bar{v}$  at two pseudo heights (0.5 km and 5.0 km) at different times are shown in Fig. 6.9. The radial profiles of  $\delta\bar{v}$  at 0.5 km shares the same characteristics as that in MK97's, MM99's 2D model and MM00's 3D barotropic vortices. These include zero  $\delta\bar{v}$  occurring at the stagnation radius of radially propagating VRWs and the maximum acceleration located outside the center of initial asymmetry. The maximum acceleration at the higher level (5.0 km) occurs inside the center of initial asymmetry, which is approximately one order smaller in magnitude than the maximum acceleration at 0.5 km. This result suggests that the trapped VRWs (i.e., restricted wave vertical propagation) in the quasi-barotropic mean flow can barely induce the mean flow change at high altitudes.

LB02 and HB02 show a quite different story from LB01. At the 1<sup>st</sup> h, the vortex deceleration and vorticity reduction also occur around the radius of 30 km but is at the higher altitude near the height where initial asymmetry is placed (5.0 km). As the VRWs propagate both outward and upward, the maximum acceleration at the 12<sup>th</sup> h has migrated to 5.5 km, indicating the vertical propagation of VRW wave packets. In contrast to LB01 in which the maximum acceleration at the 12<sup>th</sup> h has moved to the radius (75 km) outside the center of initial asymmetry, the maximum acceleration in LB02 and HB02 only moves 71 km and 67 km respectively, the radius at and inside the center of initial asymmetry, reflecting the suppressed wave radial propagation caused by the baroclinicity. Both the

mean flow acceleration and the augment of the mean absolute vorticity are strengthened by the vortex baroclinicity. All above features suggest that the vortex baroclinicity has great impact on the wave-mean-flow interaction in the 3D baroclinic vortices.

The radial profiles of  $\delta\bar{v}$  at 2.5 km and 7.5 km for LB02 and HB02 are shown in Fig. 6.10 and Fig. 6.11. In contrast to LB01, the change in  $\bar{v}$  at the high altitude (7.5 km) in LB02 and HB02 is much larger than that at the low altitude (2.5 km). This is expected from the height of initial asymmetry (5.0 km) and the upward propagation of VRW packets. Moreover, the inner shift of zero  $\delta\bar{v}$  with height can be observed in both experiments. The maximum acceleration at the low level ( $z=2.5\text{km}$ ) is outside the center of the initial asymmetry similar to that in LB01. This is due to the fact that the vortex baroclinicity is weak at this altitude. However, the maximum mean acceleration at  $z=7.5$  km occurs inside the center of the initial asymmetry because of the suppression of wave radial propagation by vortex baroclinicity. This is an important difference of wave-mean-flow interaction between barotropic and baroclinic vortices. In barotropic conditions, the VRW radial propagation causes the vortex spin-up to occur outside the RMW where the initial asymmetry is prescribed, indicating that eyewall disturbances can lead to storm intensification and size expansion via wave-mean-flow interaction. In baroclinic conditions, wave-mean-flow interaction appears to result in stronger storm intensification than that in barotropic conditions. Most importantly, the upward propagation of VRWs tends to cause the contraction of the storm vortex during its intensification.

## 6.5 Summary

The impact of baroclinicity on wave-mean-flow interaction and vortex intensification in 3D baroclinic vortices are investigated using WRF simulations. Based on the budget equation of the mean tangential momentum, different contributions including the radial and vertical eddy momentum flux term ( $-\overline{u'v'}$  and  $-\overline{w'v'}$ ) and mean advection term to the change in azimuthal-mean tangential wind are examined using model outputs. The main results are summarized as follows.

In the quasi-barotropic regime of a baroclinic vortex, although the initial asymmetry induced wave packets are tilted up-shear with respect to the mean tangential wind in the early stage of the simulation (see illustration in Fig. 6.2b), the radial propagation of VRWs shifts the up-shear tilted wave phase to down-shear tilting (see illustration in Fig. 6.2a) consistent with what was found in barotropic vortices in previous studies. In the baroclinic regime of a baroclinic vortex, however, the radial propagation of VRWs is restricted and it is found that the highly confined radial propagation of VRW packets cannot shift the horizontal wave phase from up-shear tilting to down-shear tilting. The inner wave packets keep their horizontal up-shear tilting throughout the entire simulation period. In contrast, the enhanced VRW vertical propagation induces a down-shear tilting of the wave packets in the vertical and the tilting becomes more significantly as the upward VRW propagation strengthens.

The different wave phase tilting shows a significant impact on the wave-mean-flow interaction. In the quasi-barotropic regime, the net change in the mean tangential wind is dominated by the term associated with the eddy radial momentum flux divergence. The mean advection term is negligible. In the baroclinic regime, the tendencies induced by both

radial and vertical momentum flux divergence are important. Only in the strongest baroclinic case (i.e., experiment HB02), the tendency associated with the mean advection is non-negligible. Consistent with the previous studies, the maximum acceleration in quasi-barotropic regime occurs just outside the RMW. However, in the baroclinic regime the enhanced vertical propagation and suppressed radial propagation of VRWs cause the maximum acceleration of the mean flow to occur at the higher altitudes and inside the RMW. Thus, in addition to the intensification of a vortex, the wave-mean-flow interaction can also affect the size of a vortex. Asymmetries excited in the quasi-barotropic regime of a vortex tend to accelerate the mean flow at the larger radius to expand the size of storm; whereas asymmetries excited in the baroclinic regime of a vortex may cause the vortex to contract depending on the strength of basic-state baroclinicity and the location of the asymmetries. The implication is that the wave-mean-flow interaction associated with the asymmetries generated aloft by the diabatic heating in the inner eyewall and outer rainbands and the asymmetries generated in the boundary layer due to surface friction can have a different impact on TC evolution and intensification.

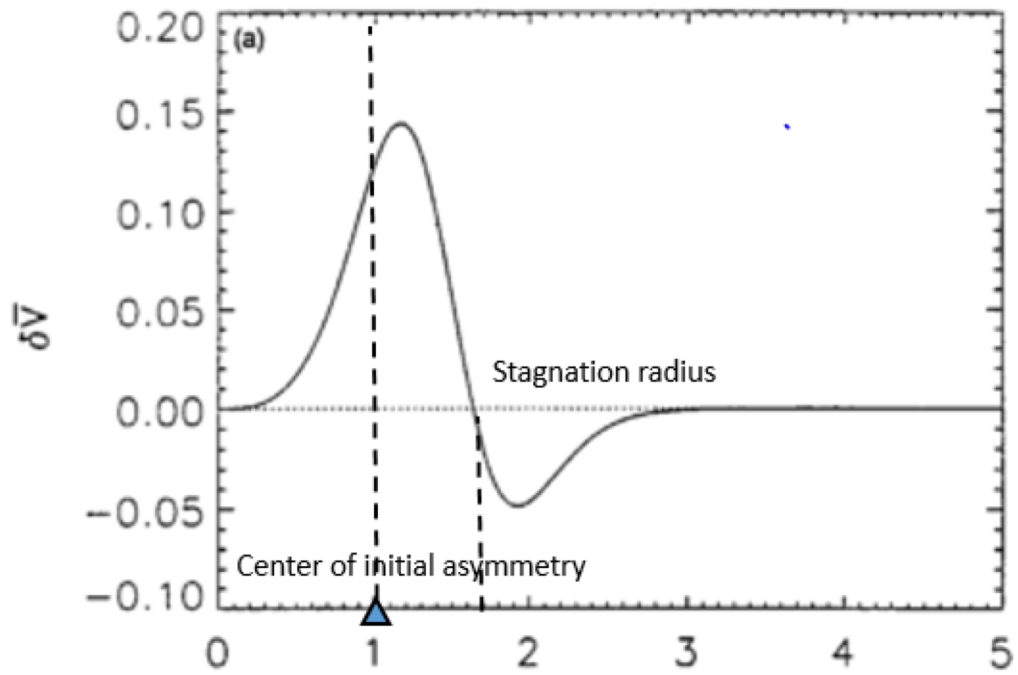


Fig. 6.1: Change in azimuthal-mean tangential wind induced by a wn-2 asymmetry in the simulation of a 2D non-divergent barotropic model. (After Montgomery and Kallenbach 1997)

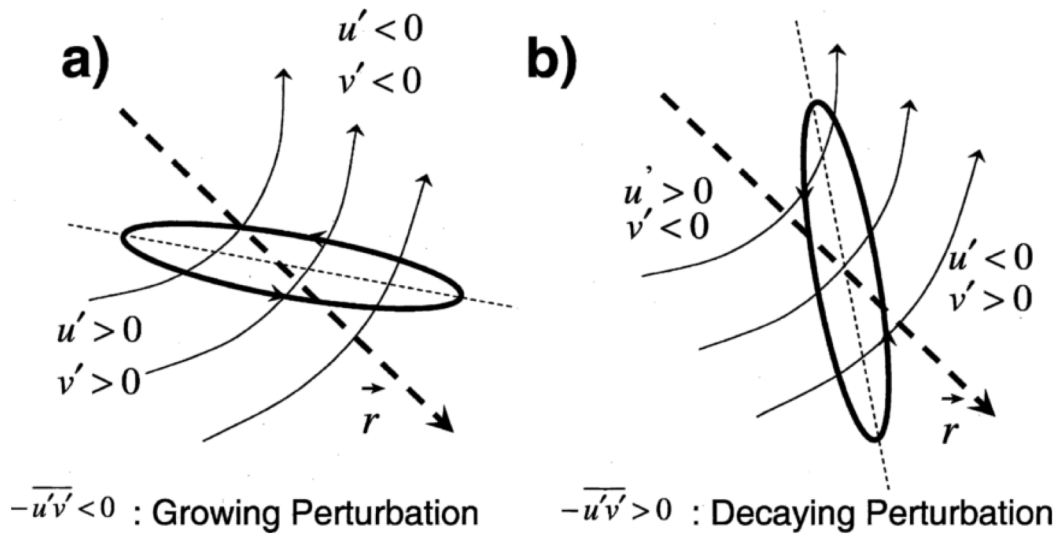


Fig. 6.2: Examples of the horizontal tilting of perturbations of (a) growing and (b) decaying cases in an idealized vortex in which the radial gradient of the mean angular velocity is set to a negative value such that the tangential wind speed is the same at all three radii indicated by the thin solid curves. Thick solid lines indicate a perturbation flow. Thin dashed lines separate regions of the perturbation that have opposite signs of tangential and radial wind direction. Thick dashed arrows represent the positive radial direction. (After Young and William 2005)

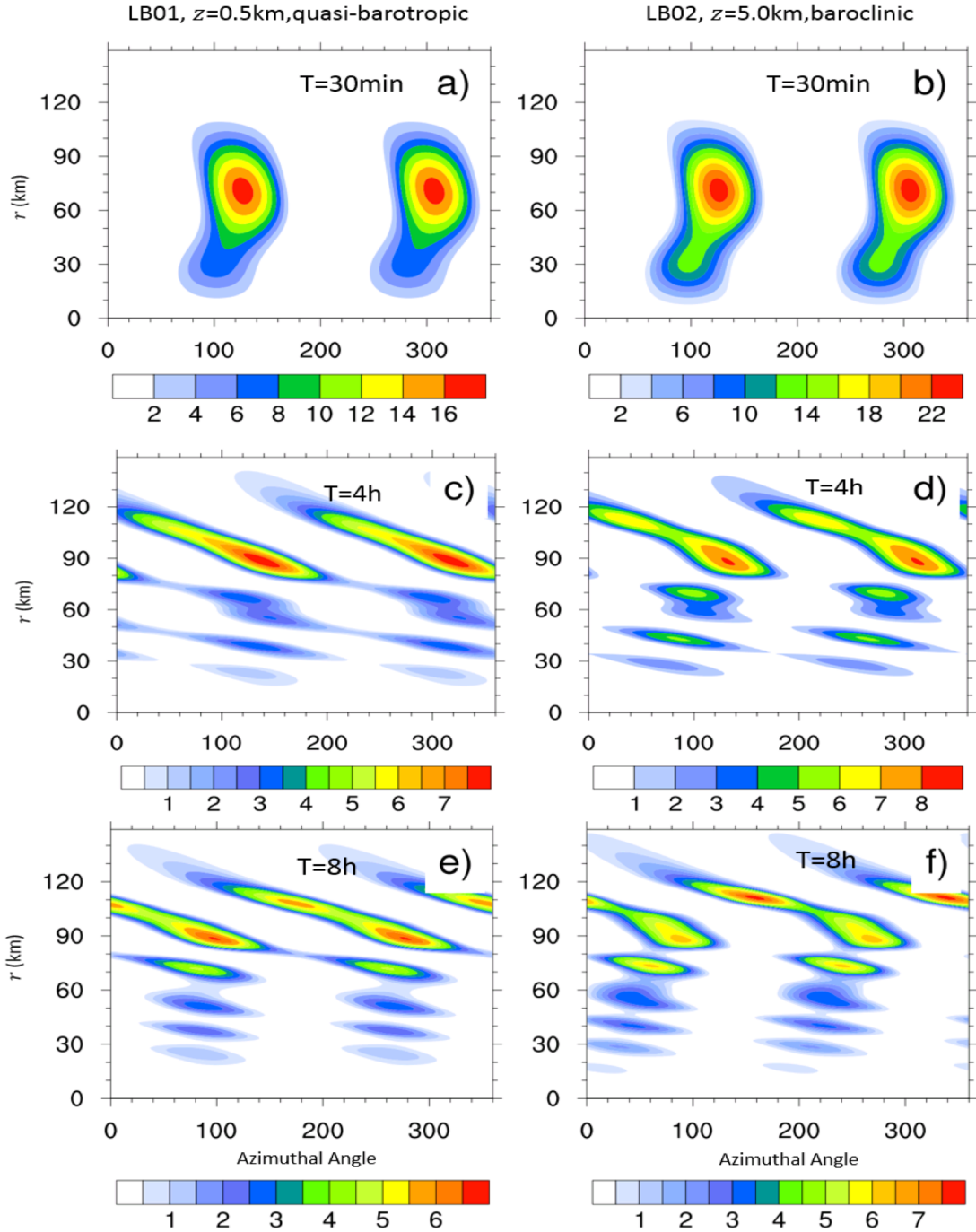


Fig. 6.3: (a), (c) and (e): Positive Fourier coefficients of  $w_{n=2}$  asymmetric vorticity at  $z=0.5\text{km}$  as function of azimuthal angle at 30 min, 4 h, and 8 h respectively in experiment LB01. (b), (d) and (f): The same as (a), (c), and (e) but for LB02 at  $z=5.0\text{km}$ . Vorticity ( $s^{-1}$ ) has been multiplied by a factor of  $10^5$ . The increase (decrease) of a phase line with azimuthal angle indicates an upshear (downshear) tilting.

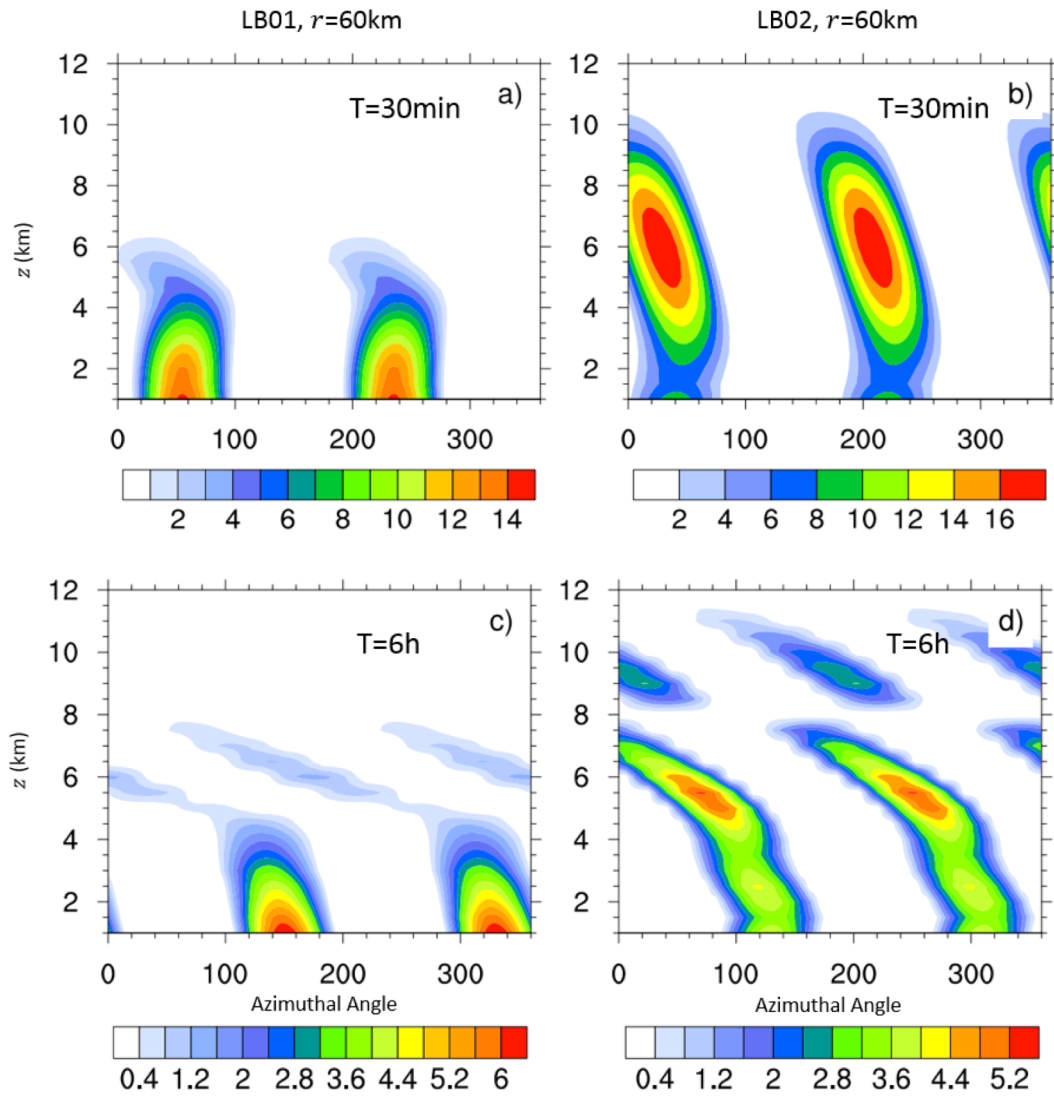


Fig. 6.4: The same as Fig 6.3 but for the wave phase tilting in the vertical at the radius of  $r=60\text{km}$ .

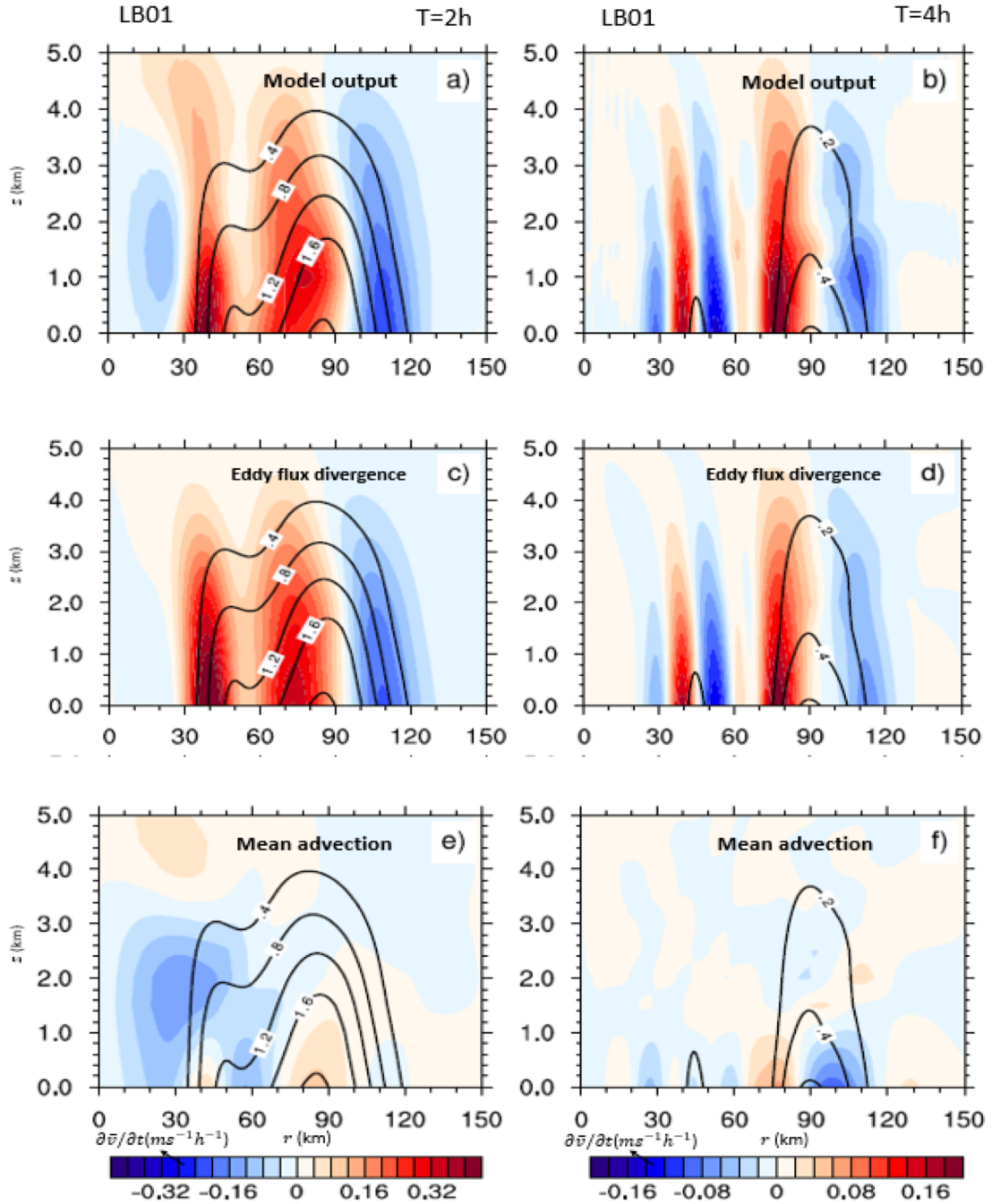


Fig. 6.5: (a) and (b): Radius-height plot of the simulated azimuthal-mean tangential wind tendency ( $ms^{-1}h^{-1}$ ) directly from the model output at 2 h and 4 h respectively in experiment LB01. (c) and (d): the diagnosed tendency ( $ms^{-1}h^{-1}$ ) associated with the eddy momentum divergence in the budget equation. (e) and (f): the diagnosed tendency ( $ms^{-1}h^{-1}$ ) associated with the mean advection in the budget equation. Solid contours in figures indicate the radial momentum flux ( $-\overline{u'v'}$ ,  $m^2s^{-2}$ ).

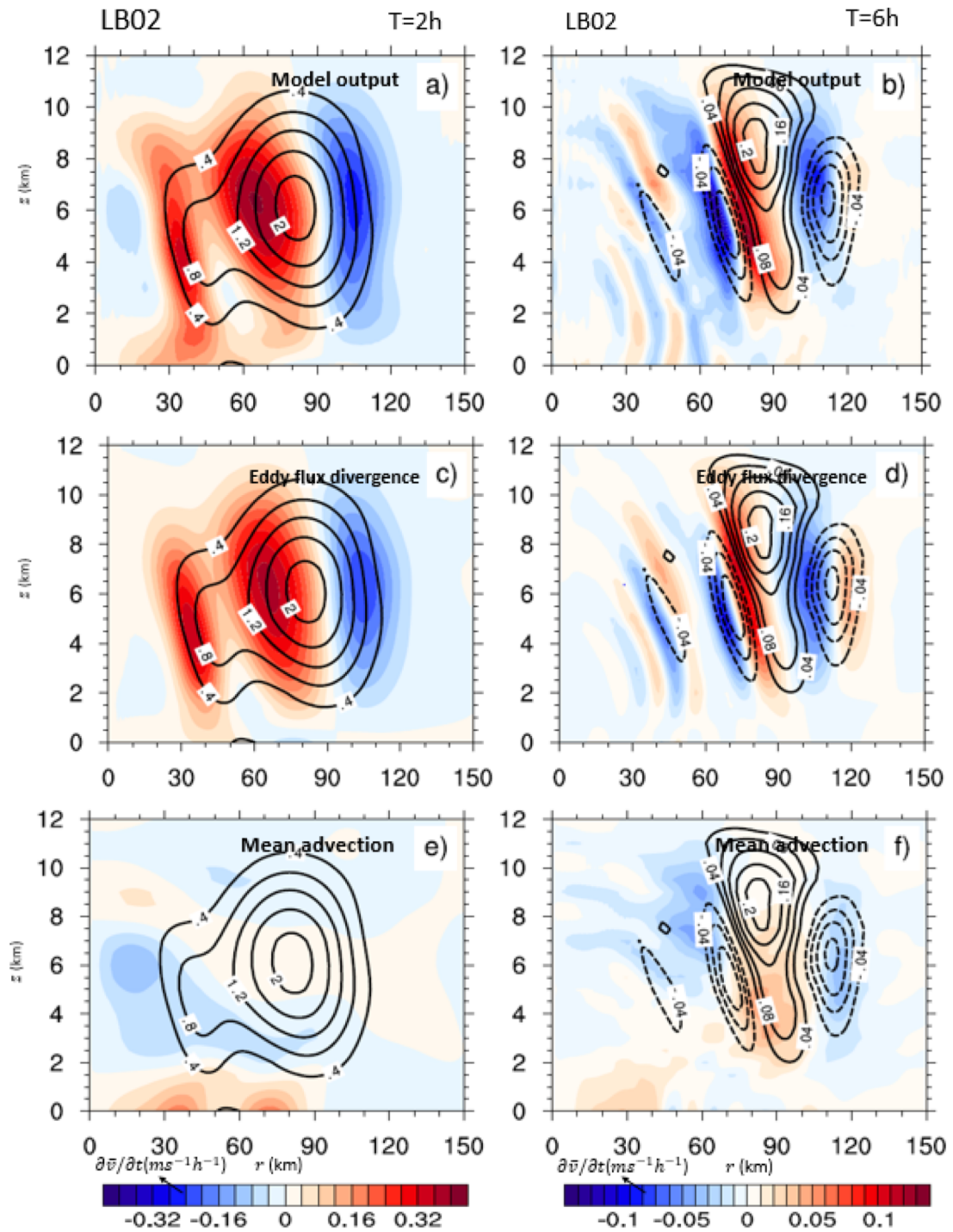


Fig. 6.6: The same as Fig. 6.5 but for LB02 at 2 h and 6 h.

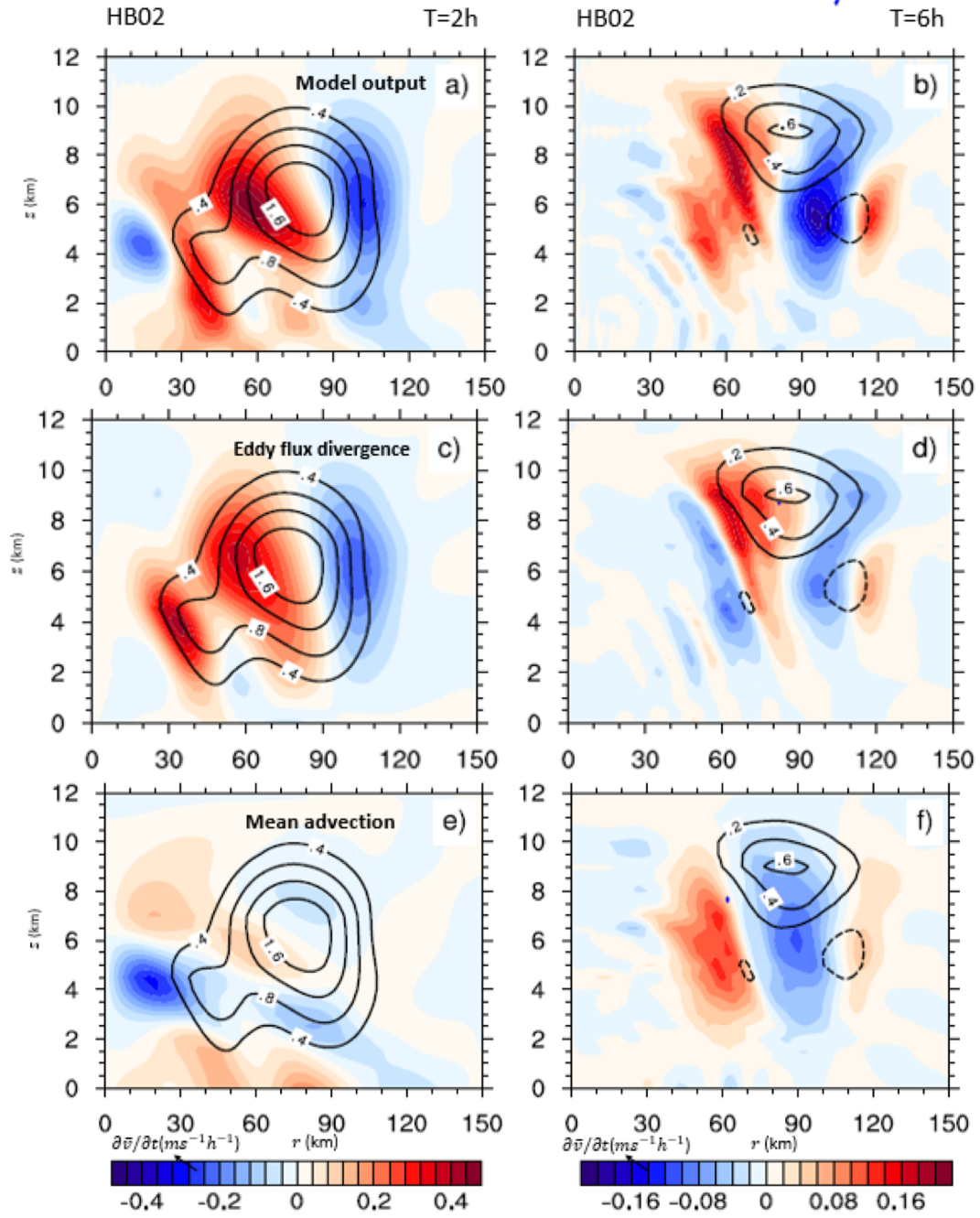


Fig. 6.7: The same as Fig. 6.6 but for HB02.

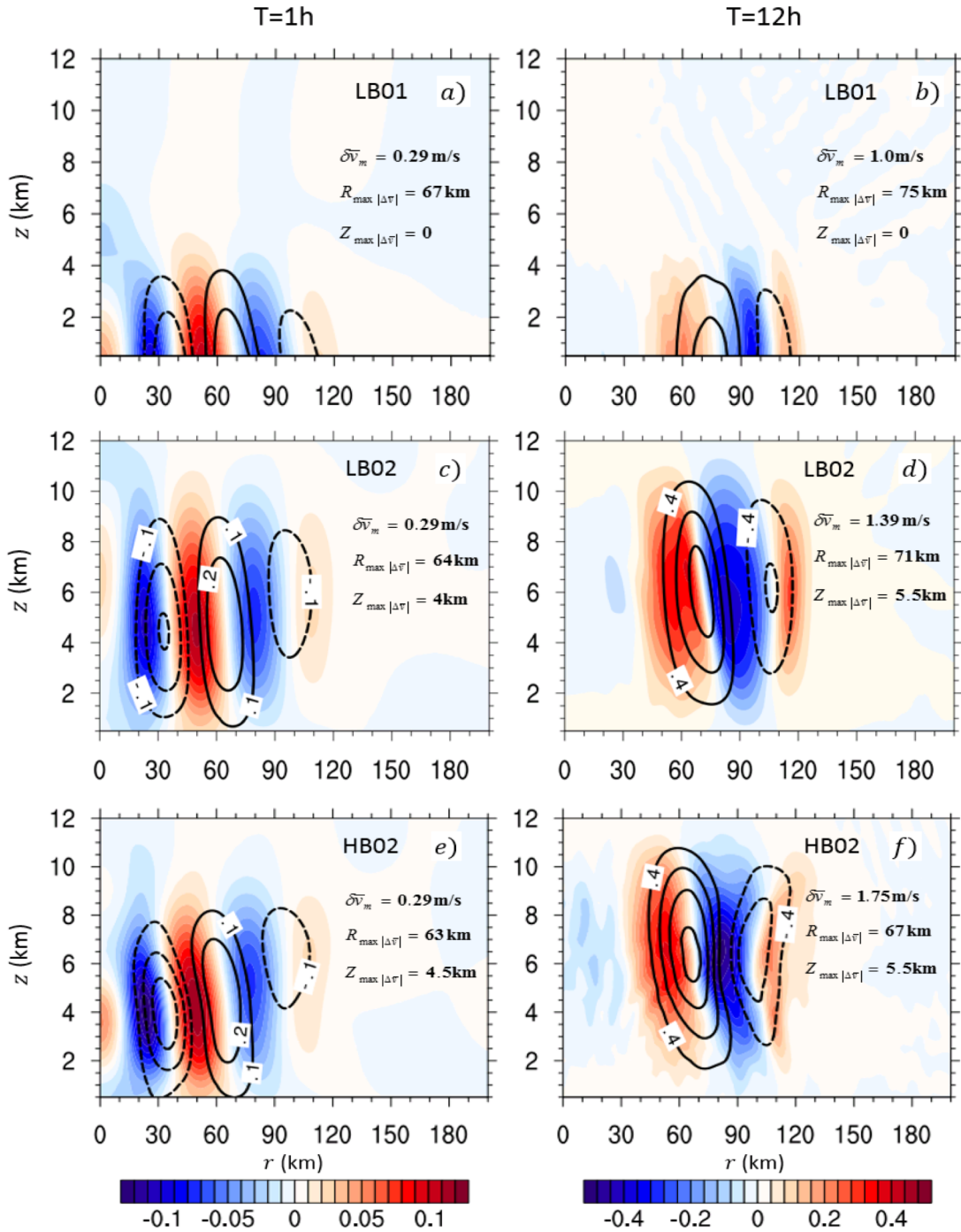


Fig. 6.8: (a), (c), and (e): Change in basic-state tangential wind  $\Delta\bar{v}$  (solid/dashed contours) and vorticity  $\Delta\bar{\zeta}$  (color shades) at 1 h for LB01, LB02, and HB02, respectively. (b), (d), and (f): The same as (a), (c), and (e) but for the fields at 12 h. The maximum acceleration (positive  $\delta\bar{v}$ ) and the position where it occurs are indicated by the legend in each figures.

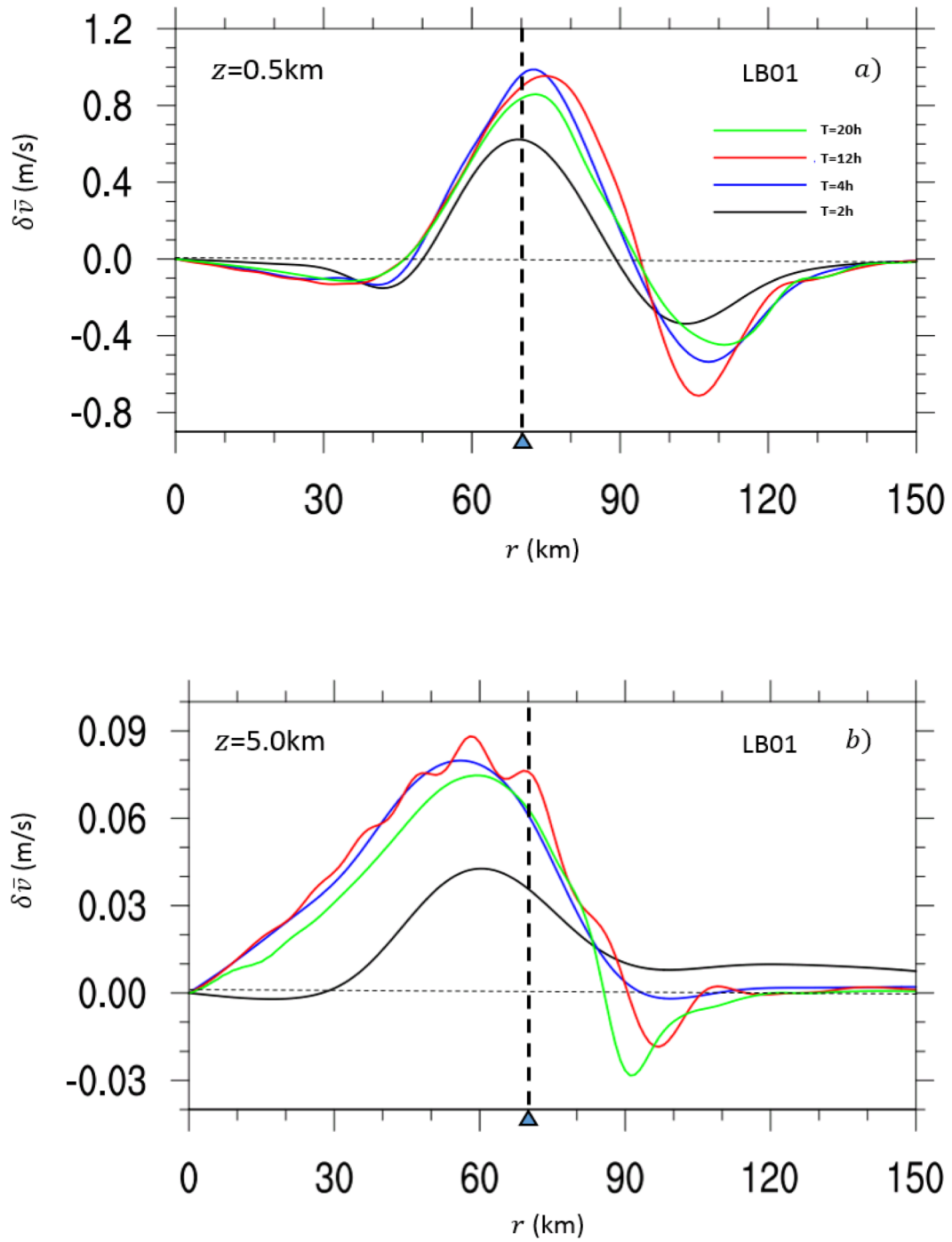


Fig. 6.9: (a) and (b): Evolution of the change in azimuthal-mean tangential wind at  $z=0.5\text{ km}$  and  $z=5.0\text{ km}$  in LB01, respectively. Thin dashed line indicates the zero line. Thick dashed line and triangle indicate the radius where the center of initial asymmetry is placed.

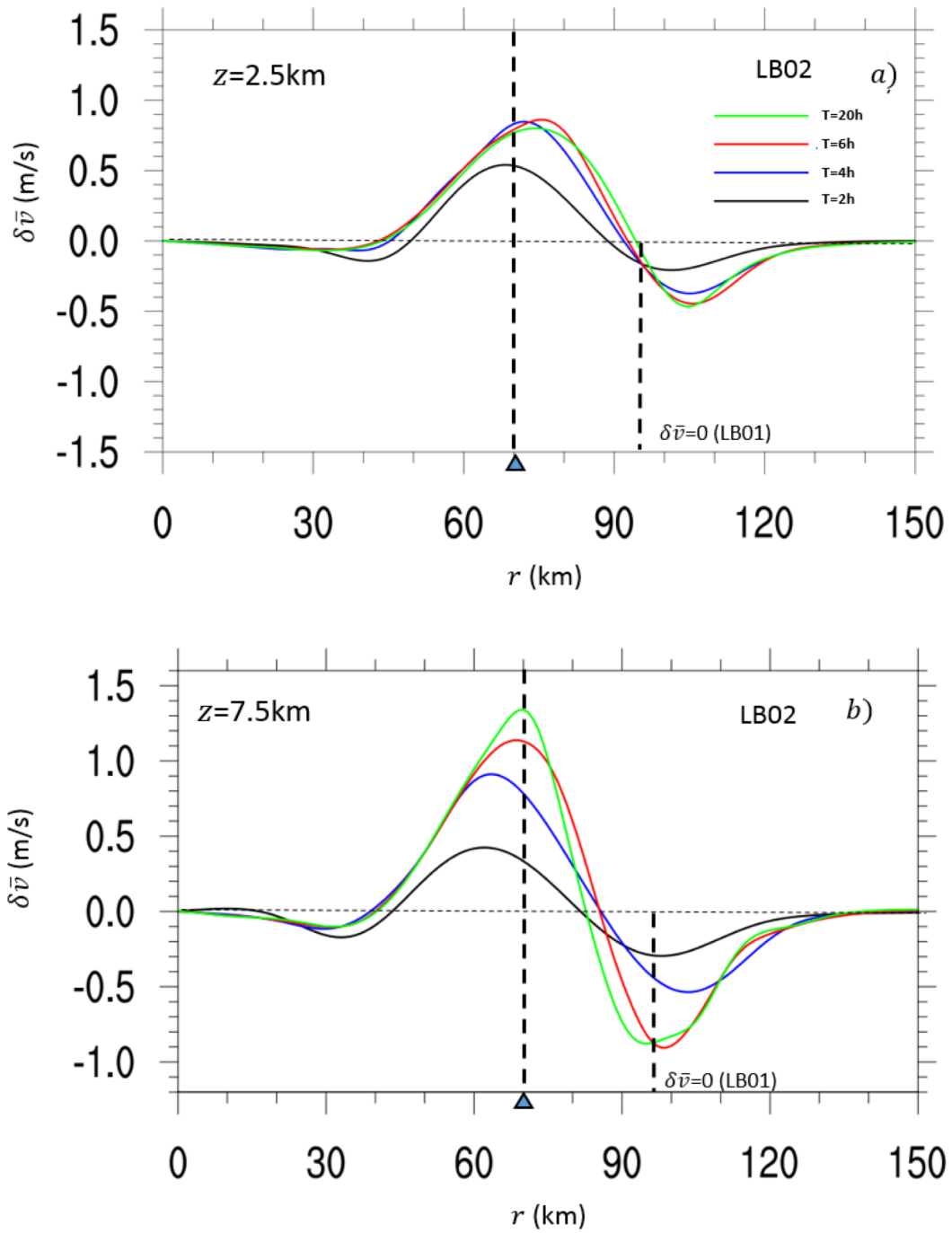


Fig. 6.10: The same as Fig 6.9 but for the change in azimuthal-mean tangential wind at  $z=2.5$  km and  $z=7.5$  km in LB02.

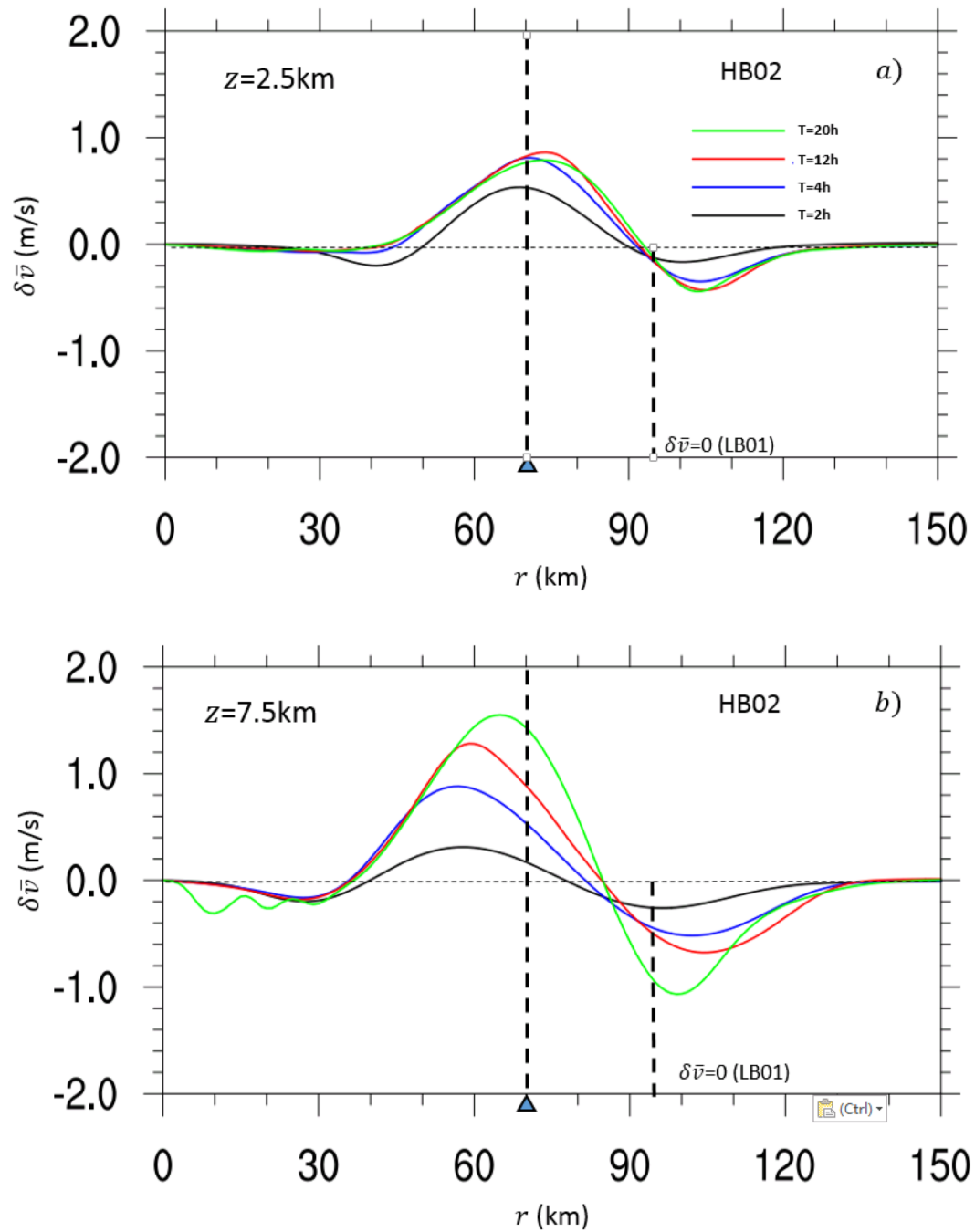


Fig. 6.11: The same as Fig 6.10 but for HB02 with strong vortex baroclinicity.

## Chapter 7: Summary and Conclusions

This dissertation study addresses key issues of TC internal dynamics from the perspective of VRWs. Previous studies on radial propagation of VRWs in barotropic vortices established a foundation for understanding the internal mechanisms of TC intensification via wave-mean-flow interaction. However, the VRW theory obtained based on the barotropic assumption cannot provide appropriate guidance for observational and numerical studies of TC intensification since the barotropic assumption oversimplifies the vertical structure of TCs. In this dissertation, the VRW kinematics, wave propagation features, and wave-mean-flow interactions in 3D baroclinic vortices are studied both theoretically and numerically. The first part of the dissertation presents a theoretical study of the wave kinematics and propagation using the WKB analysis within the AB approximation framework, and the second part validates the theoretical prediction of VRWs using non-hydrostatic WRF simulations and addresses issues regarding the wave-mean-flow interaction in baroclinic vortices. The main findings of this study are summarized as follows.

In Chapter 2, the generalized wave formulae in the pseudo-height coordinate that can describe VRW propagation in both barotropic and baroclinic conditions were derived. The results show that baroclinicity substantially complicates the VRW propagation due to both the vertical shearing effect that results in the increase of vertical wavenumber with time and the additional " $\beta$ " restoring mechanism that supports wave propagation.

In Chapter 3, the VRW kinematics is investigated in the isentropic coordinate. It is found that the wave dispersion relation and group velocities of VRW packets in baroclinic

vortices in the isentropic coordinate have the same mathematical format as those in barotropic vortices in the pseudo-height coordinate. To some extent, the wave propagation features on the isentropic surfaces may be analogues to that in barotropic vortices on the pseudo heights. This is not a surprise considering that adiabatic motions are virtually 2D when viewed in an isentropic coordinate. However, the increase of vertical wavenumber with time in baroclinic conditions largely complicates the wave propagation feature. It is shown that the maximum radial and vertical distance traveled by the VRW wave-packets in baroclinic conditions is constrained by the geometry of a ‘critical’ surface determined by the properties of initial wave-packets and basic-state vortices. Thus, an enhanced wave vertical propagation must be accompanied by suppression of wave radial propagation and vice versa.

In Chapter 4, the generalized wave formulae derived in this study are applied to baroclinic monopole vortices to investigate the impact of baroclinicity on the radial and vertical propagation of VRWs. The swirl profile and vertical extension used to construct baroclinic monopole vortices are the same as those described by MK97, MM00, and Nolan et al. (2007). The results confirmed the theoretical derivation that vortex baroclinicity tends to promote the vertical propagation of VRWs but suppresses wave radial propagation. It is also found that waves excited at the surface behave like those in barotropic vortices in that they are trapped in the low layer with substantial radial propagation, whereas waves excited in the low to mid troposphere in the inner-core region of a vortex can most effectively propagate upward but their radial propagation is largely suppressed. In contrast, perturbations excited outside the RMW cannot effectively propagate upward. The implication of this finding is that the wave-mean-flow interaction associated with the

asymmetries generated aloft by the diabatic heating of inner eyewall and outer rainbands and by surface friction may not simply follow what was depicted by the 2D nondivergent model and 3D barotropic model of MK97 and MM00.

The results of nonlinear and non-hydrostatic WRF simulations, which are designed to investigate the structure and evolution of asymmetries in 3D baroclinic vortices, are presented in Chapter 5. The wind and vorticity fields of the basic state vortices and asymmetries are initialized in the same way as that described in the Chapter 4. The thermodynamic fields that hold the vortices satisfy the hydrostatic and gradient wind balance and thermal wind relation. It is shown that the basic-state flow in a baroclinic vortex can be roughly classified into a quasi-barotropic regime near the surface and a baroclinic regime in the low- to mid-troposphere. VRW propagation shows substantially different characteristics in these two regimes. Comparison between vorticity and vertical velocity fields suggests that the wave packets in WRF simulations are indeed the VRWs. Quantitatively, the simulated radial and vertical group velocity is found to be consistent with the theoretical predictions presented in Chapter 4. Qualitatively, it is shown that the structure and evolution of asymmetries in the WRF simulations can well reproduce the main features of VRW obtained in our theoretical derivation.

For the cases in which the initial asymmetry is placed near the surface (experiments LB01 and HB01), the wave propagation features are similar to what was depicted in MK97's 2D and MM's 3D barotropic vortices. Wave packets, which increase their radial wavenumber with time, show substantial outward propagation. But wave vertical propagation is nearly negligible. In contrast, for the cases in which the initial asymmetry is placed in the middle troposphere (experiments LB02 and HB02), wave packets show

substantial vertical propagation with an apparent increase of vertical wavenumber with time. But the wave radial propagation is largely suppressed. The increase of vertical wave number, promotion of wave vertical propagation, and suppression of wave radial propagation became more substantial in the strong baroclinic vortex (HB02). In all cases, the wave packets excited in the inner-core region by the initial asymmetry and the outer wave packets originated from the initial asymmetry can reach the stagnation radii (heights) close to the theoretical predictions. In addition, the wn-1 asymmetry shows much stronger radial and vertical propagation than the wn-2 asymmetry.

Chapter 6 discusses how baroclinicity affects the wave-mean-flow interaction and its role in vortex intensification. The budget analyses of the mean tangential momentum were performed to investigate the role of various processes in vortex intensification. It is found that the negative radial momentum flux  $-\overline{u'v'}$  and its divergence are the main contributors to the vortex spinup. It is found that the wave phase tilting in the quasi-barotropic regime in the WRF simulation LB01 approximately follows what was depicted in the barotropic framework by the previous studies. However, the wave phase tilting in the baroclinic regime in experiments LB02 and HB01 shows different features. The promoted vertical propagation by baroclinicity causes a significant down-shear tilting of the wave packets in the vertical. The differences in wave phase tilting in the quasi-barotropic and baroclinic regimes are shown to have great impacts on the tendency of mean tangential wind. The positive tendency in experiment LB01 is well correlated to positive  $-\overline{u'v'}$  near the surface in the vicinity of RMW; whereas the mean tangential wind tendency in LB02 and HB02 induced by the positive  $-\overline{u'v'}$  is shifted to the high altitude caused by the vertical propagation of VRWs.

The wave phase tilting, radial/vertical eddy momentum flux and their divergence, as well as the vortex symmetric response to asymmetric forcing together lead to the distinct characteristics of wave-mean-flow interactions in 3D baroclinic vortices, which are substantially different from that in barotropic vortices. As a result, the change in mean tangential wind via wave-mean-flow interaction shows different characteristics in the experiments performed in this study. The maximum acceleration of mean tangential wind in LB01 occurs just outside the RMW similar to the result in 3D barotropic vortices. In LB02 and HB02, the wave excited in the inner-core region of the vortex can barely accelerate the mean flow at or outside the RMW. The enhanced wave upward propagation leads to a strong acceleration of the mean flow at the high altitudes.

The analyses show that wave-mean-flow interaction in LB02 and HB02 is substantially different from what was depicted by MK97 and MM00. In 2D nondivergent and 3D barotropic models, wave-mean-flow interaction tends to accelerate the mean flow at the larger radius to expand the size of the vortex. In baroclinic vortices, because of the restriction of wave radial propagation and promotion of vertical propagation, the wave-mean-flow interaction causes the acceleration of mean flow to occur inside of RMW, which would lead to the contraction of the vortex depending on the strength of basic-state baroclinicity and the altitudes where asymmetries are excited.

In this study, for the sake of simplicity, monopole vortices, which exclude the mechanism of barotropic instability, are used in our theoretical analyses and numerical simulations. However, a monopole vortex may only be found in the TC genesis stage. In reality, a typical TC vortex often consists of a well-defined vorticity annulus. How barotropic instability affects VRW radial/vertical propagation and vice versa is a question

yet to be addressed. Moreover, to what extent that the results from our theoretical analyses and numerical simulations can be extended to real TCs needs to be further explored. To investigate these issues will be the focus of my future research. Nonetheless, the theoretical derivation and numerical simulations performed in this dissertation study provide a good foundation and guidance for future study of the mechanisms governing the TC intensification.

## LIST OF THE REFERENCE:

- Black, P. G., and F. D. Marks, 1991: The structure of an eyewall meso-vortex in Hurricane Hugo (1989). Preprints, 19th Conf. on Hurricanes and Tropical Meteorology, Miami, FL, Amer. Meteor. Soc., 579–582.
- Black, R. A., and J. Hallett, 1986: Observations of the distribution of ice in hurricanes. *J. Atmos. Sci.*, 43, 802–822
- Bryan, G. H. and Rotunno, R., 2009a: The influence of near-surface, high- entropy air in hurricane eyes on maximum hurricane intensity, *J. Atmos. Sci.*, 66, 148–158.
- \_\_\_\_\_, 2009b: Evaluation of an analytical model for the maximum intensity of tropical cyclones, *J. Atmos. Sci.*, 66, 3042–3060.
- Carr III, L. E. and Williams, R. T., 1989: Barotropic vortex stability to perturbations from axisymmetry, *J. Atmos. Sci.*, 46, 3177–3191.
- Case, K. M., 1969: Stability of inviscid plane Couette flow. *Phys. Fluids*, 3, 143-148
- Charney, J. G. and Eliassen A., 1964: On the growth of the hurricane depression. *J. Atmos. Sci.*, 21, 68-75.
- Chen, Y., and Yau, M. K., 2001: Spiral bands in a simulated hurricane. Part I: Vortex Rossby wave verification, *J. Atmos. Sci.*, 58, 2128– 2145.
- Chen, Y., Brunet, G., and Yau, M. K., 2003: Spiral bands in a simulated hurricane. Part II: Wave activity diagnostics, *J. Atmos. Sci.*, 60, 1239–1256.
- Cotto, A., I. Gonzalez III, and H. E. Willoughby, 2015: Synthesis of vortex Rossby waves. Part I: Episodically forced waves in the inner waveguide. *J. Atmos. Sci.*, 72, 3940–3957, doi:10.1175/JAS-D-15-0004.1. Abstract
- Dunkerton, T. J., Montgomery, M. T., and Wang, Z., 2009: Tropical cyclogenesis in a tropical wave critical layer: easterly waves, *Atmos. Chem. Phys.*, 9, 5587–5646, doi:10.5194/acp-9-5587-2009.
- Eliassen, A., 1949: The quasi-static equations of motion with pressure as independent variable. *Geophys. Publ.*, 17, 1–44.

\_\_\_\_\_, 1951: Slow thermally or frictionally controlled meridional circulation in a circular vortex. *Astrophys. Norv.*, 5, 19–60.

Emanuel, K. A., 1986: An air-sea interaction theory for tropical cyclones. Part I: Steady state maintenance, *J. Atmos. Sci.*, 43, 585–604.

\_\_\_\_\_, 1989: The finite amplitude nature of tropical cyclogenesis, *J. Atmos. Sci.*, 46, 3431–3456.

\_\_\_\_\_, 1991: The theory of hurricanes. *Ann. Rev. Fluid Mech.*, 23, 179–196.

\_\_\_\_\_, 1995: Sensitivity of tropical cyclones to surface exchange coefficients and a revised steady-state model incorporating eye dynamics, *J. Atmos. Sci.*, 52, 3969–3976, 1995.

\_\_\_\_\_, 1997: Some aspects of hurricane inner-core dynamics and energetics, *J. Atmos. Sci.*, 54, 1014–1026.

\_\_\_\_\_, 2003: Tropical cyclone, *Annu. Rev. Earth Planet Sci.*, 31, 75–104, 2003.

Emanuel, K. A., Neelin, J. D., and Bretherton, C. S.: On large-scale circulations in convecting atmosphere, *Q. J. R. Meteorol. Soc.*, 120, 1111–1143, 1994.

Emanuel, K. A., DesAutels, C., Holloway, C., and Korty, R.: Environmental control of tropical cyclone intensity, *J. Atmos. Sci.*, 61, 843–858, 2004.

Farrell, B. F., 1982: The initial growth of disturbances in a baroclinic flow. *J. Atmos.*

Farrell, B. F., 1987: Developing disturbances in shear. *J. Atmos. Sci.*, 44, 2191–2199.

Fjortoft, R., 1962: On the integration of a system of geostrophically balanced prognostic equations. *Proc. Int. Symp. Numerical Weather Prediction, Tokyo, Japan, Meteorological Society of Japan*, 153–159

Gentry, R.C., T.T. Fujita and R.C. Sheets, 1970: Aircraft, spacecraft, satellite and radar observations of Hurricane Gladys, 1968. *J. Appl. Meteor.*, 9, 837–850.

Guinn, T.A., Schubert, W.H., 1993. Hurricane spiral bands. *J. Atmos. Sci.* 50, 3380–3403.

Holland, G. J., and G. S. Dietachmayer, 1993: On the interaction of tropical-cyclone-scale vortices. III: Continuous barotropic vortices. *Quart. J. Roy. Meteor. Soc.*, 119, 1381–1398.

Holton, J. R., 2004: An introduction to dynamic meteorology, Academic Press, London, 535 pp.

Hoskins, B. J., 1975: The geostrophic momentum approximation and the semi-geostrophic equations. *J. Atmos. Sci.*, 32, 233–242.

Kleinschmidt, E., Jr., 1951: Grundlagen einer Theorie des tropischen Zyklonen. *Archiv fur Meteorologie, Geophysik und Bioklimatologie, Serie A*, 4, 53-72.

Knaff, J. A., J. P. Kossin, and M. DeMaria, 2003: Annular hurricanes, *Weather Forecast*, 18, 204 – 223.

Kniewel, J. C., D. S. Nolan, and J. P. Kossin, 2004: An assessment of the balance in a mesoscale vortex within a midlatitude, continental mesoscale convective system. *J. Atmos. Sci.*, 61, 1827-1832.

Kossin, J. P., and M. D. Eastin, 2001: Two distinct regimes in the kinematic and thermodynamic structure of the hurricane eye and eyewall. *J. Atmos. Sci.*, 58, 1079-1090

Kossin, J. P., B. D. McNoldy, and W. H. Schubert, 2002: Vortical swirls in hurricane eye clouds. *Mon. Wea. Rev.*, 130, 3144-3149.

Kossin, J. P., and W. H. Schubert, 2004: Mesovortices in Hurricane Isabel (2003). *Bull. Amer. Meteor. Soc.*, 85, 151-153.

Kurihara, Y., 1976: On the development of spiral bands in a tropical cyclone. *J. Atmos. Sci.*, 33, 940–958.

Lewis, B. M., and H. F. Hawkins, 1982: Polygonal eye walls and rainbands in hurricanes. *Bull. Amer. Meteor. Soc.*, 63, 1294–1300.

MacDonald, N. J., 1968: The evidence for the existence of Rossbylike waves in the hurricane vortex. *Tellus*, 20, 138–150.

Marks, F.D., R.A. How, Jr. and J.F. Gamache, 1992: Dual-aircraft investigation of the inner core of Hurricane Norbert. Part I: Kinematic Structure. *J. Atmos. Sci.*, 49:919-942.

Marks, F. D. and Shay, L. K., 1998: Landfalling tropical cyclones: Forecast problems and associated research opportunities, *B. Am. Meteorol. Soc.*, 79, 867–876.

Malkus, J. S. and Riehl, H., 1960: On the dynamics and energy transformations in steady-state hurricanes. *Tellus*, 12, 1-20.

Mallen, K. J., M. T. Montgomery, and B. Wang, 2005: Reexamining the near-core radial structure of the tropical cyclone circulation: Implications for vortex resiliency. *J. Atmos. Sci.*, 62, 408–425.

\_\_\_\_\_, 2010: On the dynamics and energy transformations in steady-state hurricanes, *Tellus*, 12, 1–20, 1960. Martinez, Y. H.: Diagnostic study of hurricane asymmetries using empirical normal modes, Ph. D. thesis, McGill University, 188 pp., 2008. Martinez, Y., Brunet, G., and Yau, M. K.: On the dynamics of two-dimensional hurricane-like vortex symmetrization, *J. Atmos. Sci.*, 67, 3559–3580.

McCalpin, J.D., 1987: “On the adjustment of azimuthally perturbed vortices”, *J. Geophys. Res.* 92, 8213–8225.

McWilliams, J. C., 1985: A uniformly valid model spanning the regimes of geostrophic and isotropic, stratified turbulence: Balanced turbulence. *J. Atmos. Sci.*, 42, 1773–1774.

McWilliams, J. C., Graves, L. P., and Montgomery, M. T., 2003: A formal theory for vortex Rossby waves and vortex evolution, *Geophys. Astrophys. Fluid Dyn.*, 97, 275–309.

Melander, M.V., McWilliams, J.C., Zabusky, N.J., 1987. Axisymmetrization and vorticity-gradient intensification of an isolated two-dimensional vortex through filamentation. *J. Fluid Mech.* 178, 137–159.

Molinari, J., P. Moore, and V. Idone, 1999: Convective structure of hurricanes as revealed by lightning locations. *Mon. Wea. Rev.*, 127, 520–534.

Moller, J. D., and M. T. Montgomery, 1999: Vortex Rossby waves and hurricane intensification in a barotropic model. *J. Atmos. Sci.*, 56, 1674–1687.

Möller, J. D. and Montgomery, M. T., 2000: Tropical cyclone evolution via potential vorticity anomalies in a three-dimensional balance model, *J. Atmos. Sci.*, 57, 3366–3387.

Montgomery, M. T. and Enagonio, J. 1998: Tropical cyclogenesis via convectively forced vortex Rossby waves in a three-dimensional quasigeostrophic model, *J. Atmos. Sci.*, 55, 3176–3207.

Montgomery, M. T. and L. J. Shapiro, 1995: Generalized Charney-Stern and Fjortoft theorems for rapidly rotating vortices. *J. Atmos. Sci.*, 52, 1829-1833.

\_\_\_\_\_, 1997: A theory for vortex Rossby waves and its application to spiral bands and intensity changes in hurricanes. *Quart. J. Roy. Meteor. Soc.*, 123, 435–465.

Montgomery, M. T. and Enagonio, J., 1998: Tropical cyclogenesis via convectively forced vortex Rossby waves in a three-dimensional quasigeostrophic model, *J. Atmos. Sci.*, 55, 3176–3207.

Montgomery M. T. and R. K. Smith, 2013: Paradigms for tropical-cyclone intensification, *Aust. Meteor. Ocean. J.*

Montgomery, M. T., Nguyen, S. V., Persing, J., and Smith, R. K., 2009: Do tropical cyclones intensify by WISHE?, *Q. J. R. Meteorol. Soc.*, 135, 1697–1714.

Muramatsu, T., 1986: Trochoidal motion of the eye of Typhoon 8019. *J. Meteor. Soc. Japan*, 64, 259–272.

Nguyen, V. S., Smith, R. K., and Montgomery, M. T., 2008: Tropical-cyclone intensification and predictability in three dimensions, *Q. J. R. Meteorol. Soc.*, 134, 563–582.

Nolan, D. S. and M. T. Montgomery, 2002: Nonhydrostatic, three-dimensional perturbations to balanced, hurricane-like vortices. Part I: Linearized formulation, stability, and evolution. *J. Atmos. Sci.*, 59, 2989–3020.

Nolan, D. S. and Grasso, L. D., 2003: Nonhydrostatic, three-dimensional perturbations to balanced, hurricane-like vortices. Part II: Symmetric response and nonlinear simulations, *J. Atmos. Sci.*, 60, 2717–2745.

Nolan, D. S., Yumin, M., and Stern, D. P., 2007: Tropical cyclone intensification from asymmetric convection: Energetics and efficiency, *J. Atmos. Sci.*, 64, 3377–3405.

Ooyama KV., 1964: A dynamical model for the study of tropical cyclone development. *Geophys. Int.*, 4, 187-198.

\_\_\_\_\_, 1969: Numerical simulation of the life cycle of tropical cyclones. *J. Atmos. Sci.*, 26, 3-40.

\_\_\_\_\_, 1982: Conceptual evolution of the theory and modeling of the tropical cyclone. *J. Meteor. Soc. Japan*, 60, 369-380.

\_\_\_\_\_, 1997: Footnotes to “Conceptual evolution.” Preprints, 22d Conf. on Hurricanes and Tropical Meteorology, Fort Collins, CO, Amer. Meteor. Soc., 13–18.

Peng, J., M. S. Peng, and T. Li, 2008: Dependence of vortex axisymmetrization on the characteristics of the asymmetry. *Quart. J. Roy. Meteor. Soc.*, 134, 1253–1268

Peng, M. S., J. Peng, T. Li, and E. Hendricks, 2014a: Effect of baroclinicity on vortex axisymmetrization. Part I: Barotropic basic vortex. *Adv. Atmos. Sci.*, 31(6), doi: 10.1007/s00376-014-3237-x.

\_\_\_\_\_, 2014b: Effect of baroclinicity on vortex axisymmetrization. Part II: Baroclinic basic vortex. *Adv. Atmos. Sci.*, 31(6), doi: 10.1007/s00376-014-3238-9.

Rappaport, E. N., and Coauthors, 2009: Advances and challenges at the National Hurricane Center. *Wea. Forecasting*, 24, 395–419.

Raymond, D. J., and Emanuel, K., 1993, The Kuo cumulus parameterization: The representation of cumulus convection in numerical models,

*Meteorol. Monogr.*, 46, 145–150, Amer. Meteorol. Soc., Boston, USA.

Riehl, H., 1954: *Tropical Meteorology*. McGraw-Hill, New York, 392 pp.

Ritchie, E.A., Holland, G.J., 1993: On the interaction of tropical-cyclone scale vortices. II. Discrete vortex patches. *Q. J. R. Meteorol. Soc.* 119, 1363–1379.

Rotunno, R. and Emanuel, K. A., 1987: An air-sea interaction theory for tropical cyclones. Part II: Evolutionary study using a nonhydrostatic axisymmetric numerical model, *J. Atmos. Sci.*, 44, 542–561.

Rozoff, C. M., Schubert, W. H., McNoldy, B., and Kossin, J. P., 2006: Rapid filamentation zones in intense tropical cyclones, *J. Atmos. Sci.*, 63, 325–340.

Schubert, W. H., Montgomery, M. T., Taft, R. K., Guinn, T. A., Fulton, S. R., Kossin, J. P., and Edwards, J. P., 1999: Polygonal eyewalls, asymmetric eye contraction, and potential vorticity mixing in hurricanes, *J. Atmos. Sci.*, 56, 1197–1223.

Shapiro, L. J. and Montgomery, M. T., 1993: A three-dimensional balance theory for rapidly rotating vortices, *J. Atmos. Sci.*, 50, 3322–3335.

Shapiro, L. J., and Willoughby, H. E., 1982: The response of balanced hurricanes to local sources of heat and momentum. *J. Atmos. Sci.*, 39, 378–394.

Lloyd J. Shapiro, 2000: Potential Vorticity Asymmetries and Tropical Cyclone Evolution in a Moist Three-Layer Model. *J. Atmos. Sci.*, 57, 3645–3662. doi: [http://dx.doi.org/10.1175/1520-0469\(2000\)057<3645:PVAATC>2.0.CO;2](http://dx.doi.org/10.1175/1520-0469(2000)057<3645:PVAATC>2.0.CO;2)

Smith II, G. B. and Montgomery, M. T., 1995: Vortex axisymmetrization: Dependence on aximuthal wave-number or asymmetric radial structure changes, *Q. J. R. Meteorol. Soc.*, 121, 1615–1650.

Smith, R. K., Montgomery, M. T., and Nguyen, S. V., 2008: Axisymmetric dynamics of tropical cyclone intensification in a three-dimensional model, *Q. J. R. Meteorol. Soc.*, 134, 337–351.

\_\_\_\_\_, 2009: Tropical cyclone spin-up revisited, *Q. J. R. Meteorol. Soc.*, 135, 1321–1335.

Sutyryn, G.G., 1989: “Azimuthal waves and symmetrization of an intense vortex”, *Sov. Phys. Dokl.* 34, 104–106.

Terwey, W. D., and Montgomery, M. T., 2008: Secondary eyewall formation in two idealized, full-physics modeled hurricanes. *J. Geophys. Res.*, 113, D12112, doi:10.1029/2007JD008897.

Wang, Y., 2002a: Vortex Rossby waves in a numerically simulated tropical cyclone. Part I: Overall structure, potential vorticity, and kinetic energy budgets, *J. Atmos. Sci.*, 59, 1213–1238.

\_\_\_\_\_, 2002b: Vortex Rossby waves in a numerically simulated tropical cyclone. Part II: The role in tropical cyclone structure and intensity changes, *J. Atmos. Sci.*, 59, 1239–1262.

Willoughby, H. E., 1978: A possible mechanism for the formation of hurricane rainbands. *J. Atmos. Sci.*, 35, 838–848.

\_\_\_\_\_, 1990: Gradient balance in tropical cyclones, *J. Atmos. Sci.*, 47, 265–274.

\_\_\_\_\_, 1990: Temporal changes of the primary circulation in tropical cyclones. *J. Atmos. Sci.*, 47, 242–264.

\_\_\_\_\_, 1995: Mature structure and evolution. In *Global Perspectives on Tropical Cyclones*. pp21-62. WMO/TD-No 693 (Ed. R. L. Elsberry), World Meteorological Organization, Geneva, 289pp.

Wu, L. and Braun, S. A, 2004: Effects of environmentally induced asymmetries on hurricane intensity: a numerical study, *J. Atmos. Sci.*, 61, 3065–3081, 2004.

VITA

CEN GAO

2005-2009                    B.S. Atmospheric Science  
                                  Nanjing University  
                                  Nanjing, China PR

2010-2016                    Research Assistant  
                                  Florida International University  
                                  Miami, Florida

PUBLICATION AND PROFESSIONAL PRESENTATION

Gao, C., and P. Zhu, 2015: Vortex Rossby wave propagation in baroclinic TC-like vortices, *Geophys. Res. Lett.* in revision.

Zhu, P., Z-D. Zhu, S. Gopalakrishnan, R. Black, F. D. Marks, V. Tallapragada, J. Zhang, X. Zhang, C. Gao, 2015: Impact of sub-grid scale processes on eyewall replacement cycle of tropical cyclones in HWRF system, *Geophys. Res. Lett.* 42, doi:10.1002/2015GL066436

Zhu, P., Y. Wang, S. S. Chen, M. Curcic, C. Gao, 2015: Impact of storm-induced cooling of sea surface temperature on large turbulent eddies and vertical turbulent transport in the atmospheric boundary layer of Hurricane Isaac. *J. Geophys. Res. - Ocean.* 121, doi:10.1002/2015JC011320.

Gao, C.: Sensitivity of eyewall structure and intensification of tropical cyclones to the boundary layer turbulent mixing, 30<sup>st</sup> AMS hurricane conference, Apr. 15<sup>st</sup> -20<sup>th</sup>, 2012, Ponte Vedra Beach, FL.

Gao, C.: Inner-core asymmetric dynamics of tropical cyclones in 3D nonlinear simulations, 31<sup>st</sup> AMS hurricane conference, March 31 – April 4, 2014, San Diego, California.

Gao, C.: Vortex Rossby wave propagation and wave-mean-flow interaction in 3D baroclinic TC-like vortices, 32<sup>nd</sup> AMS hurricane conference, Apr. 17<sup>th</sup>-22<sup>nd</sup>, 2016, San Juan, PR.